Cell

Resource

Metformin decelerates aging clock in male monkeys

Graphical abstract

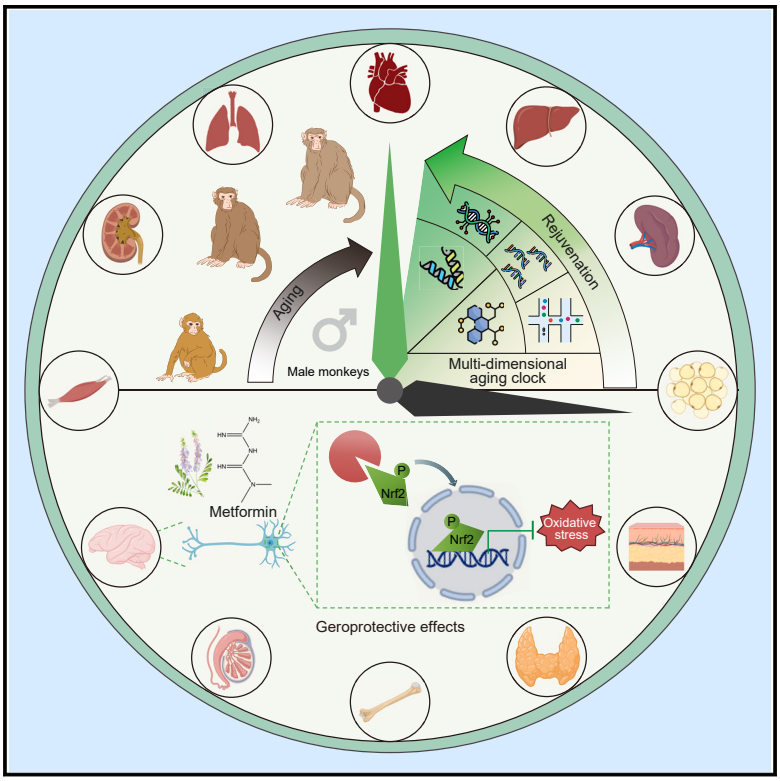

Highlights

- Metformin prevents brain atrophy, elevating cognitive function in aged male primates
- Metformin slows the pace of aging across diverse male primate tissues
- Metformin counterparts neuronal aging, delivering geroprotection via Nrf2 in male primates

Authors

Yuanhan Yang, Xiaoyong Lu, Ning Liu, ..., Jing Qu, Weiqi Zhang, Guang-Hui Liu

Correspondence

qujing@ioz.ac.cn (J.Q.),
zhangwq@big.ac.cn (W.Z.),
ghliu@ioz.ac.cn (G.-H.L.)

In brief

Prolonged metformin treatment diminishes the multidimensional biological age and alleviates neuronal aging through the Nrf2 pathway in male primates.

Yang et al., 2024, Cell *187*, 1–21
October 31, 2024
https://doi.org/10.1016/j.cell.2024.08.021

CellPress

Please cite this article in press as: Yang et al., Metformin decelerates aging clock in male monkeys, Cell (2024), https://doi.org/10.1016/j.cell.2024.08.021

Cell

CellPress

Resource

Metformin decelerates aging clock in male monkeys

Yuanhan Yang,[1,10,23] Xiaoyong Lu,[2,3,10,23] Ning Liu,[7,8,23] Shuai Ma,[1,4,5,10,23] Hui Zhang,[1,10,13,23] Zhiyi Zhang,[7,23] Kuan Yang,[2,3,10] Mengmeng Jiang,[1,4,5] Zikai Zheng,[2,3,10] Yicheng Qiao,[7,8] Qinchao Hu,[1,11] Ying Huang,[12] Yiyuan Zhang,[1,4,5] Muzhao Xiong,[2,3,10] Lixiao Liu,[2,3,10] Xiaoyu Jiang,[1,10] Pradeep Reddy,[15] Xueda Dong,[7,9] Fanshu Xu,[7,8] Qiaoran Wang,[2,3,10] Qian Zhao,[6] Jinghui Lei,[6] Shuhui Sun,[13] Ying Jing,[6] Jingyi Li,[1,4,5,22] Yusheng Cai,[1,4,5] Yanling Fan,[2,3] Kaowen Yan,[1,4,5] Yaobin Jing,[1,4,5,14] Amin Haghani,[15] Mengen Xing,[19] Xuan Zhang,[20,24] Guodong Zhu,[21,24] Weihong Song,[19,24] Steve Horvath,[15,24] Concepcion Rodriguez Esteban,[15,24] Moshi Song,[1,5,10,24] Si Wang,[6,22,24] Guoguang Zhao,[16,17,18,24] Wei Li,[1,4,5,10,24] Juan Carlos Izpisua Belmonte,[15,24] Jing Qu,[1,4,5,10,13,22,*] Weiqi Zhang,[2,3,4,5,10,22,*] and Guang-Hui Liu[1,4,5,6,10,22,25,*]

[1]Key Laboratory of Organ Regeneration and Reconstruction, State Key Laboratory of Membrane Biology, State Key Laboratory of Stem Cell and Reproductive Biology, Institute of Zoology, Chinese Academy of Sciences, Beijing 100101, China
[2]China National Center for Bioinformation, Beijing, China
[3]Beijing Institute of Genomics, Chinese Academy of Sciences, Beijing, China
[4]Institute for Stem Cell and Regeneration, CAS, Beijing 100101, China
[5]Beijing Institute for Stem Cell and Regenerative Medicine, Beijing 100101, China
[6]National Clinical Research Center for Geriatric Disorders, Aging Translational Medicine Center, International Center for Aging and Cancer, Xuanwu Hospital Capital Medical University, Beijing 100053, China
[7]State Key Laboratory of Brain and Cognitive Science, Institute of Biophysics, Chinese Academy of Sciences, Beijing 100101, China
[8]College of Life Sciences, University of Chinese Academy of Sciences, Beijing 100049, China
[9]Sino-Danish College, University of Chinese Academy of Sciences, Beijing 100049, China
[10]University of Chinese Academy of Sciences, Beijing 100049, China
[11]Hospital of Stomatology, Guanghua School of Stomatology, Guangdong Provincial Key Laboratory of Stomatology, Sun Yat-Sen University, Guangzhou 510060, China
[12]Chongqing Fifth People's Hospital, Chongqing 400060, China
[13]Beijing Institute of Heart, Lung and Blood Vessel Diseases, Beijing Anzhen Hospital, Capital Medical University, Beijing 100029, China
[14]International Center for Aging and Cancer, Hainan Medical University, Haikou 571199, China
[15]Altos Labs San Diego Institute of Science, San Diego, CA, USA
[16]Department of Neurosurgery, Xuanwu Hospital Capital Medical University, Beijing 100053, China
[17]National Medical Center for Neurological Diseases, Beijing 100053, China
[18]Beijing Municipal Geriatric Medical Research Center, Beijing 100053, China
[19]Oujiang Laboratory, Center for Geriatric Medicine and Institute of Aging, Key Laboratory of Alzheimer's Disease of Zhejiang Province, Zhejiang Provincial Clinical Research for Mental Disorders, The First-Affiliated Hospital, Wenzhou Medical University, Wenzhou, Zhejiang 325035, China
[20]Department of Rheumatology, Beijing Hospital, National Center of Gerontology, Institute of Geriatric Medicine, Clinical Immunology Center, Chinese Academy of Medical Sciences, Beijing 100730, China
[21]Institute of Gerontology, Guangzhou Geriatric Hospital, Guangzhou Medical University, Guangzhou, China
[22]Aging Biomarker Consortium (ABC), Beijing 100101, China
[23]These authors contributed equally
[24]Senior author
[25]Lead contact
*Correspondence: qujing@ioz.ac.cn (J.Q.), zhangwq@big.ac.cn (W.Z.), ghliu@ioz.ac.cn (G.-H.L.)
https://doi.org/10.1016/j.cell.2024.08.021

SUMMARY

In a rigorous 40-month study, we evaluated the geroprotective effects of metformin on adult male cynomolgus monkeys, addressing a gap in primate aging research. The study encompassed a comprehensive suite of physiological, imaging, histological, and molecular evaluations, substantiating metformin's influence on delaying age-related phenotypes at the organismal level. Specifically, we leveraged pan-tissue transcriptomics, DNA methylomics, plasma proteomics, and metabolomics to develop innovative monkey aging clocks and applied these to gauge metformin's effects on aging. The results highlighted a significant slowing of aging indicators, notably a roughly 6-year regression in brain aging. Metformin exerts a substantial neuroprotective effect, preserving brain structure and enhancing cognitive ability. The geroprotective effects on primate neurons were partially mediated by the activation of Nrf2, a transcription factor with anti-oxidative capabilities. Our research pioneers the systemic reduction of multi-dimensional biological age in primates through metformin, paving the way for advancing pharmaceutical strategies against human aging.

Please cite this article in press as: Yang et al., Metformin decelerates aging clock in male monkeys, Cell (2024), https://doi.org/10.1016/j.cell.2024.08.021

INTRODUCTION

Aging, a progressive process, induces tissue dysfunction and physiological deterioration, culminating in the emergence of age-related conditions, including neurodegenerative, cardiovascular, and diabetic disorders.[1–5] Notably, accumulating evidence suggests that aspects of aging are malleable in rodents through interventions including small-molecule drugs, genetic manipulations, exercise, and diet.[6–11] Metformin, a first-line treatment for type 2 diabetes, developed from a guanidine derivative in *Galega officinalis*, shows promise in slowing physiological aging across a range of models, including nematodes, fruit flies, and rodents.[12–21] Previous studies, including our own, also demonstrated metformin's potential to alleviate senescence in human diploid cells.[21–25] Moreover, retrospective studies indicate that metformin appears to reduce the mortality rate in diabetic patients.[26–28] However, whether metformin can delay aging and ameliorate aging-related tissue degeneration in primates remains unclear.

Leveraging high-throughput omics technologies, a cutting-edge toolkit for gauging biological aging has emerged, affording us the ability to precisely quantify aging rates at a molecular level.[29] Machine learning integration of epigenomics, transcriptomics, proteomics, and metabolomics data paves the way for "aging clocks," offering a means to evaluate the effectiveness of interventions against aging.[30–36] Additionally, the evolution of single-cell sequencing technologies enhances our comprehension of the intricate cellular and molecular underpinnings of the aging process and its interventions.[37] Yet the potential of metformin to catalyze systemic rejuvenation across various biological dimensions at the pan-tissue level remains to be fully understood.

To explore whether metformin alleviates age-related declines, we conducted a comprehensive, 40-month study assessing adult-onset metformin supplementation in aged primates. Specifically, our investigation encompassed a broad spectrum of analytical techniques, including physiological examinations, medical imaging, pan-tissue histological analysis, organism-wide transcriptomics, and single-nucleus RNA sequencing (snRNA-seq). By quantifying these parameters and integrating them into a comprehensive "primate aging clock," we provided evidence that metformin decelerates the aging process in male cynomolgus monkeys across various tissues. Importantly, our findings highlighted a notable neuroprotective effect of metformin, which was further validated using a human stem cell-derived neuronal senescence model. Our results affirm that extended metformin administration mitigates aging in primates, indicating its clinical potential for aging management and disease prevention.

RESULTS

Long-term metformin treatment exhibits geroprotective effects in primates

To assess whether long-term metformin therapy delays aging in healthy primates, we conducted a proof-of-concept study involving male cynomolgus monkeys (*Macaca fascicularis*) aged between 13 and 16 years, roughly equivalent to approximately 40–50 years in humans. At the start of the study, monkeys were evenly divided by age and randomly assigned to either the metformin or vehicle treatment groups (hereafter referred to as O-Met and O-Ctrl). The monkeys in the O-Met group were administered a daily dose of 20 mg/kg metformin, a standard dosage used in diabetes management for humans,[38,39] while being maintained under the same environmental and care conditions as the O-Ctrl group (Figure 1A). One participant in the O-Ctrl group succumbed to kidney failure on the 1,126th day of the study, as confirmed by a veterinarian. The remaining monkeys adhered to this regimen for a period of 1,200 days, approximately 3.3 years, which corresponds to about 10 years in humans.

Both groups underwent routine physical examinations every 3 months (Figure 1A). We observed that prolonged administration of metformin was not associated with compromised blood glucose homeostasis, nor did it lead to a reduction in body weight (Table S1). Similarly, we did not detect significant changes in the blood cell composition or the physiological characteristics of urine (Table S1).

We also included two additional control groups: young (3–5 years old) and middle-aged (10–12 years old) male adult cynomolgus monkeys, referred to as the Y-Ctrl group and M-Ctrl group, respectively. Once the O-Met group had completed 1,200 days of metformin treatment, we analyzed all four groups of monkeys for 68 biological parameters. These included morphometric indicators (BMI and organ indices), blood tests (routine blood tests, blood biochemical tests, and hormones), and imaging indicators (computed tomography [CT] scans and magnetic resonance imaging [MRI]) (Figure 1B). Taken together, these results implied the high safety profile of long-term metformin treatment (Table S1). Additionally, we noted that aging-associated periodontal bone loss was mitigated in the O-Met group relative to the O-Ctrl group (Figure 1C).

To evaluate memory, learning, and cognitive flexibility, we employed the Wisconsin General Test Apparatus (WGTA) method.[40,41] In the delay task, which evaluates memory retention, the O-Met group demonstrated higher accuracy in retrieving food after a delay compared with the O-Ctrl group, suggesting that metformin may enhance memory in aged animals (Figure 1D). Additionally, in the object discrimination task, the O-Met group showed superior learning abilities, indicating metformin's potential to improve learning in older subjects (Figure 1D). Likewise, in the object reversal learning, the O-Met group displayed enhanced cognitive resilience relative to the O-Ctrl group (Figure 1D).

When we investigated brain morphology using MRI, general linear mixed models (GLMMs) revealed reduced cortical thickness in aged monkeys compared with young ones, particularly in the frontal and temporal lobes (Figures 1E and S1A). In metformin-treated aged monkeys, frontal lobe cortical thickness was preserved, with a trend toward increased thickness in the parietal lobe, compared with the O-Ctrl group (Figures 1E and S1A). Consistently, histological examination revealed that metformin treatment enhanced the thickness of the frontal cortex, an area that typically thinned with age in monkeys (Figure 1F). By subdividing the brain into 88 regions using the CHARM5 atlas,[42] we identified 9 regions, predominantly in the frontal lobe, with a

Please cite this article in press as: Yang et al., Metformin decelerates aging clock in male monkeys, Cell (2024), https://doi.org/10.1016/j.cell.2024.08.021

CellPress

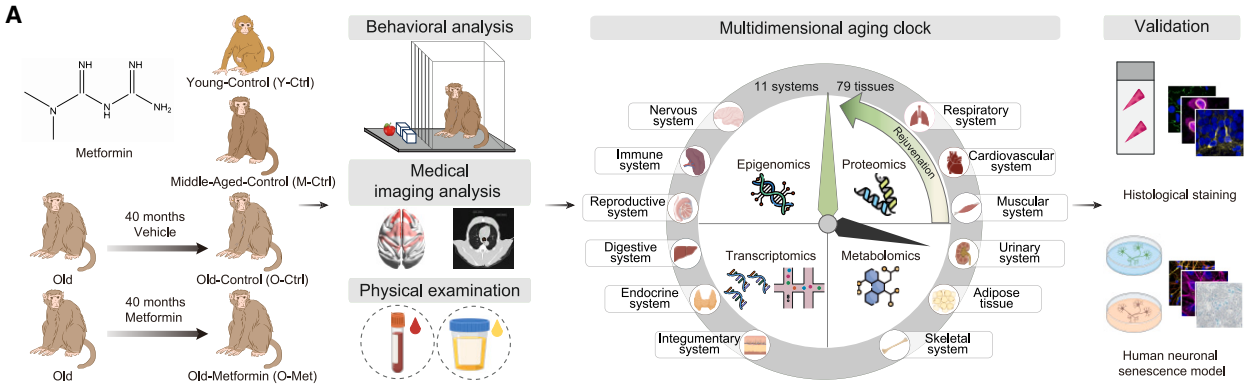

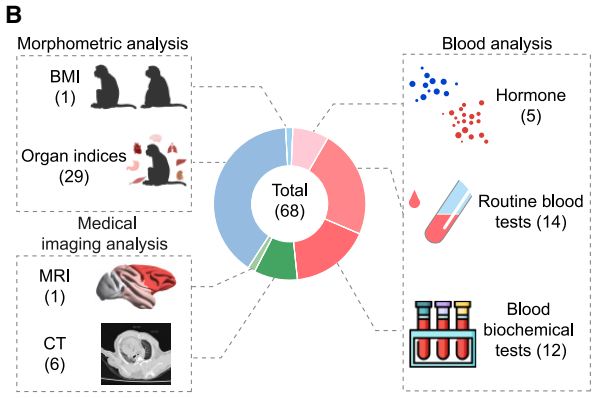

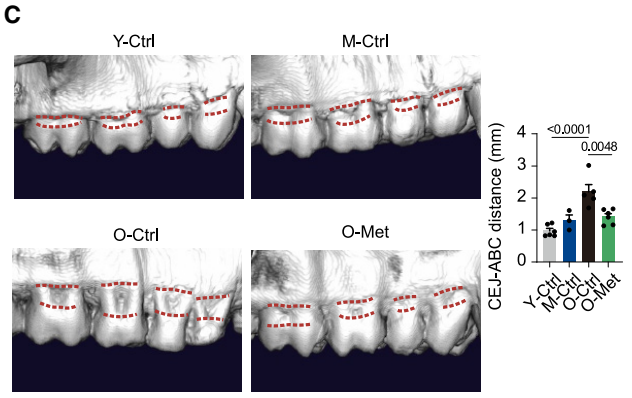

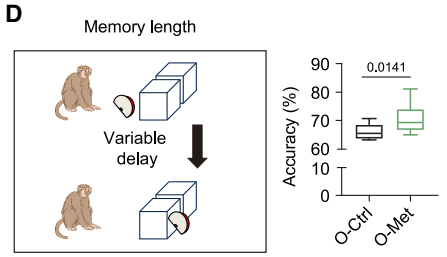

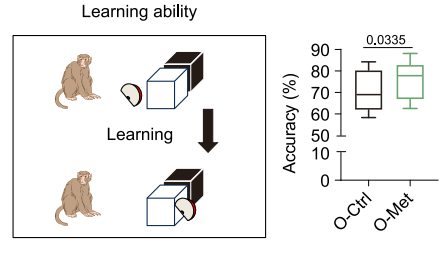

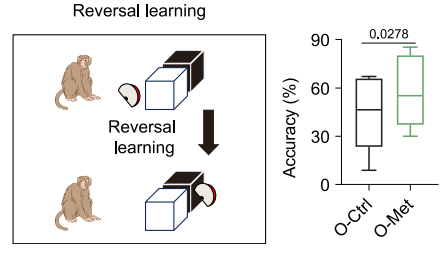

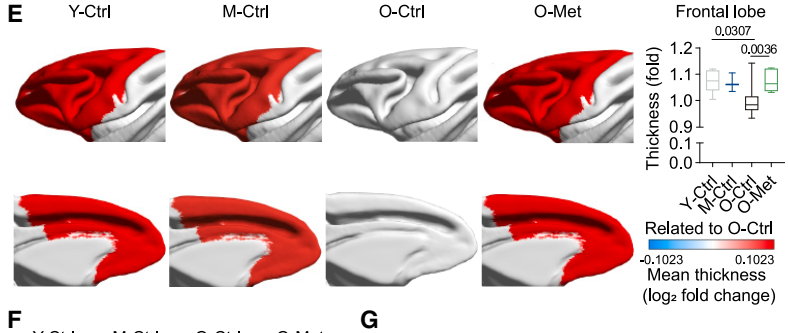

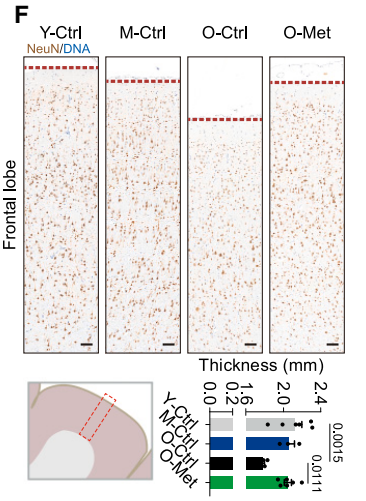

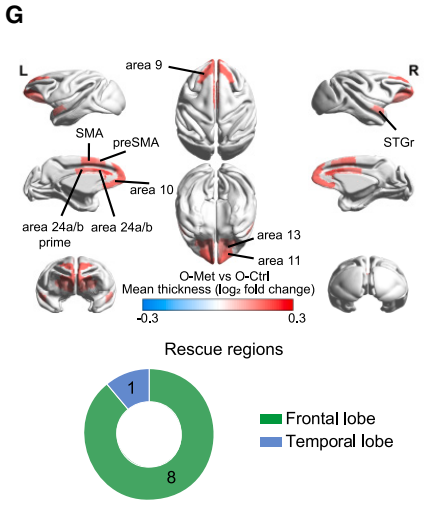

(legend on next page)

Please cite this article in press as: Yang et al., Metformin decelerates aging clock in male monkeys, Cell (2024), https://doi.org/10.1016/j.cell.2024.08.021

rescue in cortical thickness in metformin-treated monkeys (Figures 1G and S1B). These included cortical areas important for cognitive function (Figures 1G and S1B), namely orbital frontal cortex (OFC) (i.e., areas 10, 11, and 13), lateral prefrontal cortex (LPFC) (i.e., area 9), anterior cingulate cortex (ACC) (i.e., area 24a/b), midcingulate cortex (MCC) (i.e., area 24a/b prime), and motor cortex (i.e., preSMA and SMA), with OFC and LPFC known for roles in working memory, rule learning, and reversal learning.[43,44] Taken together, these findings, in conjunction with enhancements in memory and cognitive function, suggest that metformin might postpone aging-associated structural deterioration of the brain, particularly in the frontal lobe.

Metformin alleviates aging-related transcriptional fluctuations in multiple tissues

To gain molecular insights into primate aging and the systemic effects of metformin intervention, we conducted organism-wide and genome-wide RNA-seq analyses. In all, we profiled 79 tissues/organs (including the nervous, integumentary, endocrine, digestive, reproductive, immune, respiratory, cardiovascular, muscular, urinary, and skeletal systems) of cynomolgus monkeys of three different ages (Y-Ctrl, M-Ctrl, and O-Ctrl) and old monkeys that received metformin (O-Met) (Figures 2A and S2A). Initially, we performed a time-ordering analysis to dissect age-dependent transcriptional dynamics using Mfuzz c-means clustering. This analysis revealed four distinct clusters: cluster 1 with continuous upregulation (U), cluster 2 with continuous downregulation (D), cluster 3 with initial upregulation and subsequent downregulation (UD), and cluster 4 with earlier downregulation and then upregulation (DU) (Figures 2B and S2B). Genes in cluster U were predominantly related to innate immune response and inflammatory response, while those in cluster D were involved in extracellular matrix organization and developmental processes, reflecting a decline in tissue maintenance and regeneration capability during aging (Figure 2B).

Next, we investigated the impact of metformin on age-dependent transcriptomic changes at a tissue level. When we compared the trajectories between young, middle-aged, and old ("Y-Ctrl, M-Ctrl, to O-Ctrl") and between young, middle-aged, and metformin-treated old ("Y-Ctrl, M-Ctrl, to O-Met") monkeys, we found that metformin intervention was associated with global mitigation of age-dependent transcriptional dynamic changes in all four clusters. Gene set variation analysis (GSVA) demonstrated that metformin markedly rescued the expression of genes in clusters U and D, with less pronounced effects in the other two clusters (Figure 2C). To quantify the extent of metformin's effect in alleviating aging, we calculated a tissue-specific "rescue score" (see STAR Methods). Notably, metformin rescued most aged tissues (Figure 2D), with tissues like the frontal lobe, skin, liver, kidney, quadriceps muscle, and lung acquiring the highest rescue score across the 79 tissues in 11 systems (Figure 2D). When we used GSVA to characterize aging rescue at a pathway level, we identified that metformin treatment was associated with the inhibition of aging-related inflammatory response, apoptosis, fibrosis, and reactive oxygen species (ROS) pathways (Figures 2E, 2F, and S2C). Conversely, metformin treatment reactivated aging-repressed pathways typically involved in development and morphogenesis, including Wnt signaling, lipid metabolism, and DNA repair pathways (Figures 2E and 2F). In conclusion, our comprehensive atlas captures tissue transcriptional profiles that unravel the global geroprotective effect metformin exerts in primates.

Metformin attenuates various aging hallmarks across tissues

To validate our findings, we carried out comprehensive histological evaluations, focusing on the classic hallmarks of aging, particularly in tissues with higher rescue scores. Our initial observations indicated that metformin administration was associated with reduced aggregation of senescent cells, as denoted by fewer p21-positive cells in tissues such as the lung, liver, kidney (both cortex and medulla), heart, stomach, and skin of the O-Met group relative to the O-Ctrl group (Figure 3A). Furthermore, metformin treatment was associated with reduced expansion of aging-related fibrotic regions in the lung, kidney, and heart when compared with the O-Ctrl group (Figure 3B). Similarly, aging-related accumulation of lipid peroxidation within the urinary system, marked by 4-hydroxynonenal (4-HNE), was mitigated by

Figure 1. Behavioral and imaging assessments of cynomolgus monkeys following chronic metformin treatment

(A) Illustration of the long-term metformin treatment analysis workflow in cynomolgus monkeys. The graphical elements in this study's figures are sourced from BioRender.com and Flaticon.com.

(B) Illustration of morphometric analysis, medical imaging analysis, and blood analysis in cynomolgus monkeys.

(C) Micro-CT examination of alveolar bone in Y-Ctrl, M-Ctrl, O-Ctrl, and O-Met monkeys. The quantification data are shown as the means ± SEMs, and one-way ANOVA p values are indicated. Y-Ctrl, $n = 6$; M-Ctrl, $n = 3$; O-Ctrl, $n = 5$; O-Met, $n = 6$ monkeys.

(D) Performance of O-Ctrl and O-Met group monkeys in the delay task (top), discrimination task (middle), and reversal task (bottom) were assessed by utilizing the Wisconsin general test apparatus (WGTA). The boxes show the median (center line), the quartile range (25%–75%), and the whiskers (minimum and maximum). The ANOVA p values for the delay and discrimination tasks are noted, alongside the Mann-Whitney U test p values for the reversal task. See STAR Methods.

(E) Magnetic resonance imaging (MRI) assessment of frontal lobe cortical thickness in Y-Ctrl, M-Ctrl, O-Ctrl, and O-Met monkeys is presented. $\log_2$(fold change) in cortical thickness is displayed on the frontal lobe mid-gray surface, compared to the O-Ctrl group. Cortical thickness was obtained separately for each hemisphere of individual monkeys. Data for cortical thickness are presented as the mean value across both hemispheres for each monkey. The boxes show the median (center line), the quartile range (25%–75%), and the whiskers (minimum and maximum), with GLMM analysis p values annotated. See STAR Methods.

(F) Immunohistochemical evaluation of NeuN in the frontal lobe of brains from Y-Ctrl, M-Ctrl, O-Ctrl, and O-Met monkeys is illustrated. Scale bars, 100 μm. Y-Ctrl, $n = 6$; M-Ctrl, $n = 3$; O-Ctrl, $n = 5$; O-Met, $n = 6$ monkeys. The quantified data are shown as means ± SEMs, one-way ANOVA with Tukey's multiple comparisons test p values are indicated.

(G) MRI was employed to examine 88 brain regions in Y-Ctrl, M-Ctrl, O-Ctrl, and O-Met monkeys. The visualization emphasizes areas with significant ($p < 0.05$) changes in cortical thickness due to metformin-induced rejuvenation. A pie chart illustrates the proportion of brain regions experiencing metformin-induced rejuvenation across the cerebral lobes. See STAR Methods.

See also Figure S1 and Table S1.

Please cite this article in press as: Yang et al., Metformin decelerates aging clock in male monkeys, Cell (2024), https://doi.org/10.1016/j.cell.2024.08.021

CellPress

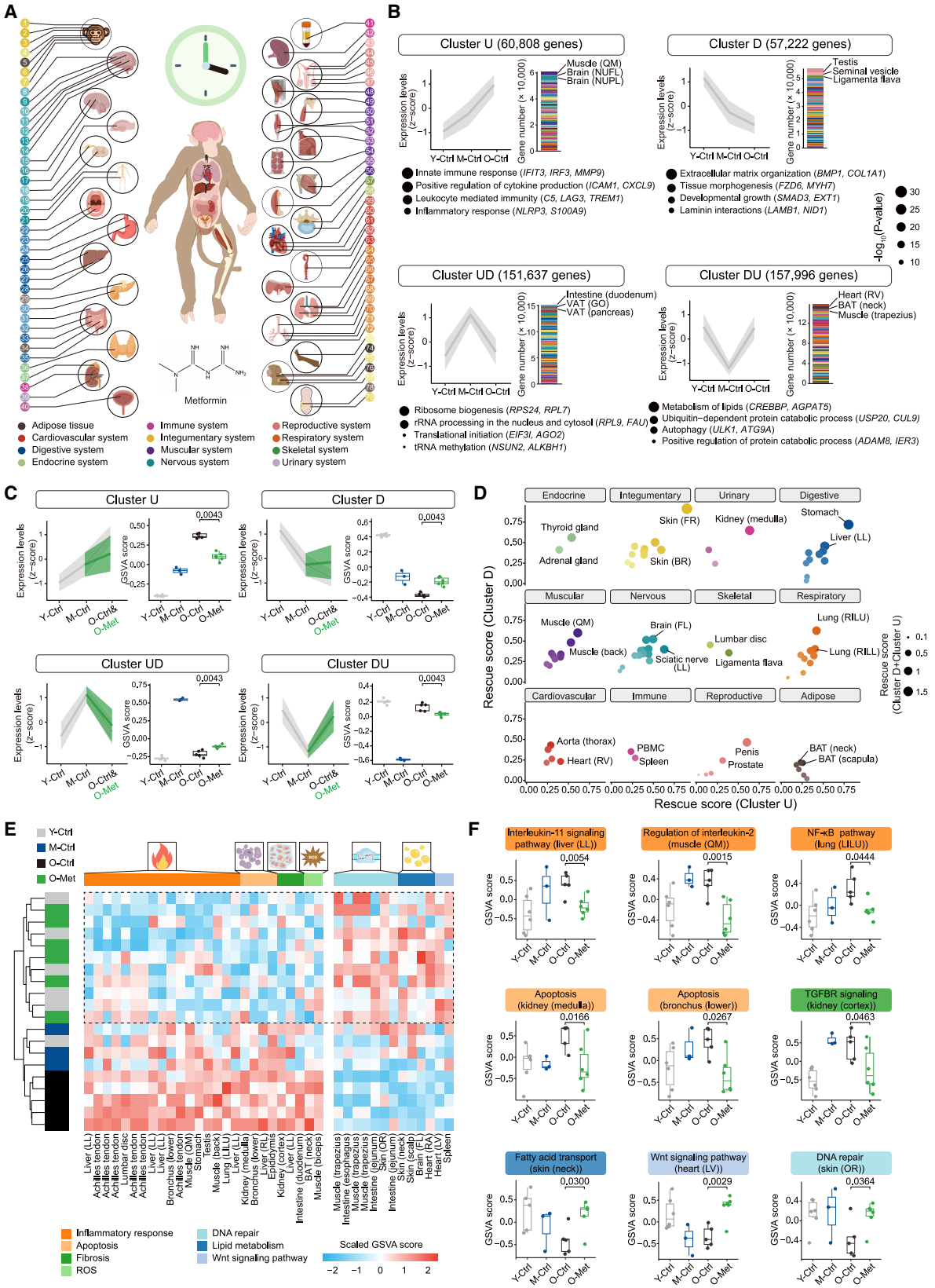

(legend on next page)

Please cite this article in press as: Yang et al., Metformin decelerates aging clock in male monkeys, Cell (2024), https://doi.org/10.1016/j.cell.2024.08.021

metformin treatment (Figure S3A). Additionally, in O-Met monkey tissues, metformin was effective in rectifying indicators of epigenetic instability associated with aging, such as the loss of H3K9me3 and the up-regulated expression of endogenous retrovirus (ERV) proteins (Figures S3B and S3C). Moreover, the decline of fast II fibers, a key indicator of skeletal muscle aging, was counteracted by metformin treatment (Figure S3D).

Strikingly, we detected a widespread, potent effect of metformin in curbing chronic inflammation, a cardinal hallmark of aging that underlies almost all aging-related diseases.[7,9,45,46] Metformin supplementation was associated with reduced aging-associated inflammatory areas within the liver and stomach and less immune cell infiltration in the lung, liver, and kidney (Figures 3C and 3D). We also noted that metformin treatment was associated with a blunted escalation of senescence-associated secretory phenotype (SASP) factors, including tumor necrosis factor-α (TNF-α), interleukin-1β (IL-1β), S100 calcium-binding protein A8 (S100A8), and matrix metalloproteinase 9 (MMP9) across the array of tissues examined (Figures 3E–3G and S3E). In summary, our findings underscore that metformin efficiently reduces the emergence of aging hallmarks, including tissue degeneration and inflammation, in primates.

Reduction of multi-omics biological age by metformin

To quantify metformin-induced deceleration of biological age, we established computational models of monkey aging clocks based on multi-omics data. In addition to pan-tissue transcriptomic profiles, we obtained DNA methylation profiles to construct DNA methylation clocks for tissues with top-ranking transcriptional rescue scores. Furthermore, we generated a quantitative plasma proteomics dataset and metabolomics signatures using mass spectrometry (Figures S4A–S4E). By integrating data from the Y-Ctrl, M-Ctrl, and O-Ctrl cohorts (a total of 36 monkeys), we were able to formulate a penalized linear model (see STAR Methods). This model enabled the estimation of the biological age for each monkey and the calculation of ΔAge as the discrepancy between the predicted biological age and the expectation of that measurement for the monkey's chronological age.[32,47] The difference in ΔAge between the O-Met group and the O-Ctrl group was quantified as ΔAgeDiff (see STAR Methods for details). To this end, we employed the ElasticNet method to quantify biological age indicators, including DNAmAge (based on DNA methylation), transcriptAge (based on the transcriptome), proteinAge (based on the proteome), and metabAge (based on the metabolome), for each monkey (Figure 4A; Table S3).

This analysis estimated that metformin administration resets the proteinAge of treated monkeys by an average of −6.41 years (Figure 4B). In tissues with a notable transcriptome aging rescue, DNAmAge was also rescued, including the frontal lobe, lung, kidney (cortex), liver, and skin, which were restored by an average of −6.10, −5.11, −4.90, −3.95, and −2.65 years, respectively (Figure 4C). Given these data, we investigated the impact of metformin on biological age at the transcriptomic level in each tissue. Our analysis revealed that the transcriptAge of all thirteen tissues was restored to a younger state, including the Achilles tendon (ΔAgeDiff −5.31 years), liver (ΔAgeDiff −4.14 years), bronchus (ΔAgeDiff −3.71 years), muscle (ΔAgeDiff −3.56 years), and lung (ΔAgeDiff −3.40 years) (Figure 4D and Table S3). Collectively, our findings demonstrate that metformin intervention delays aging across various tissues and different omic layers, as evidenced by the measurement of biological age.

Metformin slows liver aging and enhances hepatoprotection in aged monkeys

The liver, functioning as a metabolic organ, exhibited substantial metformin-associated reductions in both DNAmAge (with an ΔAgeDiff of approximately −3.95 years) and transcriptAge (with an ΔAgeDiff of about −4.14 years) (Figures 4C and 4D). To more precisely analyze the interventional effects of metformin, we performed snRNA-seq on liver samples from the Y-Ctrl, M-Ctrl, O-Ctrl, and O-Met groups (Figures 5A and S5A–S5C).

Subsequently, we developed "single-nucleus transcriptomic aging clocks" referred to as sn-transcriptAge, leveraging snRNA-seq data spanning from young to middle-aged to old age, to characterize aging and aging deceleration at the cell-type level.[48] First, we identified differentially expressed genes

Figure 2. Metformin reversed age-related gene expression in a variety of tissues throughout the monkey body

(A) Schematic diagram showing 79 tissues across 11 systems in transcriptomic analysis. (1) Skin (scalp); (2) skin (FR); (3) skin (OR); (4) skin (IR); (5) SAT (face); (6) skin (BR); (7) skin (MR); (8) brain (PFL); (9) brain (FL); (10) brain (PL); (11) brain (TL); (12) brain (OL); (13) brain stem; (14) cerebellum; (15) brain (NUFL); (16) brain (NUPL); (17) brain (hippocampus); (18) dorsal root ganglion; (19) spinal cord; (20) median nerve (UL); (21) sciatic nerve (LL); (22) gingiva; (23) tongue; (24) esophagus; (25) stomach; (26) liver (RL); (27) liver (ML); (28) liver (LL); (29) VAT (pancreas); (30) pancreas; (31) intestine (duodenum); (32) intestine (jejunum); (33) intestine (ileum); (34) VAT (GO); (35) intestine (SC); (36) thyroid gland; (37) adrenal gland; (38) kidney (medulla); (39) kidney (cortex); (40) bladder; (41) PBMC; (42) spleen; (43) seminal vesicle; (44) prostate; (45) penis; (46) epididymis; (47) testis; (48) muscle (back); (49) supraspinatus tendon; (50) muscle (biceps); (51) muscle (gastrocnemius); (52) Achilles tendon; (53) muscle (trapezius); (54) muscle (abdomen); (55) muscle (glute); (56) muscle (quadriceps); (57) ligamentum flavum; (58) lumbar disc; (59) heart (RA); (60) heart (LV); (61) heart (RV); (62) aorta (arch); (63) aorta (thorax); (64) diaphragm; (65) lung (RILU); (66) lung (LILU); (67) lung (RILL); (68) lung (LILL); (69) trachea (upper); (70) trachea (lower); (71) bronchus (upper); (72) bronchus (lower); (73) skin (hand); (74) BAT (neck); (75) skin (neck); (76) BAT (scapula); (77) skin (back); (78) SAT (abdomen); and (79) skin (belly). The full names of tissues are listed in Table S1.

(B) Transcriptomic data clustering analysis from monkey tissues, with the count of age-dependent genes per cluster displayed. Solid lines and ribbons represent mean of standardized FPKM across clusters ± SDs.

(C) Left, expression changes of age-dependent genes from monkeys upon metformin treatment. Solid lines and ribbons represent mean of standardized FPKM across clusters ± SDs. Right, box plot showing GSVA score of age-dependent genes in different groups. Wilcoxon rank-sum test p values are indicated.

(D) The dot plot illustrates the rescue score for various aged tissues post metformin treatment. Initially, the gene expression of persistently up-regulated and down-regulated aging genes (clusters U and D) was quantified across monkey organs from different groups using the GSVA algorithm.

(E) Heatmap showing the rescue pathways related to aging based on GSVA score.

(F) Boxplot showing the selected rescue pathways compared with specific tissue. Moderated t tests p values using limma are indicated.

See also Figure S2 and Table S2.

Please cite this article in press as: Yang et al., Metformin decelerates aging clock in male monkeys, Cell (2024), https://doi.org/10.1016/j.cell.2024.08.021

CellPress

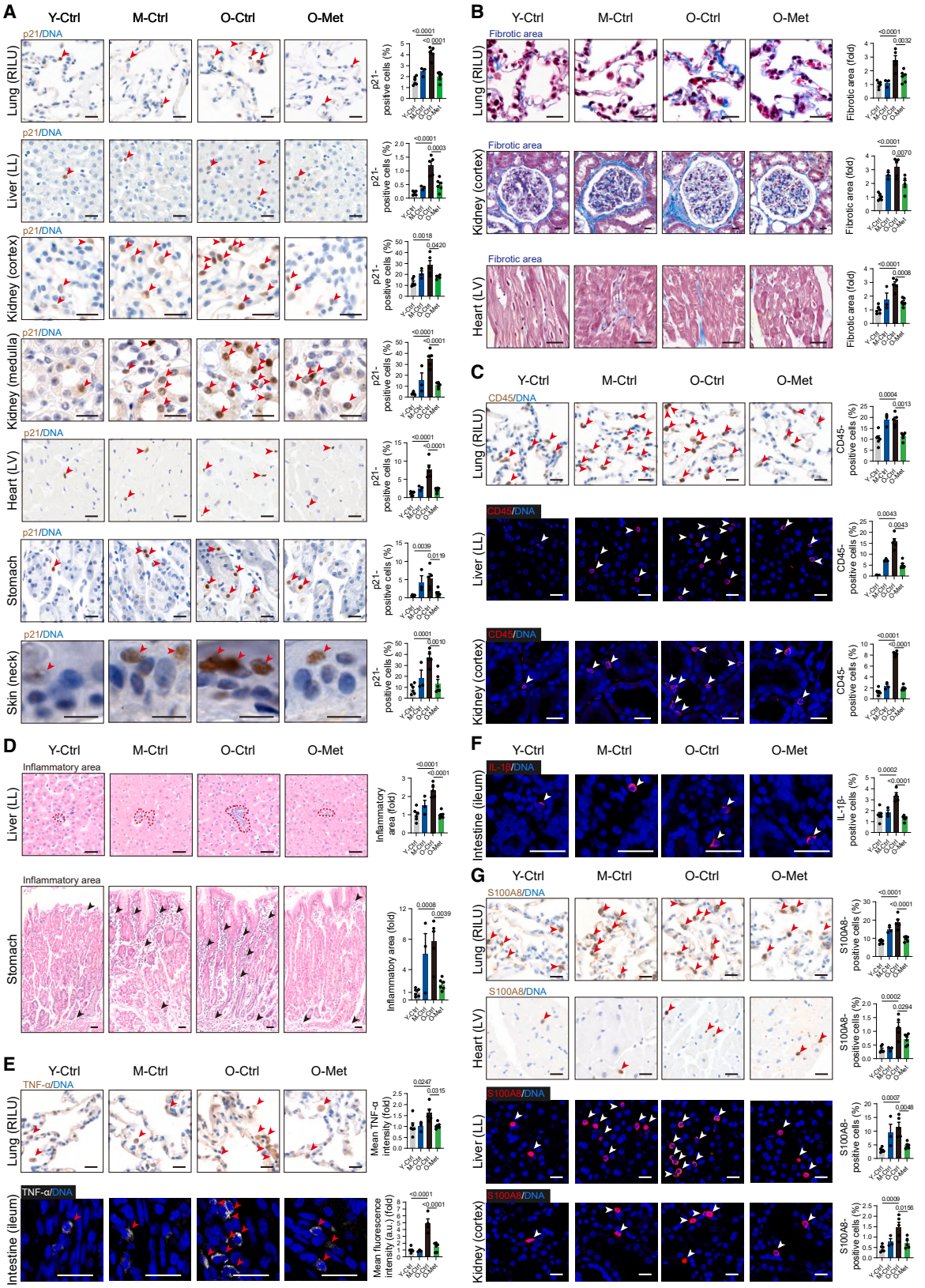

(legend on next page)

Please cite this article in press as: Yang et al., Metformin decelerates aging clock in male monkeys, Cell (2024), https://doi.org/10.1016/j.cell.2024.08.021

(DEGs) by comparing any two groups among the Y-Ctrl, M-Ctrl, and O-Ctrl cohorts with a cutoff of $|\log_2(\text{fold change})| > 0.25$ and an adjusted p value < 0.05, which we designated as age-dependent DEGs (Table S4). Utilizing the expression matrix of these aging DEGs as input data and the chronological ages of each monkey as the training label, we employed an ElasticNet model to construct single-nucleus aging clocks, which we refined using leave-one-out (LOO) cross-validation techniques to augment its predictive precision (see STAR Methods). By combining all cell-type data points into a singular input matrix, we developed an integrated model predicting that metformin treatment could rejuvenate the liver by an average of 4.28 years (Figure 5B). Notably, three specific cell types—hepatocytes, Kupffer cells, and T cells—demonstrated an obvious rescue to a more youthful state, with their sn-transcriptAge showing an average regression of 5.83, 6.66, and 6.43 years, respectively (Figure 5B).

Metformin treatment markedly restored the expression of genes that were consistently up-regulated (cluster U) or down-regulated (cluster D) in the O-Ctrl group relative to the Y-Ctrl and M-Ctrl groups (Figures S5D and S5E). Overall, metformin rescued approximately 33.9% of cluster U DEGs and 21.2% of cluster D DEGs (Figure S5F). More specifically, different cell types are associated with different rescue effects, with marginal pro-aging effects (Figure S5G). Gene function annotation revealed that cluster D genes are predominantly involved in essential metabolic functions in hepatocytes, including lipid transport (e.g., *ABCA9*, *HACL1*, and *SLC22A7*) and lipid catabolism (e.g., *HACL1*, *CYP4F12*, and *PNPLA3*), as well as amino acid catabolism (e.g., *ARG1*, *GNMT*, and *SHMT1*) (Figure S5D). These results suggest that metformin treatment can mitigate aging-induced impairment of liver metabolism. By contrast, cluster U genes were enriched in pathways such as immune response (e.g., *LBP*, *C4BPA*, and *C4BPB*) and the transforming growth factor-β (TGF-β) pathway (e.g., *SMAD3*, *TGFBR1*, and *TGFBR3*), as well as inflammatory responses in multiple cell types (Figure S5D).[49,50] Suppression of cluster U genes in O-Met monkeys correlated with a reduced inflammatory and fibrotic state (Figure S5H).

When we ranked the proportion of rescued DEGs, along with the Augur score (a metric that assesses the sensitivity of each cell type to specific treatments), we identified Kupffer cells, hepatocytes, and T cells as the top three rescued cell types, aligning with our biological age estimations (Figures S6A and S6B). Furthermore, the top aging-related and rescued bulk RNA-seq DEGs were primarily attributed to transcriptional changes in hepatocytes (Figure S6C), highlighting their pivotal role in both aging and its attenuation through metformin treatment. Consistently, gene expression trajectories revealed that the expression of hepatocyte-specific clusters U and D genes was robustly restored to a youthful state following metformin treatment (Figure S6D). Specifically, pathways indicative of hepatocyte senescence,[51–55] including inflammatory responses (e.g., *CRP*, *LBP*, and *SERPINA3*), and metabolism of lipids (e.g., *ABCB11*, *HACL1*, and *SCP2*) in the O-Met group, were restored to a state resembling Y-Ctrl rather than O-Ctrl (Figures S6E and S6F). In line with the bioinformatic analyses, histology analysis confirmed that increased expression of apolipoprotein E (APOE), a lipoprotein particle component recently identified as a biomarker of aging,[56,57] was reset to a youthful state (Figures S6G and S6H). Through Oil red O staining, we validated that the age-associated abnormal accumulation of lipid droplets was mitigated in the O-Met group (Figure S6H). Additionally, metformin reduced TNF-α levels and fibrosis, which were elevated during aging in the liver (Figures S6I and S6J). Collectively, these results demonstrate that metformin protects liver function potentially by enhancing the metabolic functions of hepatocytes.

Metformin retards brain aging and provides neuroprotection in elderly monkeys

With improvements noted in brain structure and function following metformin treatment, and considering the frontal lobe exhibited the most notable rescue in DNAmAge (Figure 4C), our next step was to explore the geroprotective effects of metformin in the frontal lobe. Using the same approach as with the liver, we performed snRNA-seq on frontal lobe samples from all four monkey groups (Figures 5C and S7A). As we had done in the liver snRNA-seq analysis, we trained ElasticNet models to gauge the comprehensive transcriptomic landscape of the frontal lobe (Figures 5D and 5E). Intriguingly, we found that the majority of cell types after metformin treatment reverted to a more youthful stage, exhibiting reduced sn-transcriptAge. By integrating data from all cell types into a unified model, we were able to determine

Figure 3. Metformin mitigated multiple aging hallmarks across monkey tissues

(A) Immunohistochemical assessment of p21 in the lung, liver, kidney, heart, stomach, and skin of Y-Ctrl, M-Ctrl, O-Ctrl, and O-Met monkeys. The arrows indicate p21-positive cells. Scale bars of lung, liver, kidney, heart, and stomach, 20 μm; scale bars of skin, 10 μm.

(B) Masson's trichrome staining evaluation of lung, kidney, and heart in Y-Ctrl, M-Ctrl, O-Ctrl, and O-Met monkeys. Scale bars, 20 μm.

(C) Immunohistochemical and immunofluorescent examination of CD45 of the lung, liver, and kidney in Y-Ctrl, M-Ctrl, O-Ctrl, and O-Met monkeys. The arrows indicate CD45-positive cells. Scale bars, 20 μm.

(D) Hematoxylin and eosin (H&E) staining assessment of liver and stomach in Y-Ctrl, M-Ctrl, O-Ctrl, and O-Met monkeys. The dashed circles and arrows indicate inflammatory area. Scale bars, 40 μm.

(E) Immunohistochemical and immunofluorescent examination of TNF-α in lung and intestine in Y-Ctrl, M-Ctrl, O-Ctrl, and O-Met monkeys. The arrows indicate TNF-α-positive cells. Scale bars, 20 μm.

(F) Immunofluorescent examination of IL-1β in intestine in Y-Ctrl, M-Ctrl, O-Ctrl, and O-Met monkeys. The arrows indicate IL-1β-positive cells. Scale bars, 20 μm.

(G) Immunohistochemical and immunofluorescent examination of S100A8 in lung, heart, liver, and kidney in Y-Ctrl, M-Ctrl, O-Ctrl, and O-Met monkeys. The arrows indicate S100A8-positive cells. Scale bars, 20 μm.

The quantified data in (A)–(G) are shown as means ± SEMs, Mann-Whitney test p values of liver in (C) are indicated, one-way ANOVA with Tukey's multiple comparisons test p values of (A) and (B), and lung and kidney in (C) and (D)–(G) are indicated. Y-Ctrl, $n = 6$; M-Ctrl, $n = 3$; O-Ctrl, $n = 4$–5; O-Met, $n = 5$–6 monkeys in (A)–(G).

See also Figure S3.

Please cite this article in press as: Yang et al., Metformin decelerates aging clock in male monkeys, Cell (2024), https://doi.org/10.1016/j.cell.2024.08.021

CellPress

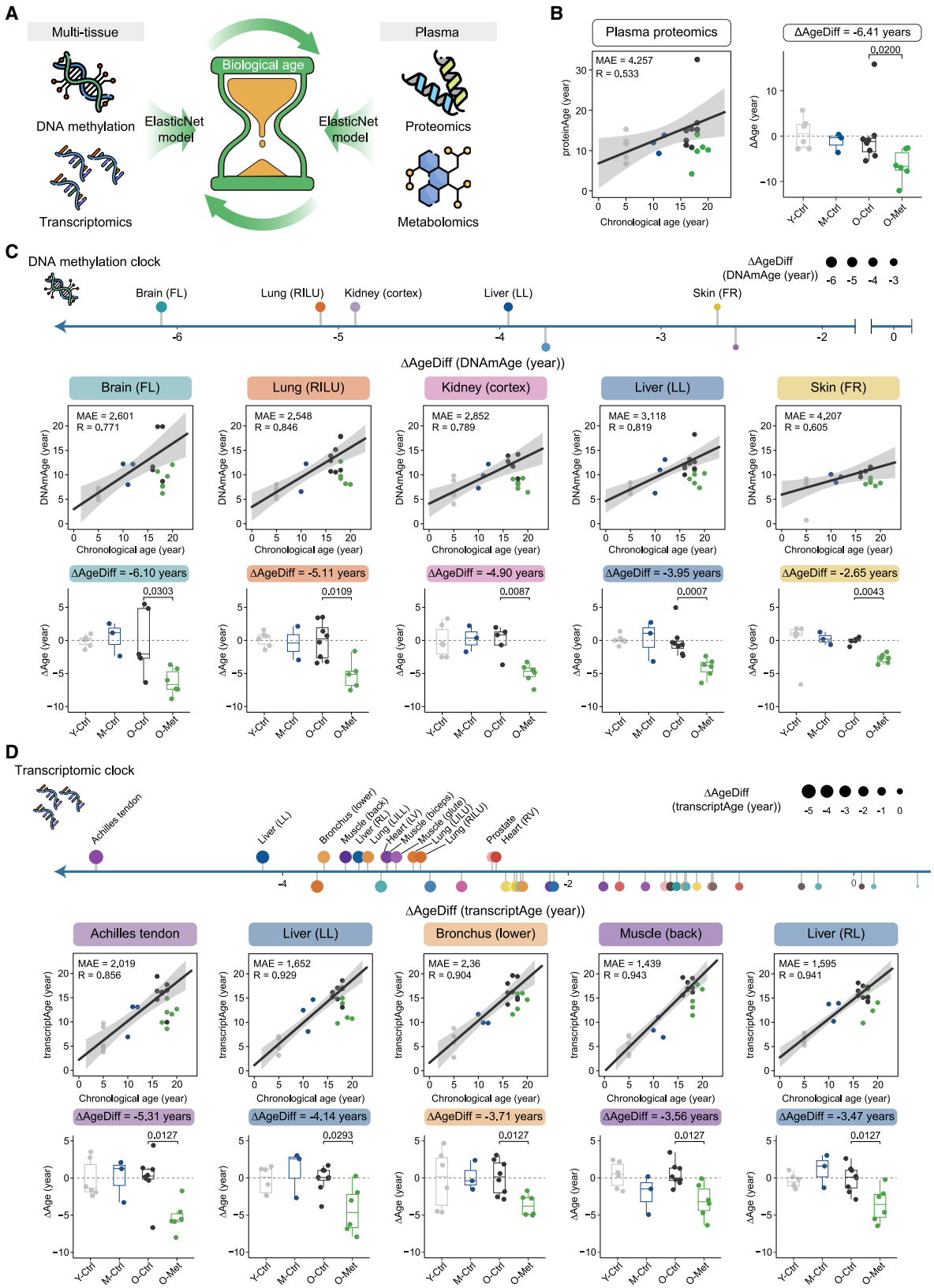

(legend on next page)

Please cite this article in press as: Yang et al., Metformin decelerates aging clock in male monkeys, Cell (2024), https://doi.org/10.1016/j.cell.2024.08.021

that metformin treatment rescued the frontal lobe of monkeys by an average of 5.90 years (Figure 5D). Subsequently, improvement of sn-transcriptAge was notably observed in inhibitory neuron (InN) (ΔAgeDiff −5.59 years), excitatory neuron (ExN) (ΔAgeDiff −5.45 years), as well as microglia (ΔAgeDiff −6.86 years), oligodendrocyte (OL) (ΔAgeDiff −6.79 years), astrocyte (ΔAgeDiff −6.08 years), and oligodendrocyte progenitor cell (OPC) (ΔAgeDiff −5.70 years) (Figure 5E).

Metformin treatment markedly rescued gene repression in all four clusters (U, D, UD, and DU) and cell types, consistent with the rescue in biological age (Figures S7D and S7E). In O-Met monkeys, analysis of aging DEGs in cluster U that consistently increased with aging were rescued by 30.1%, whereas those in cluster D that consistently decreased with aging were rescued by 28.0%, respectively (Figure S7F). Gene Ontology (GO-term) analysis indicated that genes pivotal for neuronal function, such as dendrite morphogenesis/extension and synapse assembly, were down-regulated during aging in ExN, InN, OL, OPC, microglia, and astrocyte but were restored by metformin treatment (Figure 5F). By contrast, pathways that were up-regulated during aging, including activation of the immune response, complement activation, and regulation of the TGF-β receptor signaling pathway, were reset to lower levels by metformin treatment (Figure 5F). We also investigated whether metformin has potential side effects by exacerbating the expression changes of aging DEGs, and found that the number of pro-aging DEGs in all cell types captured by snRNA-seq is very limited, suggesting that metformin's pro-aging impact at this dosage is likely manageable (Figures S7G and S7H). Experimentally, we verified that markers associated with brain aging and the progression of neurodegenerative diseases were restored by metformin treatment to levels similar to those observed in young monkeys. This includes a reduction in SA-β-gal-positive cells, p-Tau (T181) accumulation, and a decrease in pro-inflammatory factors like MMP9 (Figure 5G). Additionally, we observed that the reduced myelin sheath thickness, a characteristic of aged monkeys, was rebuilt to a younger state following metformin treatment (Figure 5G).

Next, the Augur score assessment highlighted that ExN underwent the most pronounced metformin-induced geroprotective effects (Figure 6A). Given the critical role of ExN in cognitive function, we conducted an in-depth analysis of frontal lobe ExNs (Figures 6A–6C). Gene set enrichment analysis (GSEA) indicated that pathways typically down-regulated with aging, such as synaptic membrane adhesion, dendrite morphogenesis, and neurogenesis, were restored by metformin treatment (Figure 6B). Additionally, genes associated with neuronal protection, which were typically suppressed with aging, were up-regulated by metformin. Conversely, genes linked to neuronal aging and apoptosis were down-regulated by the metformin (Figure 6C). These results were further supported by a series of histological assays, which provided compelling evidence of neuroprotection of metformin. Specifically, metformin treatment reduced the proportion of SPiDER-β-gal-positive neurons, and mitigated the loss of nuclear envelope integrity (Figures 6D and 6E). Additionally, the drug alleviated abnormal protein accumulation within neurons, as indicated by a reduction in cytosolic aggresome and amyloid-β (Aβ) accumulation (Figure 6F). Metformin also enhanced neuronal regeneration and synaptic connectivity, as evidenced by dendrite elongation, a critical aspect of neuronal structural plasticity and functional capability (Figure 6G). Furthermore, in the hippocampus, a brain region particularly vulnerable to aging, we detected a reduced accumulation of microglia, a cell type implicated in numerous neurodegenerative diseases and aging, and restoration of neuronal nuclear envelope integrity (Figure 6H). Additionally, metformin increased neural precursor activity in the hippocampal region (Figure 6H). These results collectively suggest that metformin, by countering age-related cellular alterations, provides comprehensive neuroprotection against the detrimental effects of aging.

Metformin autonomously mitigates neuronal senescence in an Nrf2-dependent manner

Subsequently, we utilized our established *in vitro* model using human embryonic stem cell (hESC)-derived neurons to assess the potential geroprotective effects of metformin (Figures S8A–S8C).[58,59] Treatment with low-dose metformin (5 μM) over 15 days alleviated indicators of neuronal senescence, including decreased SA-β-gal activity, lessened aggresome and Aβ accumulation, lowered IL-6 expression, and restored lamin B2 levels (Figures 7A–7C and S8D–S8F). These findings suggest that metformin could decelerate human neuronal aging through a cell-autonomous mechanism.

Upon evaluating the protein levels of potential downstream effectors of metformin, we observed that metformin treatment restored the active form of nuclear factor erythroid-derived 2-like 2 (phosphorylated Nrf2), a pivotal regulator of cellular antioxidant response that typically decreased during prolonged

Figure 4. Multi-omics analysis of biological aging in metformin-treated monkeys

(A) Schematic overview of multi-tiered biological age assessment in monkeys administered metformin.

(B) Dot plot depicting predicted biological age (proteinAge) derived from plasma proteomics (left). Boxplot illustrating the rescue of monkey's proteinAge by metformin (right).

(C) Lollipop chart displaying the monkey multi-tissue biological age (DNAmAge) by metformin, based on DNA methylation data (top). Dot plot illustrating significant ($p < 0.05$) metformin-induced rescue of tissue's DNAmAge, ranked by ΔAgeDiff, based on tissue DNA methylation data (middle section). Boxplot depicting the rescue of monkey's DNAmAge by metformin treatment (bottom).

(D) Lollipop chart illustrating the monkey multi-tissue biological age (transcriptAge) by metformin, based on bulk RNA-seq data (top). Dot plot highlighting the top 5 metformin-induced tissue rescues (ranked by ΔAgeDiff) in transcriptAge, based on tissue bulk RNA-seq data (middle section). Boxplot representing the reduction of monkey's transcriptAge following metformin treatment (bottom).

The rescued tissues in (C) and (D) were placed above the horizontal line, and the dots representing the tissue are colored according to the colors in Figure 2A. The dashed line in (B)–(D) signifies no difference between the predicted biological age and the expected value for the monkey's actual age (ΔAge = 0), with the distance from the dot to the line indicating the individual's aging pace. Wilcoxon rank-sum test p values in (B)–(D) are indicated.

See also Figure S4 and Table S3.

Please cite this article in press as: Yang et al., Metformin decelerates aging clock in male monkeys, Cell (2024), https://doi.org/10.1016/j.cell.2024.08.021

CellPress

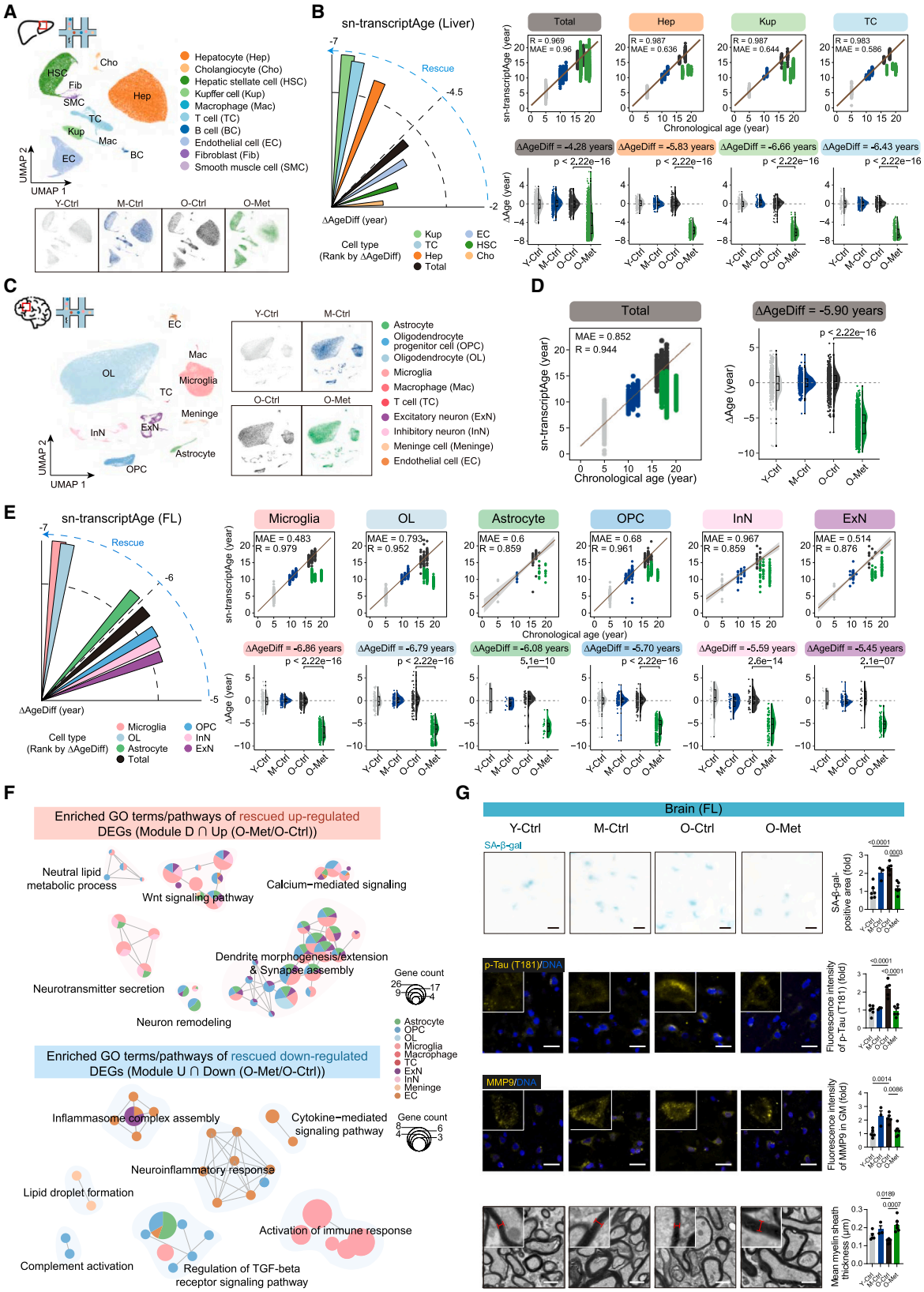

(legend on next page)

Please cite this article in press as: Yang et al., Metformin decelerates aging clock in male monkeys, Cell (2024), https://doi.org/10.1016/j.cell.2024.08.021

neuronal culture (Figures S8G and S8H). Metformin treatment resulted in increased nuclear phosphorylated Nrf2, accompanied by the up-regulation of Nrf2 target genes like *HO-1*, *NQO-1*, *SOD3*, *GPX2*, and *GPX1*, which were generally suppressed and typically down-regulated during human neuron (hNeuron) senescence (Figures 7D, 7E, S8I, and S8J). Consistently, metformin treatment decreased the expression of 4-HNE, a lipid peroxide product, and ROS levels, indicating lower oxidative stress levels in O-Met tissues compared with those in O-Ctrl groups (Figures 7F and S8K). Furthermore, a subset of metformin-induced gene expression changes in hNeurons was partially mirrored *in vivo* (Figure S8L). We observed no significant changes in mitochondrial gene expression or mtDNA content in senescent hNeurons after metformin treatment (Figures S8M–S8P). These results suggest that elevated Nrf2 activity may mediate the geroprotective effect of metformin in primate neurons.

To validate our hypothesis, we manipulated Nrf2 activity in hNeurons using two approaches. Firstly, we knocked down Nrf2 using small interfering RNAs (siRNAs) (Figures 7G, S9A, and S9B), leading to diminished nuclear levels of active Nrf2 and its target genes, even in the presence of metformin (Figures 7H, 7J, S9C, and S9D). Nrf2 repression accelerated neuronal senescence, which could not be slowed down by metformin treatment (Figures 7I and 7J). These observations indicate that metformin's neuroprotective effects are, at least in part, contingent upon Nrf2 activity. Secondly, we generated hNeurons featuring an engineered E82G Nrf2 variant that enhances Nrf2 activation by obstructing KEAP1 binding (Figures 7K, S9E, and S9F).[60,61] This genetic enhancement strategy potently activated the Nrf2 pathway, evident in heightened nuclear Nrf2 phosphorylation, elevated target gene expression, and lowered oxidative markers like 4-HNE and ROS in Nrf2 E82G neurons, contrasting with the wildtype (Figures 7L, 7N, and S9G–S9I). Consequently, cellular senescent phenotypes observed in the prolonged culture of hNeurons were rescued (Figures 7M and 7N). Furthermore, the geroprotective impact from Nrf2's constitutive activation surpassed that of metformin alone, and metformin did not enhance these effects when used in conjunction with the Nrf2 E82G mutation (Figures 7M and 7N). These findings align with the levels of nuclear-localized phosphorylated Nrf2, suggesting that Nrf2 pathway activation is a key mechanism in metformin's role in delaying human neuronal aging. Consistent with our *in vitro* findings, Nrf2 pathway activation was also detected across multiple tissues in metformin-treated monkeys, including frontal lobe neurons (Figures 7O, 7P, and S9J). In summary, metformin decelerates neuronal aging and, by extension, brain aging, largely via Nrf2 pathway activation.

DISCUSSION

Over 3 years, we evaluated metformin's systemic geroprotective effects in healthy monkeys, taking advantage of their physiology and organ structure akin to humans, as well as their disease and medication responses.[58,62–65] Our results indicate metformin's capacity to ameliorate aging across the primate body, with multidimensional aging clocks showing a rejuvenation trend post-treatment. Given aging's complexity,[66–69] a thorough appraisal of geroprotective interventions is essential.[32,70,71] Our study reveals metformin's tissue- and cell-specific geroprotective actions, notably enhancing cognitive performance in primates. Supported by evidence of metformin crossing the blood-brain barrier even at 5 μM concentrations,[72–77] providing neuroprotection, these findings suggest metformin's potential in slowing brain aging and possibly treating neurodegenerative and other chronic conditions.[78–80]

Beyond its diabetes management role,[38,81] our study indicates metformin has a minimal effect on blood sugar in healthy elderly monkeys (Table S1). We demonstrate that metformin decelerates neuronal senescence and brain aging, primarily via cell-autonomous pathways with Nrf2's intrinsic antioxidant mechanisms playing a critical role. Distinguishing from metformin's established protective mechanisms through AMP-activated

Figure 5. Metformin mitigates liver and frontal lobe aging in monkeys

(A) UMAP plot illustrating the distribution of distinct liver cell types in monkeys (top). Additional UMAP plots depict the cell type distribution across 4 groups (bottom).

(B) Radial bar chart displaying the rescue of multiple monkey liver cell types' biological age (sn-transcriptAge) by metformin, as determined from liver snRNA-seq data. Dot plot depicting sn-transcriptAge from liver snRNA-seq. Box plot illustrating the rescue of monkey sn-transcriptAge by metformin. Only significant (Wilcoxon rank-sum test p values < 0.05) rescue cell types were plotted. The dot symbolizes a metacell in the test set or O-Met group.

(C) UMAP plot showing distribution of different cell types in the brain (FL) (left). UMAP plots showing distribution of different cell types in 4 groups (right).

(D) Dot plot illustrates the integrated predicted biological age (sn-transcriptAge) from frontal lobe snRNA-seq data (left). The boxplot displays the rescue of monkeys' integrated biological age in the frontal lobe by metformin treatment. Each dot represents a metacell from the test set or O-Met group.

(E) Radial bar chart depicts the rescue of monkey frontal lobe multi-cell type biological age (sn-transcriptAge) by metformin, based on frontal lobe snRNA-seq (left). Dot plot (right top) shows sn-transcriptAge derived from frontal lobe snRNA-seq. Boxplot (right bottom) illustrates the rescue of monkeys' sn-transcriptAge by metformin treatment. Significant rescue cell types, as determined by Wilcoxon rank-sum test with $p < 0.05$, are exclusively plotted. Dot plot illustrates the integrated sn-transcriptAge from frontal lobe snRNA-seq data (left). The boxplot displays the rescue of monkeys' integrated biological age in the frontal lobe by metformin treatment. Each dot represents a metacell from the test set or O-Met group.

(F) Networks illustrate the representative GO terms significantly enriched in both up- and down-regulated rescued DEGs across various cell types, as identified through functional enrichment analysis.

(G) Assessments of brain aging in Y-Ctrl, M-Ctrl, O-Ctrl, and O-Met monkeys include SA-β-gal staining, immunofluorescence for p-Tau (T181) and MMP9, and electron microscopy analysis for mean myelin sheath thickness in the frontal lobe (FL). Scale bars of SA-β-gal staining and immunofluorescence analysis of p-Tau (T181) and MMP9 in brain (FL), 20 μm. Scale bars of electron microscopy analysis of mean myelin sheath thickness, 1 μm. Y-Ctrl, $n = 6$; M-Ctrl, $n = 3$; O-Ctrl, $n = 5$; O-Met, $n = 6$ monkeys. The quantified data are shown as means ± SEMs, one-way ANOVA with Tukey's multiple comparisons test p values are indicated.

The dashed line in (B), (D), and (E) indicates no difference between the predicted biological age and the expected measurement for the monkey's actual age (ΔAge = 0), with the gap between the dot and line representing the individual's aging rate.

See also Figures S5, S6, and S7 and Table S4.

Please cite this article in press as: Yang et al., Metformin decelerates aging clock in male monkeys, Cell (2024), https://doi.org/10.1016/j.cell.2024.08.021

CellPress

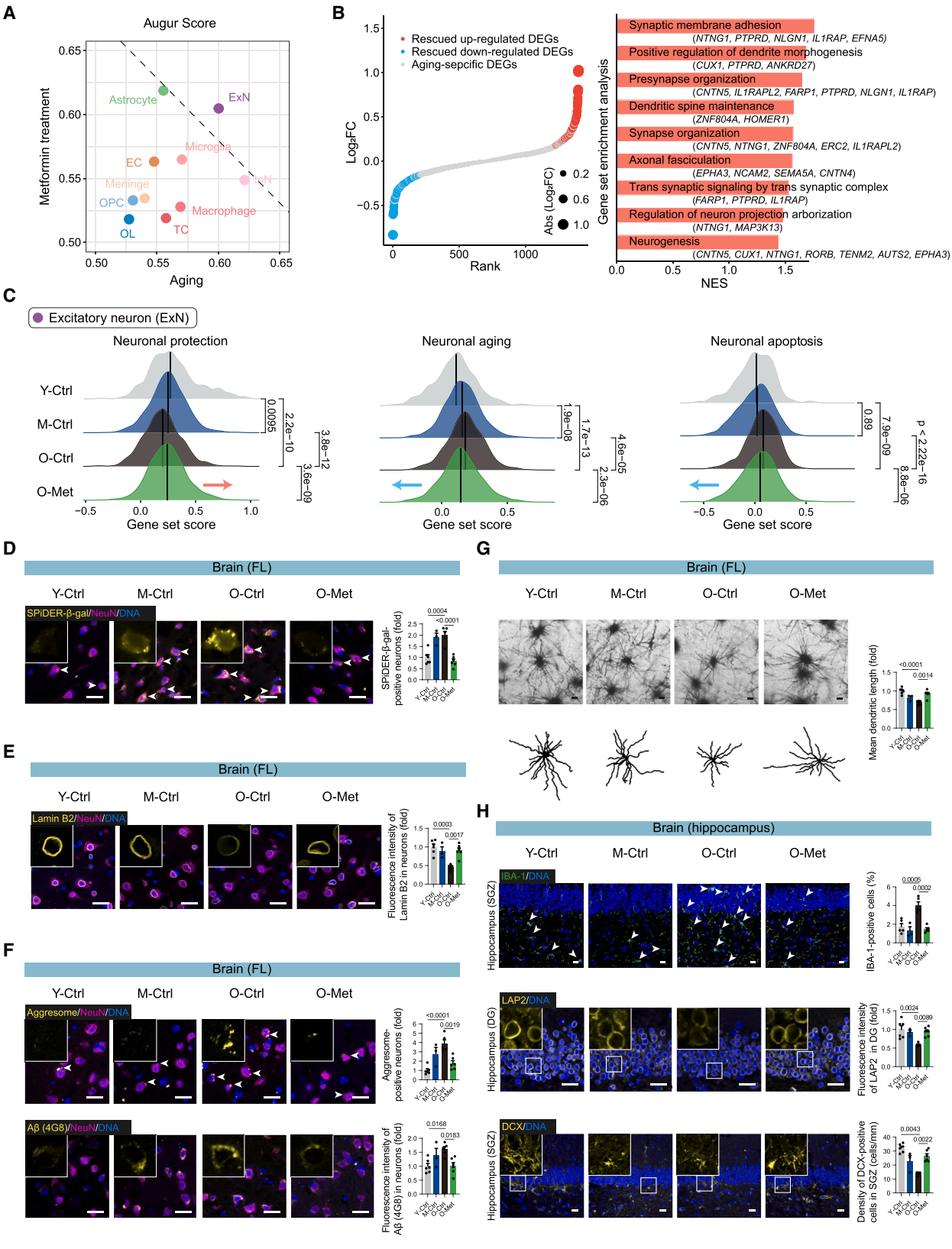

(legend on next page)

Please cite this article in press as: Yang et al., Metformin decelerates aging clock in male monkeys, Cell (2024), https://doi.org/10.1016/j.cell.2024.08.021

protein kinase (AMPK) activation and mitochondrial electron transport inhibition,[77,82–86] our findings underscore the Nrf2 antioxidant pathway as a promising target for geroprotection.[22,87–90]

Significantly, the metformin dosage in our primate study falls within the standard therapeutic range,[12,14,91–94] enhancing the applicability of our findings to human therapeutics. The observed reversal of aging biomarkers in primates indicates the feasibility of targeting core aging mechanisms in organs, offering a strategy to improve chronic conditions and prevent age-related diseases. Our research identifies the optimal dosage and timing for metformin administration in primates, elucidating organ-specific sensitivity and providing pharmacodynamic insights. Additionally, we introduce predictive biomarkers for intervention efficacy assessment, including plasma and tissue clocks from accessible clinical biopsies.[31,95] These innovative biomarkers establish a clinical standard for evaluating geroprotective interventions,[31,96,97] offering a structured approach to assess the effects of pharmaceuticals on aging and to develop strategies for combating age-related chronic diseases.

Limitations of the study

Our study reveals the multifaceted influence of metformin on decelerating primate aging, with a current emphasis on male subjects. We have noted that metformin potentially slows aging at molecular and tissue levels in males, but conclusive evidence of functional rejuvenation is sparse, and a full understanding of its side effects in humans remains elusive. The study also omitted assessments of monkey mortality and the long-term effects following metformin cessation. Recognizing the complex interactions of geroprotective agents with multiple targets is key, indicating that research into pathways beyond Nrf2 holds promise. While the comprehensive impact and mechanisms of metformin in primates are yet to be fully charted, our findings indicate significant delays in the aging process. This insight is a critical step forward, guiding the advancement of clinical strategies to mitigate aging impacts and its associated health issues.

RESOURCE AVAILABILITY

Lead contact

Further information and requests for resources and reagents should be directed to and will be fulfilled by the lead contact, Guang-Hui Liu (ghliu@ioz.ac.cn).

Materials availability

This study did not generate new unique reagents.

Data and code availability

- Bulk RNA-seq data of cynomolgus monkey tissues have been deposited at the Genome Sequence Archive (GSA) in the National Genomics Data Center, Beijing Institute of Genomics (China National Center for Bioinformation) of the Chinese Academy of Sciences. Raw data for previously published bulk RNA-seq for the gingiva can be accessed at CRA014943. snRNA-seq data of cynomolgus monkey tissues have been deposited at the GSA. Bulk RNA-seq data of hNeuron have been deposited at the GSA-Human. DNA methylation and metabolomics data of cynomolgus monkey tissues have been deposited at the Open Archive for Miscellaneous Data (OMIX) in the National Genomics Data Center, Beijing Institute of Genomics (China National Center for Bioinformation) of the Chinese Academy of Sciences. The DIA plasma proteomics data generated in this study have been deposited in the iProX database consortium. Accession numbers are listed in the key resources table.
- This paper does not report original code.
- Any additional information required to reanalyze the data reported in this paper is available from the lead contact upon request.

ACKNOWLEDGMENTS

We extend our heartfelt thanks to the Aging Biomarker Consortium for their insightful feedback and guidance. Our appreciation goes to Hongxing Han, Wei Li, Feifei Liu, Jingyi Jia, Chen Xie, Zhejun Ji, Shanshan Yang, Fangshuo Zheng, Huifang Hu, Yanxia Ye, Xiaoqian Liu, Lingling Geng, Daoyuan Huang, Beibei Liu, Chengyu Liu, Linguo Cai, Xuebao Wang, Min Wang, Yan Yu, Guoqiang Sun, Jian Yin, Lanzhu Li, Cui Wang, Ruochen Wu, Ping Yang, Liyun Zhao, Sheng Zhang, Baohu Zhang, Jinghao Hu, Xiuping Li, Shuaiqi Fang, Yixin Zhang, Zehua Wang, Yingjie Ding, Shijia Bi, Zhiran Zou, Tianling Cao, Di Liu, Xiaoyan Sun, Mingheng Li, Xiangmei Jin, Yandong Zheng, Kang Wang, Yuesheng Zuo, Haoteng Yan, Miyang Ma, Jiale Ping, Zeming Wu, Chen Zhang, and Yixuan Hu for their assistance with tissue dissociation from specific monkey organs. We are grateful to Guibin Wang from the State Key Laboratory of Medical Proteomics, Beijing Proteome Research Center, National Center for Protein Sciences (Beijing), and Beijing Institute of Lifeomics for conducting plasma protein mass spectrometry analysis. We also thank Linguo Cai and Miyang Ma for their expertise in cell culture guidance. We acknowledge Lei Bai, Ruijun Bai, Jing Lu, Qun Chu, Ying Yang, Luyang Tian, Shangyi Qiao, Jing Chen, Xiangmei Jin, Xiuping Li, and Xuewei Chen for their administrative support. Our thanks go to Junying Jia from the Institute of Biophysics, Chinese Academy of Sciences, for the fluorescence-activated cell sorting, to Shiwen Li, Xili Zhu, Yue Wang, and Hua Qin from the Institute of Zoology, Chinese Academy of Sciences, for image scanning, to Junfeng Hao from the Institute of

Figure 6. Metformin demonstrates neuroprotective properties in the frontal lobes of aged monkeys

(A) Dot plot showing cell type prioritization in snRNA-seq by Augur.

(B) Dot plot showing the age-dependent DEG. The order was ranked by $\log_2$(fold change) (O-Met/O-Ctrl) (left). The red, blue, and gray dots represent rescue up-regulated, rescue down-regulated, and non-rescued genes, respectively. A bar plot (right) displays gene set enrichment analysis (GSEA) results post-metformin treatment in excitatory neurons of the monkey frontal lobe.

(C) Ridge plots showing representative gene set score in four groups. The black line represents the median expression. Wilcoxon rank-sum test *p* values are indicated.

(D) SPiDER-β-gal staining evaluation brain (FL) with immunofluorescence examination of NeuN in Y-Ctrl, M-Ctrl, O-Ctrl, and O-Met monkeys. Scale bars, 20 μm.

(E) Immunofluorescence evaluation of Lamin B2 and NeuN in brain (FL) in Y-Ctrl, M-Ctrl, O-Ctrl, and O-Met monkeys. Scale bars, 20 μm.

(F) Aggresome assessment (top) and immunofluorescence examination of Aβ (4G8) (bottom) of brain (FL) with immunofluorescence examination of NeuN in Y-Ctrl, M-Ctrl, O-Ctrl, and O-Met monkeys. Scale bars, 20 μm.

(G) Golgi staining analysis of the frontal lobe (FL) in Y-Ctrl, M-Ctrl, O-Ctrl, and O-Met monkeys. Scale bars, 20 μm.

(H) Immunofluorescent analysis of IBA-1, DCX, and LAP2 in brain (hippocampus) of Y-Ctrl, M-Ctrl, O-Ctrl, and O-Met monkeys. Scale bars, 20 μm.

The quantified data in (D)–(H) are shown as means ± SEMs, one-way ANOVA with Tukey's multiple comparisons test *p* values of (D)–(G), IBA-1 and LAP2 in (H) are indicated, Mann-Whitney test *p* values of DCX in (H) are indicated. Y-Ctrl, n = 5–6; M-Ctrl, n = 3; O-Ctrl, n = 5; O-Met, n = 5–6 monkeys in (D)–(H).

See also Figure S7 and Table S4.

Please cite this article in press as: Yang et al., Metformin decelerates aging clock in male monkeys, Cell (2024), https://doi.org/10.1016/j.cell.2024.08.021

CellPress

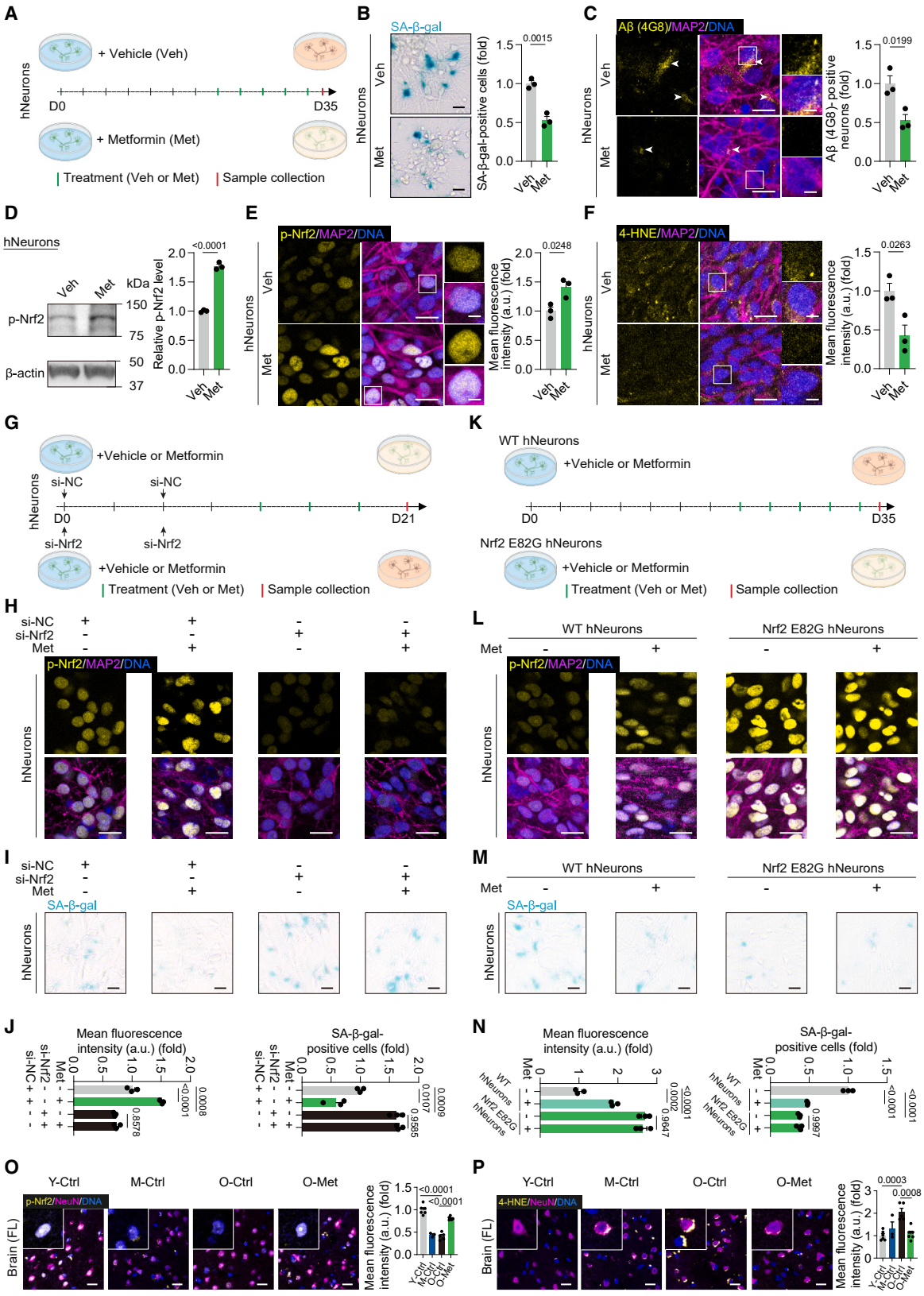

(legend on next page)

Biophysics, Chinese Academy of Sciences, for additional slide scanning, and to Can Peng from the Institute of Biophysics, Chinese Academy of Sciences, for her work on TEM. We acknowledge Lingling Geng for assisting in animal experiments and Liang Sun for valuable advice. This work was supported by the National Key Research and Development Program of China (2022YFA1103700, 2022YFA1103800)), the National Natural Science Foundation of China (82125011, 92168201, 81921006, 92149301, 82122024, 82322025, and 82361148131), the Program of the Beijing Natural Science Foundation (JQ24044), the National Key Research and Development Program of China (2020YFA0804000, the STI2030-Major Projects-2021ZD0202400, 2023YFC3605400, 2020YFA0112200, 2021YFF1201000, 2023YFC3504301, 2020YFA0113400, 2021YFA1101000, 2021ZD0200200, and 2022YFC3602000), the National Natural Science Foundation of China (82330044, 32341001, 92049304, 92049116, 32121001, 82192863, 82271600, 82071588, 82361148130, 8231101626, 82201727, 82230060, 81788101, 32141004, 82203021, and 82171799), CAS Project for Young Scientists in Basic Research (YSBR-076, YSBR-012, and YSBR-036), the Program of the Beijing Natural Science Foundation (Z230011, Z240018, 5244046, and 5242024), the Informatization Plan of Chinese Academy of Sciences (CAS-WX2022SDC-XK14), New Cornerstone Science Foundation through the XPLORER PRIZE (2021-1045), Youth Innovation Promotion Association of CAS (E1CAZW0401, 2020085, 2022083, and 2023092), Young Elite Scientists Sponsorship Program by CAST (2021QNRC001), Initiative Scientific Research Program, Institute of Zoology, CAS (2023IOZ0102), Postdoctoral Fellowship Program of CPSF (GZC20232647), Beijing Hospitals Authority Youth Programme (QML20230806), Excellent Young Talents Program of Capital Medical University (12300927), the Project for Technology Development of Beijing-Affiliated Medical Research Institutes (11000023T000002036310), Excellent Young Talents Training Program for the Construction of Beijing Municipal University Teacher Team (BPHR202203105), Beijing Municipal Public Welfare Development and Reform Pilot Project for Medical Research Institutes (JYY2023-13), and CAS Youth Interdisciplinary Team. We thank the support from the Proteomic Navigator of the Human Body (π-HuB) Project.

AUTHOR CONTRIBUTIONS

G.-H.L., W.Z., and J.Q. provided the conceptual framework for this project and oversaw the execution of the experiments in their entirety. Y.Y. conducted animal experiments and carried out the single-nuclear isolation of the monkey's frontal lobe and liver. N.L., Y.Q., and X.D. performed the MRI experiment and data analysis of the monkey's brain. N.L., Z. Zhang, and F.X. executed the Wisconsin general test apparatus experiments on monkeys. Z. Zheng and P.R. performed the aging clock construction. X.L., A.H., and S.H. performed bioinformatics analysis of the aging clock and single-nucleus RNA sequencing (snRNA-seq) data. K.Y., S.M., and X.J. performed bioinformatics analysis of bulk RNA-seq, proteomic, and metabolomic data. Y.Y., H.Z., and M.J. performed the cell culture. Y.Y., H.Z., Y.H., and Y.Z. performed immunostaining and tissue section analyses. Y.Y. performed the TEM analysis. Q.H. conducted the micro-CT analysis. Y.Y., M. Xiong, L.L., and Q.Z. performed the DNA isolation of monkey tissues. Q.W. provided assistance in creating the schematic diagrams. J. Lei, S.S., Y. Jing, J. Li, Y.C., Y.F., K.Y., M. Xiong, M. Xing, and Y. Jing performed tissue dissociation from specific monkey organs. G. Zhao, W.S., S.H., C.R.E., M.S., S.W., X.Z., G. Zhu, W.L., and J.C.I.B. helped with supervision of the project. G.-H.L., J.Q., W.Z., Y.Y., X.L., N.L., S.M., H.Z., and Z. Zhang contributed to writing, reviewing, and editing the manuscript.

DECLARATION OF INTERESTS

J.C.I.B., S.H., C.R.E., P.R., and A.H. are employees of Altos Labs. S.H. is a founder of the non-profit Epigenetic Clock Development Foundation, which has licensed several of his patents from UC Regents and distributes the mammalian methylation array.

STAR★METHODS

Detailed methods are provided in the online version of this paper and include the following:

- KEY RESOURCES TABLE
- EXPERIMENTAL MODEL AND STUDY PARTICIPANT DETAILS
  - Ethical statement
  - Experimental cynomolgus monkey
- METHOD DETAILS
  - Routine physical examination
  - Structural MRI
  - Cognitive testing
  - Micro-CT analysis
  - Tissue dissociation
  - RNA-seq Library construction and sequencing
  - Protein extraction and trypsin digestion

Figure 7. Metformin postpones neuronal senescence in a manner dependent on Nrf2

(A) Illustration of metformin's geroprotective effects on cultured hNeurons *in vitro*, detailing the treatment regimens applied. Veh, vehicle; Met, metformin.
(B) Assessment of SA-β-gal staining in hNeurons on day 35 after treatment with Veh or Met. Scale bars, 20 μm.
(C) Immunofluorescence analysis of Aβ (4G8) in MAP2-marked hNeurons on day 35 after treatment with Veh or Met. The arrows indicate Aβ (4G8)-positive neurons. Scale bars, 20 and 5 μm (zoomed-in images).
(D) Western blot analysis of p-Nrf2 levels in hNeurons on day 35 after treatment with Veh or Met.
(E) Immunofluorescence examination of p-Nrf2 in MAP2-marked hNeurons on day 35 after treatment with Veh or Met. Scale bars, 20 and 5 μm (zoomed-in images).
(F) Immunofluorescence analysis of 4-HNE in MAP2-marked hNeurons on day 35 after treatment with Veh or Met. Scale bars, 20 and 5 μm (zoomed-in images).
(G) Schematic representation of metformin treatment in extended culture of si-NC or si-Nrf2 hNeurons, with treatment protocols as indicated.
(H) Immunofluorescent analysis of p-Nrf2 in MAP2-positive si-NC or si-Nrf2 hNeurons on day 21 after treatment with Veh or Met. Scale bars, 20 μm.
(I) SA-β-gal staining assessment in si-NC or si-Nrf2 hNeurons on day 21 after treatment with Veh or Met. Scale bars, 20 μm.
(J) Quantitative analysis of mean fluorescence intensity for p-Nrf2 and the proportion of SA-β-gal-positive cells in si-NC or si-Nrf2 hNeurons on day 21 after treatment with Veh or Met.
(K) Schematic overview of metformin treatment in extended cultures of wildtype (WT) or Nrf2 E82G hNeurons, with treatment protocols as indicated.
(L) Immunofluorescence examination of p-Nrf2 in MAP2-marked WT or Nrf2 E82G hNeurons on day 35 after treatment with Veh or Met. Scale bars, 20 μm.
(M) SA-β-gal staining evaluation in WT or Nrf2 E82G hNeurons on day 35 following treatment with Veh or Met. Scale bars, 20 μm.
(N) Quantitative assessment of mean fluorescence intensity of p-Nrf2 and the prevalence of SA-β-gal-positive cells in WT or Nrf2 E82G hNeurons on day 35 post-treatment with Veh or Met.
(O) Immunofluorescence examination of p-Nrf2 and NeuN in brain (FL) of Y-Ctrl, M-Ctrl, O-Ctrl, and O-Met monkeys. Scale bars, 20 μm.
(P) Immunofluorescence analysis of 4-HNE and NeuN in brain (FL) of Y-Ctrl, M-Ctrl, O-Ctrl, and O-Met monkeys. Scale bars, 20 μm.
The quantified data in (B)–(F), (J), and (N)–(P) are shown as means ± SEMs, two-tailed Student's t test *p* values are indicated in (B)–(F), one-way ANOVA with Tukey's multiple comparisons test *p* values are indicated in (J) and (N)–(P). $n = 3$ biological samples per group in (B)–(F), (J), and (N). Y-Ctrl, $n = 6$; M-Ctrl, $n = 3$; O-Ctrl, $n = 5$; O-Met, $n = 6$ monkeys in (O) and (P).
See also Figures S8 and S9.

- Mass spectrometry analysis of plasma proteins
- Mass spectrometry analysis of plasma metabolites
- DNA preparation
- Microarray experiment of DNA methylation
- Nuclei sorting and snRNA-seq on the 10x genomics chromium platform
- SA-β-gal staining
- Hematoxylin and eosin (HE) staining
- Masson's trichrome staining
- Aggresome staining
- ROS analysis
- Immunohistochemistry staining
- Transmission electron microscopy (TEM) analysis of myelin thickness
- Golgi staining
- Oil red O staining
- Immunofluorescence staining
- Human embryonic stem cell (hESC) culture
- Human neuron (hNeuron) differentiation
- Knockdown of Nrf2 utilizing small interfering RNA (siRNA)
- Metformin treatment of hNeurons
- Western blot analysis
- RNA extraction
- Real-time quantitative PCR
- Bulk RNA-seq data processing
- Gene set variation analysis (GSVA)
- Data-independent acquisition (DIA) quantitative proteomics
- Metabolomic data analysis
- DNA methylation aging clock analysis
- Multi-Model aging clock analysis
- snRNA-seq data processing
- Clustering and identification of cell types for each tissue
- Differential expression analysis from snRNA-seq data
- snRNA-seq tissue-specific aging clock analysis
- Aging-related trajectory analysis
- Rescue differential expression analysis
- Cell type prioritization analysis
- Functional enrichment analysis
- Gene set score analysis

- QUANTIFICATION AND STATISTICAL ANALYSIS

SUPPLEMENTAL INFORMATION

Supplemental information can be found online at https://doi.org/10.1016/j.cell.2024.08.021.

Received: April 15, 2024
Revised: July 10, 2024
Accepted: August 12, 2024
Published: September 12, 2024

REFERENCES

1. Guo, J., Huang, X., Dou, L., Yan, M., Shen, T., Tang, W., and Li, J. (2022). Aging and aging-related diseases: from molecular mechanisms to interventions and treatments. Signal Transduct. Target. Ther. *7*, 391. https://doi.org/10.1038/s41392-022-01251-0.

2. Singh, P.P., Demmitt, B.A., Nath, R.D., and Brunet, A. (2019). The Genetics of Aging: A Vertebrate Perspective. Cell *177*, 200–220. https://doi.org/10.1016/j.cell.2019.02.038.

3. Aging; Biomarker Consortium, Bao, H., Cao, J., Chen, M., Chen, M., Chen, W., Chen, X., Chen, Y., Chen, Y., Chen, Y., et al. (2023). Biomarkers of aging. Sci. China Life Sci. *66*, 893–1066. https://doi.org/10.1007/s11427-023-2305-0.

4. Cai, Y., Song, W., Li, J., Jing, Y., Liang, C., Zhang, L., Zhang, X., Zhang, W., Liu, B., An, Y., et al. (2022). The landscape of aging. Sci. China Life Sci. *65*, 2354–2454. https://doi.org/10.1007/s11427-022-2161-3.

5. Jia, Y.-J., Wang, J., Ren, J.-R., Chan, P., Chen, S., Chen, X.-C., Chhetri, J.K., Guo, J., Guo, Q., Jin, L., et al. (2023). A framework of biomarkers for brain aging: a consensus statement by the Aging Biomarker Consortium. Life Med. *2*, lnad017. https://doi.org/10.1093/lifemedi/lnad017.

6. Partridge, L., Fuentealba, M., and Kennedy, B.K. (2020). The quest to slow ageing through drug discovery. Nat. Rev. Drug Discov. *19*, 513–532. https://doi.org/10.1038/s41573-020-0067-7.

7. Sun, S., Ma, S., Cai, Y., Wang, S., Ren, J., Yang, Y., Ping, J., Wang, X., Zhang, Y., Yan, H., et al. (2023). A single-cell transcriptomic atlas of exercise-induced anti-inflammatory and geroprotective effects across the body. Innovation (Cambridge (Mass.)) *4*, 100380. https://doi.org/10.1016/j.xinn.2023.100380.

8. Wang, W., Zheng, Y., Sun, S., Li, W., Song, M., Ji, Q., Wu, Z., Liu, Z., Fan, Y., Liu, F., et al. (2021). A genome-wide CRISPR-based screen identifies KAT7 as a driver of cellular senescence. Sci. Transl. Med. *13*, eabd2655. https://doi.org/10.1126/scitranslmed.abd2655.

9. Ma, S., Sun, S., Geng, L., Song, M., Wang, W., Ye, Y., Ji, Q., Zou, Z., Wang, S., He, X., et al. (2020). Caloric Restriction Reprograms the Single-Cell Transcriptional Landscape of Rattus Norvegicus Aging. Cell *180*, 984–1001.e22. https://doi.org/10.1016/j.cell.2020.02.008.

10. Zhang, B., Yan, H., Liu, X., Sun, L., Ma, S., Wang, S., Qu, J., Liu, G.-H., and Zhang, W. (2023). SenoIndex: S100A8/S100A9 as a novel aging biomarker. Life Med. *2*. https://doi.org/10.1093/lifemedi/lnad022.

11. Shen, J., Liu, G.-H., and Song, M. (2022). Potential approaches for intervening aging. N.Atl. Sci. Open *1*, 20220021. https://doi.org/10.1360/nso/20220021.

12. Martin-Montalvo, A., Mercken, E.M., Mitchell, S.J., Palacios, H.H., Mote, P.L., Scheibye-Knudsen, M., Gomes, A.P., Ward, T.M., Minor, R.K., Blouin, M.J., et al. (2013). Metformin improves healthspan and lifespan in mice. Nat. Commun. *4*, 2192. https://doi.org/10.1038/ncomms3192.

13. Cabreiro, F., Au, C., Leung, K.Y., Vergara-Irigaray, N., Cochemé, H.M., Noori, T., Weinkove, D., Schuster, E., Greene, N.D.E., and Gems, D. (2013). Metformin retards aging in C. elegans by altering microbial folate and methionine metabolism. Cell *153*, 228–239. https://doi.org/10.1016/j.cell.2013.02.035.

14. Neumann, B., Baror, R., Zhao, C., Segel, M., Dietmann, S., Rawji, K.S., Foerster, S., McClain, C.R., Chalut, K., van Wijngaarden, P., and Franklin, R.J.M. (2019). Metformin Restores CNS Remyelination Capacity by Rejuvenating Aged Stem Cells. Cell Stem Cell *25*, 473–485.e8. https://doi.org/10.1016/j.stem.2019.08.015.

15. Kodali, M., Attaluri, S., Madhu, L.N., Shuai, B., Upadhya, R., Gonzalez, J.J., Rao, X., and Shetty, A.K. (2021). Metformin treatment in late middle age improves cognitive function with alleviation of microglial activation and enhancement of autophagy in the hippocampus. Aging Cell *20*, e13277. https://doi.org/10.1111/acel.13277.

16. Landry, D.A., Yakubovich, E., Cook, D.P., Fasih, S., Upham, J., and Vanderhyden, B.C. (2022). Metformin prevents age-associated ovarian fibrosis by modulating the immune landscape in female mice. Sci. Adv. *8*, eabq1475. https://doi.org/10.1126/sciadv.abq1475.

17. Barzilai, N., Crandall, J.P., Kritchevsky, S.B., and Espeland, M.A. (2016). Metformin as a Tool to Target Aging. Cell Metab. *23*, 1060–1065. https://doi.org/10.1016/j.cmet.2016.05.011.

18. Slack, C., Foley, A., and Partridge, L. (2012). Activation of AMPK by the putative dietary restriction mimetic metformin is insufficient to extend lifespan in Drosophila. PLoS One *7*, e47699. https://doi.org/10.1371/journal.pone.0047699.

19. Chen, S.C., Brooks, R., Houskeeper, J., Bremner, S.K., Dunlop, J., Viollet, B., Logan, P.J., Salt, I.P., Ahmed, S.F., and Yarwood, S.J. (2017). Metformin suppresses adipogenesis through both AMP-activated protein kinase (AMPK)-dependent and AMPK-independent mechanisms.

Mol. Cell. Endocrinol. *440*, 57–68. https://doi.org/10.1016/j.mce.2016.11.011.

20. Bailey, C.J. (2017). Metformin: historical overview. Diabetologia *60*, 1566–1576. https://doi.org/10.1007/s00125-017-4318-z.
21. Geng, L., Zhang, B., Liu, H., Wang, S., Cai, Y., Yang, K., Zou, Z., Jiang, X., Liu, Z., Li, W., et al. (2023). A comparative study of metformin and nicotinamide riboside in alleviating tissue aging in rats. Life Med. *2*, lnac045. https://doi.org/10.1093/lifemedi/lnac045.
22. Fang, J., Yang, J., Wu, X., Zhang, G., Li, T., Wang, X., Zhang, H., Wang, C.C., Liu, G.H., and Wang, L. (2018). Metformin alleviates human cellular aging by upregulating the endoplasmic reticulum glutathione peroxidase 7. Aging Cell *17*, e12765. https://doi.org/10.1111/acel.12765.
23. Li, Q., Hagberg, C.E., Silva Cascales, H., Lang, S., Hyvönen, M.T., Salehzadeh, F., Chen, P., Alexandersson, I., Terezaki, E., Harms, M.J., et al. (2021). Obesity and hyperinsulinemia drive adipocytes to activate a cell cycle program and senesce. Nat. Med. *27*, 1941–1953. https://doi.org/10.1038/s41591-021-01501-8.
24. Bharath, L.P., Agrawal, M., McCambridge, G., Nicholas, D.A., Hasturk, H., Liu, J., Jiang, K., Liu, R., Guo, Z., Deeney, J., et al. (2020). Metformin Enhances Autophagy and Normalizes Mitochondrial Function to Alleviate Aging-Associated Inflammation. Cell Metab. *32*, 44–55.e6. https://doi.org/10.1016/j.cmet.2020.04.015.
25. Noren Hooten, N., Martin-Montalvo, A., Dluzen, D.F., Zhang, Y., Bernier, M., Zonderman, A.B., Becker, K.G., Gorospe, M., de Cabo, R., and Evans, M.K. (2016). Metformin-mediated increase in DICER1 regulates microRNA expression and cellular senescence. Aging Cell *15*, 572–581. https://doi.org/10.1111/acel.12469.
26. Bannister, C.A., Holden, S.E., Jenkins-Jones, S., Morgan, C.L., Halcox, J.P., Schernthaner, G., Mukherjee, J., and Currie, C.J. (2014). Can people with type 2 diabetes live longer than those without? A comparison of mortality in people initiated with metformin or sulphonylurea monotherapy and matched, non-diabetic controls. Diabetes Obes. Metab. *16*, 1165–1173. https://doi.org/10.1111/dom.12354.
27. Campbell, J.M., Bellman, S.M., Stephenson, M.D., and Lisy, K. (2017). Metformin reduces all-cause mortality and diseases of ageing independent of its effect on diabetes control: A systematic review and meta-analysis. Ageing Res. Rev. *40*, 31–44. https://doi.org/10.1016/j.arr.2017.08.003.
28. Campisi, J., Kapahi, P., Lithgow, G.J., Melov, S., Newman, J.C., and Verdin, E. (2019). From discoveries in ageing research to therapeutics for healthy ageing. Nature *571*, 183–192. https://doi.org/10.1038/s41586-019-1365-2.
29. Aging Atlas Consortium (2021). Aging Atlas: a multi-omics database for aging biology. Nucleic Acids Res. *49*, D825–D830. https://doi.org/10.1093/nar/gkaa894.
30. Lu, A.T., Fei, Z., Haghani, A., Robeck, T.R., Zoller, J.A., Li, C.Z., Lowe, R., Yan, Q., Zhang, J., Vu, H., et al. (2023). Universal DNA methylation age across mammalian tissues. Nat Aging *3*, 1144–1166. https://doi.org/10.1038/s43587-023-00462-6.
31. Li, J., Xiong, M., Fu, X.H., Fan, Y., Dong, C., Sun, X., Zheng, F., Wang, S.W., Liu, L., Xu, M., et al. (2023). Determining a multimodal aging clock in a cohort of Chinese women. Med. *4*, 825–848.e13. https://doi.org/10.1016/j.medj.2023.06.010.
32. Rutledge, J., Oh, H., and Wyss-Coray, T. (2022). Measuring biological age using omics data. Nat. Rev. Genet. *23*, 715–727. https://doi.org/10.1038/s41576-022-00511-7.
33. Robinson, O., Chadeau Hyam, M., Karaman, I., Climaco Pinto, R., Ala-Korpela, M., Handakas, E., Fiorito, G., Gao, H., Heard, A., Jarvelin, M.R., et al. (2020). Determinants of accelerated metabolomic and epigenetic aging in a UK cohort. Aging Cell *19*, e13149. https://doi.org/10.1111/acel.13149.
34. Lehallier, B., Gate, D., Schaum, N., Nanasi, T., Lee, S.E., Yousef, H., Moran Losada, P., Berdnik, D., Keller, A., Verghese, J., et al. (2019). Undulating changes in human plasma proteome profiles across the lifespan. Nat. Med. *25*, 1843–1850. https://doi.org/10.1038/s41591-019-0673-2.
35. Zhu, H., Chen, J., Liu, K., Gao, L., Wu, H., Ma, L., Zhou, J., Liu, Z., and Han, J.J. (2023). Human PBMC scRNA-seq-based aging clocks reveal ribosome to inflammation balance as a single-cell aging hallmark and super longevity. Sci. Adv. *9*, eabq7599. https://doi.org/10.1126/sciadv.abq7599.
36. Bulteau, R., and Francesconi, M. (2022). Real age prediction from the transcriptome with RAPToR. Nat. Methods *19*, 969–975. https://doi.org/10.1038/s41592-022-01540-0.
37. Zou, X., Dai, X., Mentis, A.F.A., Esteban, M.A., Liu, L., and Han, L. (2022). From monkey single-cell atlases into a broader biomedical perspective. Life Med. *1*, 254–257. https://doi.org/10.1093/lifemedi/lnac028.
38. Foretz, M., Guigas, B., and Viollet, B. (2023). Metformin: update on mechanisms of action and repurposing potential. Nat. Rev. Endocrinol. *19*, 460–476. https://doi.org/10.1038/s41574-023-00833-4.
39. Matthews, D.R., Paldánius, P.M., Proot, P., Chiang, Y., Stumvoll, M., and Del Prato, S.; VERIFY study group (2019). Glycaemic durability of an early combination therapy with vildagliptin and metformin versus sequential metformin monotherapy in newly diagnosed type 2 diabetes (VERIFY): a 5-year, multicentre, randomised, double-blind trial. Lancet *394*, 1519–1529. https://doi.org/10.1016/S0140-6736(19)32131-2.
40. Liu, Z., Li, X., Zhang, J.T., Cai, Y.J., Cheng, T.L., Cheng, C., Wang, Y., Zhang, C.C., Nie, Y.H., Chen, Z.F., et al. (2016). Autism-like behaviours and germline transmission in transgenic monkeys overexpressing MeCP2. Nature *530*, 98–102. https://doi.org/10.1038/nature16533.
41. Upright, N.A., and Baxter, M.G. (2020). Effect of chemogenetic actuator drugs on prefrontal cortex-dependent working memory in nonhuman primates. Neuropsychopharmacology *45*, 1793–1798. https://doi.org/10.1038/s41386-020-0660-9.
42. Jung, B., Taylor, P.A., Seidlitz, J., Sponheim, C., Perkins, P., Ungerleider, L.G., Glen, D., and Messinger, A. (2021). A comprehensive macaque fMRI pipeline and hierarchical atlas. Neuroimage *235*, 117997. https://doi.org/10.1016/j.neuroimage.2021.117997.
43. Izquierdo, A., Brigman, J.L., Radke, A.K., Rudebeck, P.H., and Holmes, A. (2017). The neural basis of reversal learning: An updated perspective. Neuroscience *345*, 12–26. https://doi.org/10.1016/j.neuroscience.2016.03.021.
44. Miller, E.K., and Cohen, J.D. (2001). An integrative theory of prefrontal cortex function. Annu. Rev. Neurosci. *24*, 167–202. https://doi.org/10.1146/annurev.neuro.24.1.167.
45. Li, X., Li, C., Zhang, W., Wang, Y., Qian, P., and Huang, H. (2023). Inflammation and aging: signaling pathways and intervention therapies. Signal Transduct. Target. Ther. *8*, 239. https://doi.org/10.1038/s41392-023-01502-8.
46. Ma, S., Wang, S., Ye, Y., Ren, J., Chen, R., Li, W., Li, J., Zhao, L., Zhao, Q., Sun, G., et al. (2022). Heterochronic parabiosis induces stem cell revitalization and systemic rejuvenation across aged tissues. Cell Stem Cell *29*, 990–1005.e10. https://doi.org/10.1016/j.stem.2022.04.017.
47. Han, J.J. (2024). The ticking of aging clocks. Trends Endocrinol. Metab. *35*, 11–22. https://doi.org/10.1016/j.tem.2023.09.007.
48. Buckley, M.T., Sun, E.D., George, B.M., Liu, L., Schaum, N., Xu, L., Reyes, J.M., Goodell, M.A., Weissman, I.L., Wyss-Coray, T., et al. (2023). Cell-type-specific aging clocks to quantify aging and rejuvenation in neurogenic regions of the brain. Nat Aging *3*, 121–137. https://doi.org/10.1038/s43587-022-00335-4.
49. Yasui, Y., Kudo, A., Kurosaki, M., Matsuda, S., Muraoka, M., Tamaki, N., Suzuki, S., Hosokawa, T., Ueda, K., Matsunaga, K., et al. (2014). Reduced organic anion transporter expression is a risk factor for hepatocellular carcinoma in chronic hepatitis C patients: a propensity score matching study. Oncology *86*, 53–62. https://doi.org/10.1159/000356643.

50. Shen, H., Lai, Y., and Rodrigues, A.D. (2017). Organic Anion Transporter 2: An Enigmatic Human Solute Carrier. Drug Metab. Dispos. *45*, 228–236. https://doi.org/10.1124/dmd.116.072264.

51. Sanfeliu-Redondo, D., Gibert-Ramos, A., and Gracia-Sancho, J. (2024). Cell senescence in liver diseases: pathological mechanism and theranostic opportunity. Nat. Rev. Gastroenterol. Hepatol. *21*, 477–492. https://doi.org/10.1038/s41575-024-00913-4.

52. Ogrodnik, M., Miwa, S., Tchkonia, T., Tiniakos, D., Wilson, C.L., Lahat, A., Day, C.P., Burt, A., Palmer, A., Anstee, Q.M., et al. (2017). Cellular senescence drives age-dependent hepatic steatosis. Nat. Commun. *8*, 15691. https://doi.org/10.1038/ncomms15691.

53. Wijayasiri, P., Astbury, S., Kaye, P., Oakley, F., Alexander, G.J., Kendall, T.J., and Aravinthan, A.D. (2022). Role of Hepatocyte Senescence in the Activation of Hepatic Stellate Cells and Liver Fibrosis Progression. Cells *11*, 2221. https://doi.org/10.3390/cells11142221.

54. Yu, H., Jiang, X., Dong, F., Zhang, F., Ji, X., Xue, M., Yang, F., Chen, J., Hu, X., and Bao, Z. (2021). Lipid accumulation-induced hepatocyte senescence regulates the activation of hepatic stellate cells through the Nrf2-antioxidant response element pathway. Exp. Cell Res. *405*, 112689. https://doi.org/10.1016/j.yexcr.2021.112689.

55. Jurk, D., Wilson, C., Passos, J.F., Oakley, F., Correia-Melo, C., Greaves, L., Saretzki, G., Fox, C., Lawless, C., Anderson, R., et al. (2014). Chronic inflammation induces telomere dysfunction and accelerates ageing in mice. Nat. Commun. *2*, 4172. https://doi.org/10.1038/ncomms5172.

56. Zhao, H., Ji, Q., Wu, Z., Wang, S., Ren, J., Yan, K., Wang, Z., Hu, J., Chu, Q., Hu, H., et al. (2022). Destabilizing heterochromatin by APOE mediates senescence. Nat Aging *2*, 303–316. https://doi.org/10.1038/s43587-022-00186-z.

57. Lu, H., Jing, Y., Zhang, C., Ma, S., Zhang, W., Huang, D., Zhang, B., Zuo, Y., Qin, Y., Liu, G.H., et al. (2024). Aging hallmarks of the primate ovary revealed by spatiotemporal transcriptomics. Protein Cell *15*, 364–384. https://doi.org/10.1093/procel/pwad063.

58. Zhang, H., Li, J., Yu, Y., Ren, J., Liu, Q., Bao, Z., Sun, S., Liu, X., Ma, S., Liu, Z., et al. (2023). Nuclear lamina erosion-induced resurrection of endogenous retroviruses underlies neuronal aging. Cell Rep. *42*, 112593. https://doi.org/10.1016/j.celrep.2023.112593.

59. Sun, S., Li, J., Wang, S., Li, J., Ren, J., Bao, Z., Sun, L., Ma, X., Zheng, F., Ma, S., et al. (2023). CHIT1-positive microglia drive motor neuron ageing in the primate spinal cord. Nature *624*, 611–620. https://doi.org/10.1038/s41586-023-06783-1.

60. Itoh, K., Tong, K.I., and Yamamoto, M. (2004). Molecular mechanism activating Nrf2-Keap1 pathway in regulation of adaptive response to electrophiles. Free Radic. Biol. Med. *36*, 1208–1213. https://doi.org/10.1016/j.freeradbiomed.2004.02.075.

61. Cai, Y., Ji, Z., Wang, S., Zhang, W., Qu, J., Belmonte, J.C.I., and Liu, G.-H. (2022). Genetic enhancement: an avenue to combat aging-related diseases. Life Med. *1*, 307–318. https://doi.org/10.1093/lifemedi/lnac054.

62. Yang, S., Liu, C., Jiang, M., Liu, X., Geng, L., Zhang, Y., Sun, S., Wang, K., Yin, J., Ma, S., et al. (2024). A single-nucleus transcriptomic atlas of primate liver aging uncovers the pro-senescence role of SREBP2 in hepatocytes. Protein Cell *15*, 98–120. https://doi.org/10.1093/procel/pwad039.

63. Wang, Q., Wang, X., Liu, B., Ma, S., Zhang, F., Sun, S., Jing, Y., Fan, Y., Ding, Y., Xiong, M., et al. (2024). Aging induces region-specific dysregulation of hormone synthesis in the primate adrenal gland. Nat Aging *4*, 396–413. https://doi.org/10.1038/s43587-024-00588-1.

64. Zhang, H., Li, J., Ren, J., Sun, S., Ma, S., Zhang, W., Yu, Y., Cai, Y., Yan, K., Li, W., et al. (2021). Single-nucleus transcriptomic landscape of primate hippocampal aging. Protein Cell *12*, 695–716. https://doi.org/10.1007/s13238-021-00852-9.

65. Hu, Q., Zhang, B., Jing, Y., Ma, S., Hu, L., Li, J., Zheng, Y., Xin, Z., Peng, J., Wang, S., et al. (2024). Single-nucleus transcriptomics uncovers a geroprotective role of YAP in primate gingival aging. Protein Cell *15*, 612–632. https://doi.org/10.1093/procel/pwae017.

66. Cohen, A.A., Ferrucci, L., Fülöp, T., Gravel, D., Hao, N., Kriete, A., Levine, M.E., Lipsitz, L.A., Olde Rikkert, M.G.M., Rutenberg, A., et al. (2022). A complex systems approach to aging biology. Nat Aging *2*, 580–591. https://doi.org/10.1038/s43587-022-00252-6.

67. Rando, T.A., and Wyss-Coray, T. (2021). Asynchronous, contagious and digital aging. Nat Aging *1*, 29–35. https://doi.org/10.1038/s43587-020-00015-1.

68. Ma, S., Chi, X., Cai, Y., Ji, Z., Wang, S., Ren, J., and Liu, G.H. (2023). Decoding Aging Hallmarks at the Single-Cell Level. Annu. Rev. Biomed. Data Sci. *6*, 129–152. https://doi.org/10.1146/annurev-biodatasci-020722-120642.

69. He, X., Memczak, S., Qu, J., Belmonte, J.C.I., and Liu, G.H. (2020). Single-cell omics in ageing: a young and growing field. Nat. Metab. *2*, 293–302. https://doi.org/10.1038/s42255-020-0196-7.

70. Song, Q., Hou, Y., Zhang, Y., Liu, J., Wang, Y., Fu, J., Zhang, C., Cao, M., Cui, Y., Zhang, X., et al. (2022). Integrated multi-omics approach revealed cellular senescence landscape. Nucleic Acids Res. *50*, 10947–10963. https://doi.org/10.1093/nar/gkac885.

71. Mavromatis, L.A., Rosoff, D.B., Bell, A.S., Jung, J., Wagner, J., and Lohoff, F.W. (2023). Multi-omic underpinnings of epigenetic aging and human longevity. Nat. Commun. *14*, 2236. https://doi.org/10.1038/s41467-023-37729-w.

72. Sharma, S., Zhang, Y., Akter, K.A., Nozohouri, S., Archie, S.R., Patel, D., Villalba, H., and Abbruscato, T. (2023). Permeability of Metformin across an In Vitro Blood-Brain Barrier Model during Normoxia and Oxygen-Glucose Deprivation Conditions: Role of Organic Cation Transporters (Octs). Pharmaceutics *15*, 1357. https://doi.org/10.3390/pharmaceutics15051357.

73. Li, N., Zhou, T., and Fei, E. (2022). Actions of Metformin in the Brain: A New Perspective of Metformin Treatments in Related Neurological Disorders. Int. J. Mol. Sci. *23*, 8281. https://doi.org/10.3390/ijms23158281.

74. Isop, L.M., Neculau, A.E., Necula, R.D., Kakucs, C., Moga, M.A., and Dima, L. (2023). Metformin: The Winding Path from Understanding Its Molecular Mechanisms to Proving Therapeutic Benefits in Neurodegenerative Disorders. Pharmaceuticals (Basel) *16*, 1714. https://doi.org/10.3390/ph16121714.

75. Łabuzek, K., Suchy, D., Gabryel, B., Bielecka, A., Liber, S., and Okopień, B. (2010). Quantification of metformin by the HPLC method in brain regions, cerebrospinal fluid and plasma of rats treated with lipopolysaccharide. Pharmacol. Rep. *62*, 956–965. https://doi.org/10.1016/s1734-1140(10)70357-1.

76. Thinnes, A., Westenberger, M., Piechotta, C., Lehto, A., Wirth, F., Lau, H., and Klein, J. (2021). Cholinergic and metabolic effects of metformin in mouse brain. Brain Res. Bull. *170*, 211–217. https://doi.org/10.1016/j.brainresbull.2021.02.018.

77. Ma, T., Tian, X., Zhang, B., Li, M., Wang, Y., Yang, C., Wu, J., Wei, X., Qu, Q., Yu, Y., et al. (2022). Low-dose metformin targets the lysosomal AMPK pathway through PEN2. Nature *603*, 159–165. https://doi.org/10.1038/s41586-022-04431-8.

78. Zhu, X., Shen, J., Feng, S., Huang, C., Wang, H., Huo, F., and Liu, H. (2023). Akkermansia muciniphila, which is enriched in the gut microbiota by metformin, improves cognitive function in aged mice by reducing the proinflammatory cytokine interleukin-6. Microbiome *11*, 120. https://doi.org/10.1186/s40168-023-01567-1.

79. Zhu, X., Shen, J., Feng, S., Huang, C., Liu, Z., Sun, Y.E., and Liu, H. (2020). Metformin improves cognition of aged mice by promoting cerebral angiogenesis and neurogenesis. Aging (Albany, NY) *12*, 17845–17862. https://doi.org/10.18632/aging.103693.

80. Zhang, J., Lin, Y., Dai, X., Fang, W., Wu, X., and Chen, X. (2019). Metformin treatment improves the spatial memory of aged mice in an APOE

genotype-dependent manner. FASEB J. *33*, 7748–7757. https://doi.org/10.1096/fj.201802718R.

81. He, L. (2020). Metformin and Systemic Metabolism. Trends Pharmacol. Sci. *41*, 868–881. https://doi.org/10.1016/j.tips.2020.09.001.
82. Owen, M.R., Doran, E., and Halestrap, A.P. (2000). Evidence that metformin exerts its anti-diabetic effects through inhibition of complex 1 of the mitochondrial respiratory chain. Biochem. J. *348*, 607–614. https://doi.org/10.1042/bj3480607.
83. El-Mir, M.Y., Nogueira, V., Fontaine, E., Avéret, N., Rigoulet, M., and Leverve, X. (2000). Dimethylbiguanide inhibits cell respiration via an indirect effect targeted on the respiratory chain complex I. J. Biol. Chem. *275*, 223–228. https://doi.org/10.1074/jbc.275.1.223.
84. LaMoia, T.E., Butrico, G.M., Kalpage, H.A., Goedeke, L., Hubbard, B.T., Vatner, D.F., Gaspar, R.C., Zhang, X.M., Cline, G.W., Nakahara, K., et al. (2022). Metformin, phenformin, and galegine inhibit complex IV activity and reduce glycerol-derived gluconeogenesis. Proc. Natl. Acad. Sci. USA *119*, e2122287119. https://doi.org/10.1073/pnas.2122287119.
85. Herzig, S., and Shaw, R.J. (2018). AMPK: guardian of metabolism and mitochondrial homeostasis. Nat. Rev. Mol. Cell Biol. *19*, 121–135. https://doi.org/10.1038/nrm.2017.95.
86. Steinberg, G.R., and Carling, D. (2019). AMP-activated protein kinase: the current landscape for drug development. Nat. Rev. Drug Discov. *18*, 527–551. https://doi.org/10.1038/s41573-019-0019-2.
87. Schmidlin, C.J., Dodson, M.B., Madhavan, L., and Zhang, D.D. (2019). Redox regulation by NRF2 in aging and disease. Free Radic. Biol. Med. *134*, 702–707. https://doi.org/10.1016/j.freeradbiomed.2019.01.016.
88. Matsumaru, D., and Motohashi, H. (2021). The KEAP1-NRF2 System in Healthy Aging and Longevity. Antioxidants (Basel) *10*. https://doi.org/10.3390/antiox10121929.
89. George, M., Tharakan, M., Culberson, J., Reddy, A.P., and Reddy, P.H. (2022). Role of Nrf2 in aging, Alzheimer's and other neurodegenerative diseases. Ageing Res. Rev. *82*, 101756. https://doi.org/10.1016/j.arr.2022.101756.
90. Kubben, N., Zhang, W., Wang, L., Voss, T.C., Yang, J., Qu, J., Liu, G.H., and Misteli, T. (2016). Repression of the Antioxidant NRF2 Pathway in Premature Aging. Cell *165*, 1361–1374. https://doi.org/10.1016/j.cell.2016.05.017.
91. Graham, G.G., Punt, J., Arora, M., Day, R.O., Doogue, M.P., Duong, J.K., Furlong, T.J., Greenfield, J.R., Greenup, L.C., Kirkpatrick, C.M., et al. (2011). Clinical pharmacokinetics of metformin. Clin. Pharmacokinet. *50*, 81–98. https://doi.org/10.2165/11534750-000000000-00000.
92. Kajbaf, F., De Broe, M.E., and Lalau, J.D. (2016). Therapeutic Concentrations of Metformin: A Systematic Review. Clin. Pharmacokinet. *55*, 439–459. https://doi.org/10.1007/s40262-015-0323-x.
93. LaMoia, T.E., and Shulman, G.I. (2021). Cellular and Molecular Mechanisms of Metformin Action. Endocr. Rev. *42*, 77–96. https://doi.org/10.1210/endrev/bnaa023.
94. Madiraju, A.K., Erion, D.M., Rahimi, Y., Zhang, X.M., Braddock, D.T., Albright, R.A., Prigaro, B.J., Wood, J.L., Bhanot, S., MacDonald, M.J., et al. (2014). Metformin suppresses gluconeogenesis by inhibiting mitochondrial glycerophosphate dehydrogenase. Nature *510*, 542–546. https://doi.org/10.1038/nature13270.
95. Li, H., Wu, S., Li, J., Xiong, Z., Yang, K., Ye, W., Ren, J., Wang, Q., Xiong, M., Zheng, Z., et al. (2024). HALL: a comprehensive database for human aging and longevity studies. Nucleic Acids Res. *52*, D909–D918. https://doi.org/10.1093/nar/gkad880.
96. Zheng, Z., Li, J., Liu, T., Fan, Y., Zhai, Q.C., Xiong, M., Wang, Q.R., Sun, X., Zheng, Q.W., Che, S., et al. (2024). DNA methylation clocks for estimating biological age in Chinese cohorts. Protein Cell *15*, 575–593. https://doi.org/10.1093/procel/pwae011.
97. Peng, Y., Ding, L., Xiao, Z., Song, M., Lv, J., and Liu, G.H. (2024). Ethical concerns in aging research: perspectives of global frontline researchers. Sci. China Life Sci. https://doi.org/10.1007/s11427-024-2650-y.
98. Schneider, C.A., Rasband, W.S., and Eliceiri, K.W. (2012). NIH Image to ImageJ: 25 years of image analysis. Nat. Methods *9*, 671–675. https://doi.org/10.1038/nmeth.2089.
99. Fleming, S.J., Chaffin, M.D., Arduini, A., Akkad, A.D., Banks, E., Marioni, J.C., Philippakis, A.A., Ellinor, P.T., and Babadi, M. (2023). Unsupervised removal of systematic background noise from droplet-based single-cell experiments using CellBender. Nat. Methods *20*, 1323–1335. https://doi.org/10.1038/s41592-023-01943-7.
100. McGinnis, C.S., Murrow, L.M., and Gartner, Z.J. (2019). DoubletFinder: Doublet Detection in Single-Cell RNA Sequencing Data Using Artificial Nearest Neighbors. Cell Syst. *8*, 329–337.e4. https://doi.org/10.1016/j.cels.2019.03.003.
101. Hao, Y., Hao, S., Andersen-Nissen, E., Mauck, W.M., 3rd, Zheng, S., Butler, A., Lee, M.J., Wilk, A.J., Darby, C., Zager, M., et al. (2021). Integrated analysis of multimodal single-cell data. Cell *184*, 3573–3587.e29. https://doi.org/10.1016/j.cell.2021.04.048.
102. Crowell, H.L., Soneson, C., Germain, P.L., Calini, D., Collin, L., Raposo, C., Malhotra, D., and Robinson, M.D. (2020). muscat detects subpopulation-specific state transitions from multi-sample multi-condition single-cell transcriptomics data. Nat. Commun. *11*, 6077. https://doi.org/10.1038/s41467-020-19894-4.
103. Herrmann, C., Van de Sande, B., Potier, D., and Aerts, S. (2012). i-cisTarget: an integrative genomics method for the prediction of regulatory features and cis-regulatory modules. Nucleic Acids Res. *40*, e114. https://doi.org/10.1093/nar/gks543.
104. Shannon, P., Markiel, A., Ozier, O., Baliga, N.S., Wang, J.T., Ramage, D., Amin, N., Schwikowski, B., and Ideker, T. (2003). Cytoscape: a software environment for integrated models of biomolecular interaction networks. Genome Res. *13*, 2498–2504. https://doi.org/10.1101/gr.1239303.
105. Zhou, Y., Zhou, B., Pache, L., Chang, M., Khodabakhshi, A.H., Tanaseichuk, O., Benner, C., and Chanda, S.K. (2019). Metascape provides a biologist-oriented resource for the analysis of systems-level datasets. Nat. Commun. *10*, 1523. https://doi.org/10.1038/s41467-019-09234-6.
106. Wickham, H. (2016). ggplot2: Elegant Graphics for Data Analysis (Springer-Verlag New York) https://doi.org/10.1007/978-3-319-24277-4.
107. Friedman, J., Hastie, T., and Tibshirani, R. (2010). Regularization Paths for Generalized Linear Models via Coordinate Descent. J. Stat. Softw. *33*, 1–22. https://doi.org/10.18637/jss.v033.i01.
108. Skinnider, M.A., Squair, J.W., Kathe, C., Anderson, M.A., Gautier, M., Matson, K.J.E., Milano, M., Hutson, T.H., Barraud, Q., Phillips, A.A., et al. (2021). Cell type prioritization in single-cell data. Nat. Biotechnol. *39*, 30–34. https://doi.org/10.1038/s41587-020-0605-1.
109. Morabito, S., Reese, F., Rahimzadeh, N., Miyoshi, E., and Swarup, V. (2023). hdWGCNA identifies co-expression networks in high-dimensional transcriptomics data. Cell Rep. Methods *3*, 100498. https://doi.org/10.1016/j.crmeth.2023.100498.
110. Yu, G., Wang, L.G., Han, Y., and He, Q.Y. (2012). clusterProfiler: an R package for comparing biological themes among gene clusters. Omics *16*, 284–287. https://doi.org/10.1089/omi.2011.0118.
111. Dobin, A., Davis, C.A., Schlesinger, F., Drenkow, J., Zaleski, C., Jha, S., Batut, P., Chaisson, M., and Gingeras, T.R. (2013). STAR: ultrafast universal RNA-seq aligner. Bioinformatics *29*, 15–21. https://doi.org/10.1093/bioinformatics/bts635.
112. Pertea, M., Pertea, G.M., Antonescu, C.M., Chang, T.C., Mendell, J.T., and Salzberg, S.L. (2015). StringTie enables improved reconstruction of a transcriptome from RNA-seq reads. Nat. Biotechnol. *33*, 290–295. https://doi.org/10.1038/nbt.3122.
113. Futschik, M.E., and Carlisle, B. (2005). Noise-robust soft clustering of gene expression time-course data. J. Bioinform. Comput. Biol. *3*, 965–988. https://doi.org/10.1142/s0219720005001375.
114. Hänzelmann, S., Castelo, R., and Guinney, J. (2013). GSVA: gene set variation analysis for microarray and RNA-seq data. BMC Bioinformatics *14*, 7. https://doi.org/10.1186/1471-2105-14-7.

115. Ritchie, M.E., Phipson, B., Wu, D., Hu, Y., Law, C.W., Shi, W., and Smyth, G.K. (2015). limma powers differential expression analyses for RNA-sequencing and microarray studies. Nucleic Acids Res. *43*, e47. https://doi.org/10.1093/nar/gkv007.

116. Zhang, X., Smits, A.H., van Tilburg, G.B., Ovaa, H., Huber, W., and Vermeulen, M. (2018). Proteome-wide identification of ubiquitin interactions using UbIA-MS. Nat. Protoc. *13*, 530–550. https://doi.org/10.1038/nprot.2017.147.

117. Zhou, W., Triche, T.J., Jr., Laird, P.W., and Shen, H. (2018). SeSAMe: reducing artifactual detection of DNA methylation by Infinium BeadChips in genomic deletions. Nucleic Acids Res. *46*, e123. https://doi.org/10.1093/nar/gky691.

118. Fischl, B. (2012). FreeSurfer. Neuroimage *62*, 774–781. https://doi.org/10.1016/j.neuroimage.2012.01.021.

119. Cox, R.W. (1996). AFNI: software for analysis and visualization of functional magnetic resonance neuroimages. Comput. Biomed. Res. *29*, 162–173. https://doi.org/10.1006/cbmr.1996.0014.

120. Avants, B.B., Tustison, N., and Song, G. (2009). Advanced Normalization Tools: V1.0. The Insight Journal.

121. Xia, M., Wang, J., and He, Y. (2013). BrainNet Viewer: a network visualization tool for human brain connectomics. PLoS One *8*, e68910. https://doi.org/10.1371/journal.pone.0068910.

122. Xie, L., Xu, F., Liu, S., Ji, Y., Zhou, Q., Wu, Q., Gong, W., Cheng, K., Li, J., Li, L., et al. (2013). Age- and sex-based hematological and biochemical parameters for Macaca fascicularis. PLoS One *8*, e64892. https://doi.org/10.1371/journal.pone.0064892.

123. Choi, K., Chang, J., Lee, M.J., Wang, S., In, K., Galano-Tan, W.C., Jun, S., Cho, K., Hwang, Y.H., Kim, S.J., and Park, W. (2016). Reference values of hematology, biochemistry, and blood type in cynomolgus monkeys from cambodia origin. Lab. Anim. Res. *32*, 46–55. https://doi.org/10.5625/lar.2016.32.1.46.

124. Li, X., Santos, R., Bernal, J.E., Li, D.D., Hargaden, M., and Khan, N.K. (2023). Biology and postnatal development of organ systems of cynomolgus monkeys (Macaca fascicularis). J. Med. Primatol. *52*, 64–78. https://doi.org/10.1111/jmp.12622.

125. de Magalhães, J.P., and Costa, J. (2009). A database of vertebrate longevity records and their relation to other life-history traits. J. Evol. Biol. *22*, 1770–1774. https://doi.org/10.1111/j.1420-9101.2009.01783.x.

126. Langer, P. (2008). Weigl R.: Longevity of Mammals in Captivity: From the Living Collections of the World, Kleine Senckenberg-Reihe 48 (Mamm Biol), p. 214.

127. Smith, S.M., Jenkinson, M., Woolrich, M.W., Beckmann, C.F., Behrens, T.E.J., Johansen-Berg, H., Bannister, P.R., De Luca, M., Drobnjak, I., Flitney, D.E., et al. (2004). Advances in functional and structural MR image analysis and implementation as FSL. Neuroimage *23*, S208–S219. https://doi.org/10.1016/j.neuroimage.2004.07.051.

128. Malone, I.B., Leung, K.K., Clegg, S., Barnes, J., Whitwell, J.L., Ashburner, J., Fox, N.C., and Ridgway, G.R. (2015). Accurate automatic estimation of total intracranial volume: a nuisance variable with less nuisance. Neuroimage *104*, 366–372. https://doi.org/10.1016/j.neuroimage.2014.09.034.

129. Liu, Y., Yang, Q., Du, Z., Liu, J., Zhang, Y., Zhang, W., and Qin, W. (2022). Synthesis of Surface-Functionalized Molybdenum Disulfide Nanomaterials for Efficient Adsorption and Deep Profiling of the Human Plasma Proteome by Data-Independent Acquisition. Anal. Chem. *94*, 14956–14964. https://doi.org/10.1021/acs.analchem.2c02736.

130. Wiśniewski, J.R., Zougman, A., Nagaraj, N., and Mann, M. (2009). Universal sample preparation method for proteome analysis. Nat. Methods *6*, 359–362. https://doi.org/10.1038/nmeth.1322.

131. Arneson, A., Haghani, A., Thompson, M.J., Pellegrini, M., Kwon, S.B., Vu, H., Maciejewski, E., Yao, M., Li, C.Z., Lu, A.T., et al. (2022). A mammalian methylation array for profiling methylation levels at conserved sequences. Nat. Commun. *13*, 783. https://doi.org/10.1038/s41467-022-28355-z.

132. Haghani, A., Li, C.Z., Robeck, T.R., Zhang, J., Lu, A.T., Ablaeva, J., Acosta-Rodríguez, V.A., Adams, D.M., Alagaili, A.N., Almunia, J., et al. (2023). DNA methylation networks underlying mammalian traits. Science *381*, eabq5693. https://doi.org/10.1126/science.abq5693.

133. Huang, D., Zuo, Y., Zhang, C., Sun, G., Jing, Y., Lei, J., Ma, S., Sun, S., Lu, H., Cai, Y., et al. (2023). A single-nucleus transcriptomic atlas of primate testicular aging reveals exhaustion of the spermatogonial stem cell reservoir and loss of Sertoli cell homeostasis. Protein Cell *14*, 888–907. https://doi.org/10.1093/procel/pwac057.

134. Wang, S., Zheng, Y., Li, J., Yu, Y., Zhang, W., Song, M., Liu, Z., Min, Z., Hu, H., Jing, Y., et al. (2020). Single-Cell Transcriptomic Atlas of Primate Ovarian Aging. Cell *180*, 585–600.e19. https://doi.org/10.1016/j.cell.2020.01.009.

135. Kumar, L., and E Futschik, M. (2007). Mfuzz: a software package for soft clustering of microarray data. Bioinformation *2*, 5–7. https://doi.org/10.6026/97320630002005.

136. Horvath, S., Haghani, A., Macoretta, N., Ablaeva, J., Zoller, J.A., Li, C.Z., Zhang, J., Takasugi, M., Zhao, Y., Rydkina, E., et al. (2022). DNA methylation clocks tick in naked mole rats but queens age more slowly than nonbreeders. Nat Aging *2*, 46–59. https://doi.org/10.1038/s43587-021-00152-1.

137. Landi, S.M., and Freiwald, W.A. (2017). Two areas for familiar face recognition in the primate brain. Science *357*, 591–595. https://doi.org/10.1126/science.aan1139.

138. Costa, V.D., Dal Monte, O., Lucas, D.R., Murray, E.A., and Averbeck, B.B. (2016). Amygdala and Ventral Striatum Make Distinct Contributions to Reinforcement Learning. Neuron *92*, 505–517. https://doi.org/10.1016/j.neuron.2016.09.025.

Please cite this article in press as: Yang et al., Metformin decelerates aging clock in male monkeys, Cell (2024), https://doi.org/10.1016/j.cell.2024.08.021

STAR★METHODS

KEY RESOURCES TABLE

REAGENT or RESOURCE	SOURCE	IDENTIFIER
Antibodies		
Mouse monoclonal anti-TNF-α	Abcam	Cat# ab1793; RRID: AB_302615
Mouse monoclonal anti-IL-1β	Santa Cruz	Cat# sc-52012; RRID: AB_629741
Rabbit monoclonal anti-p21	Cell Signaling Technology	Cat# 2947S; RRID: AB_823586
Rabbit monoclonal anti-MRP8	Abcam	Cat# ab92331; RRID: AB_2050283
Goat polyclonal anti-IBA-1	Abcam	Cat# ab5076; RRID: AB_2224402
Rabbit polyclonal anti-CD45	Abcam	Cat# ab10558; RRID: AB_442810
Chicken polyclonal anti-GFAP	Abcam	Cat# ab4674; RRID: AB_304558
Rabbit monoclonal anti-NeuN	Abcam	Cat# ab177487; RRID: AB_2532109
Rabbit polyclonal anti-MMP9	Abcam	Cat# ab38898; RRID: AB_776512
Rabbit polyclonal anti-ERVW-Env	Abcam	Cat# ab179693; RRID: N/A
Rabbit monoclonal anti-Lamin B2	Abcam	Cat# ab151735; RRID: AB_2827514
Rabbit polyclonal anti-H3K9me3	Abcam	Cat# ab8898; RRID: AB_306848
Rabbit monoclonal anti-Tau (phospho T181)	Abcam	Cat# ab254409; RRID: AB_2905609
Rabbit monoclonal anti-β Amyloid 1-42	Abcam	Cat# ab201061; RRID: AB_2722492
Mouse monoclonal anti-MYH1	DSHB	Cat# BF-F3; RRID: AB_2811120
Mouse monoclonal anti-MYH2	DSHB	Cat# SC-71; RRID: AB_2147165
Mouse monoclonal anti-MYH7	DSHB	Cat# BA-D5; RRID: AB_2235587
Rabbit polyclonal anti-DCX	Cell signaling technology	Cat# 4604S; RRID: N/A
Mouse monoclonal anti-LAP2	BD Biosciences	Cat# 611000; RRID: AB_398313
Rabbit polyclonal to anti-4-Hydroxynonenal	Abcam	Cat# ab46545; RRID: AB_722490
Mouse monoclonal anti-IgG (D-1)	Santa Cruz	Cat# sc-515946; RRID: N/A
Rat monoclonal anti-CTIP2	Abcam	Cat# ab18465; RRID: AB_2064130
Rabbit monoclonal anti-APOE	Abcam	Cat# ab183597; RRID: N/A
Rabbit polyclonal anti-Lamin B1	Abcam	Cat# ab16048; RRID: AB_10107828
Rabbit monoclonal anti-Nrf2	Abcam	Cat# ab62352; RRID: AB_944418
Rabbit monoclonal anti-Phospho-Nrf2-S40	Abclonal	Cat# AP1133; RRID: AB_2864001
Rabbit polyclonal anti-Tom20	Santa Cruz	Cat# SC-11415; RRID: AB_2207533
Rabbit polyclonal anti-Phospho-mTOR (Ser2448)	Cell signaling technology	Cat# 2971S RRID: AB_330970
Rabbit monoclonal anti-phospho-AMPKα (Thr172) (40H9)	Cell signaling technology	Cat# 2535S; RRID: AB_2827957
Goat anti-Mouse IgM (Heavy Chain) Secondary Antibody, Alexa Fluor 647	Invitrogen	Cat# A-21238; RRID: AB_2535807
Goat anti-Mouse IgG1 Cross-Adsorbed Secondary Antibody, Alexa Fluor 488	Invitrogen	Cat# A-21121; RRID: AB_2535764
Goat anti-Mouse IgG2b Cross-Adsorbed Secondary Antibody, Alexa Fluor 594	Invitrogen	Cat# A-21145; RRID: AB_2535781
Donkey anti-Mouse IgG (H+L) Highly Cross-Adsorbed Secondary Antibody, Alexa Fluor 568	Invitrogen	Cat# A10037; RRID: AB_2534013
Donkey anti-Mouse IgG (H+L) Highly Cross-Adsorbed Secondary Antibody, Alexa Fluor 488	Invitrogen	Cat# A21202; RRID: AB_141607

(*Continued on next page*)

Please cite this article in press as: Yang et al., Metformin decelerates aging clock in male monkeys, Cell (2024), https://doi.org/10.1016/j.cell.2024.08.021

Continued

REAGENT or RESOURCE	SOURCE	IDENTIFIER
Donkey anti-Rabbit IgG (H+L) Highly Cross-Adsorbed Secondary Antibody, Alexa Fluor 568	Invitrogen	Cat# A10042; RRID: AB_2534017
Donkey anti-Rabbit IgG (H+L) Highly Cross-Adsorbed Secondary Antibody, Alexa Fluor 488	Invitrogen	Cat# A21206; RRID: AB_2535792
Donkey anti-Goat IgG (H+L) Cross-Adsorbed Secondary Antibody, Alexa Fluor 488	Invitrogen	Cat# A11055; RRID: AB_2534102
Goat anti-Chicken IgY (H+L) Secondary Antibody, Alexa Fluor 488	Invitrogen	Cat# A11039; RRID: AB_2534096
Chemicals, peptides, and recombinant proteins		
DMEM with high glucose	Hyclone	Cat# SH30243.01
GlutaMAX	Gibco	Cat# 35050079
Non-essential amino acids (NEAA)	Gibco	Cat# 11140076
Penicillin/streptomycin (P/S)	Gibco	Cat# 15140163
Plasmocin®-Mycoplasma Elimination Reagent	InvivoGene	Cat# ant-mpp
Fetal bovine serum (FBS)	Gibco	Cat# 10270-106; LOT# 42F9083K
Gelatin	Sigma-Aldrich	Cat# V900863
bFGF	Joint Protein Central	Cat# BBI-EXP-002
TRIzol™ Reagent	Thermo Fisher Scientific	Cat# 15596018
4% paraformaldehyde	Dingguo, China	Cat# AR-0211
Triton™ X-100	Sigma-Aldrich	Cat# T9284
iTaq Universal SYBR Green Super Mix	Toyobo	Cat# QPS-201
Hoechst 33342	Invitrogen	Cat# H3570
Sodium citrate buffer	ZSJQ-BIO	Cat# ZLI-9065
DMSO	Sigma	Cat# D2650
Propidium iodide	Invitrogen	Cat# P3566
Protease inhibitor cocktail	Roche	Cat# 4693159001
X-gal	Amresca	Cat# 0428-25G
Metformin hydrochloride	MERCK	N/A
Metformin hydrochloride	Tocris Bioscience	Cat# 2864
Matrigel Matrix	BD Biosciences	Cat# 354230
KnockOut-SR	Thermo Fisher Scientific	Cat# A31815-02
2-Mercaptoethanol	GIBCO	Cat# 21985-023
Advanced DMEM/F12	GIBCO	Cat# 12634-028
Neurobasal	GIBCO	Cat# 12348-017
N2	GIBCO	Cat# 17502-048
B27	GIBCO	Cat# 17504-044
hLIF	Millipore	Cat# LIF1050
SB431542	Selleck	Cat# S1067
CHIR99021	TOCRIS	Cat# 252917-06-9
Dorsomorphin	Sigma-Aldrich	Cat# P5499
Compound E	Millipore	Cat# 565790
dbcAMP	Sigma-Aldrich	Cat# D0627
Ascorbic acid	Sigma-Aldrich	Cat# A8960
BDNF	PEPROTECH	Cat# 450-02
GDNF	PEPROTECH	Cat# 450-02

(*Continued on next page*)

Please cite this article in press as: Yang et al., Metformin decelerates aging clock in male monkeys, Cell (2024), https://doi.org/10.1016/j.cell.2024.08.021

Continued

REAGENT or RESOURCE	SOURCE	IDENTIFIER
StemPro™ Accutase™ Cell Dissociation Reagent	GIBCO	Cat# A1110501
Laminin	Sigma-Aldrich	Cat# L2020
Proteinase K	New England Biolabs	Cat# P8107S
RNasin Plus RNase Inhibitor	Promega	Cat# N2618
SUPERase-IN RNase Inhibitor	Invitrogen	Cat# AM2694
VECTASHIELD Antifade Mounting Medium	Vector Laboratories	Cat# H-1000
Oil red O	Sigma-Aldrich	Cat# O0625
Cellular Senescence Detection Kit-SPiDERGal	DOJINDO Laboratories	Cat# SG03
Wheat Germ Agglutinin (WGA), Alexa Fluor™ 555 Conjugate	Invitrogen	Cat# W32464
RIPA lysis buffer	Beyotime	Cat# P0013B
cOmplete™, Mini, EDTA-free Protease Inhibitor Cocktail	Roche	Cat# 4693159001
PhosSTOP™, Phosphatase Inhibitor Cocktail	Roche	Cat# 4906837001
PMSF	Dingguo, China	Cat# WB-0181
CM-H2DCFDA	Invitrogen	Cat# C6827
5x SDS loading buffer	Dingguo, China	Cat# WB-0091
Critical commercial assays		
TUNEL cell apoptosis detection Kit	Beyotime	Cat# C1088
HiScript IV RT SuperMix for qPCR (+gDNA wiper)	Vazyme	Cat# R423-01
DAB Kit	ZSJQ-BIO	Cat# ZLI-9018
Human IL6 ELISA Kit	BioLegend	Cat# 430515
Lipofectamine 3000 Transfection Reagent	Thermo Fisher Scientific	Cat# L3000015
Proteostat Protein Aggregation Assay	Enzo	Cat# ENZ-51035-K100
Masson's trichrome staining Kit	Solarbio	Cat# G1346
FD Rapid GolgiStain™ Kit	FD NeuroTechnologies	Cat# PK401
Deposited data		
The raw data for bulk RNA-seq and snRNA-seq	This study	GSA: CRA015128, CRA012195 and CRA015001; GSA-Human: HRA007906
The raw data for protemics	This study	IProX: IPX0008294000.
The raw data for metabolomics	This study	OMIX: OMIX005919 and OMIX005920
The raw data for DNA methylation	This study	OMIX: OMIX005896 and OMIX005897
Experimental models: Cell lines		
WT hNeurons (derived from WT hESCs)	Zhang et al.[58]	N/A
Nrf2 E82G hNeurons (derived from Nrf2 E82G hESCs)	This study	N/A
Experimental models: Organisms/Strains		
The cynomolgus monkey tissues	Beijing Institute of Xieerxin Biology Resource, Beijing, China	N/A
Oligonucleotides		
Primers for real-time quantitative PCR, see Table S5	This paper	N/A
siRNAs for RNAi, see Table S5	This paper	N/A
Software and algorithms		
ImageJ (version 1.8.0)	Schneider et al.[98]	https://imagej.net/Welcome

(*Continued on next page*)

Continued

REAGENT or RESOURCE	SOURCE	IDENTIFIER
GraphPadPrism 9.0	GraphPad Software Inc.	https://www.graphpad.com/
Image Lab 4.0.1	Bio-Rad	https://www.bio-rad.com/zh-cn/product/imagelab-software?ID=KRE6P5E8Z
Phenochart™ 1.0	Phenochart	https://www.akoyabio.com/support/software/phenochart-whole-slide-viewer/
ImageScope (version 12.3.0.5056)	Leica	https://www.leicabiosystems.com/en-de/digital-pathology/manage/aperio-imagescope/
ZEN 3.1	ZEISS	https://www.micro-shop.zeiss.com/en/us/system/zen+software/software+zen/zen+-+basic+software/410135-1002-310
bcl2fastq (version 2.20.0.422)	Illumina	https://support.illumina.com/sequencing/sequencing_software/bcl2fastq-conversionsoftware.html
Cell Ranger (version 6.1.2)	10x Genomics	https://support.10xgenomics.com/single-cell-gene-expression/software/pipelines/6.1/what-is-cell-ranger
CellBender (version 0.2.0)	Fleming et al.[99]	https://github.com/broadinstitute/CellBender
DoubletFinder (version 2.0.3)	McGinnis et al.[100]	https://github.com/chris-mcginnis-ucsf/DoubletFinder
Seurat (version 4.1.1)	Hao et al.[101]	https://satijalab.org/seurat/index.html
muscat (version 1.12.0)	Crowell et al.[102]	https://bioconductor.org/packages/release/bioc/html/muscat.html
RcisTarget (version 1.6.0)	Herrmann et al.[103]	https://github.com/aertslab/RcisTarget
Cytoscape (version 3.10.0)	Shannon et al.[104]	https://cytoscape.org/
ggpubr (version 0.6.0)	N/A	https://github.com/kassambara/ggpubr
Metascape (version 3.5)	Zhou et al.[105]	http://metascape.org
ggplot2 (version: 3.4.2)	Wickham et al.[106]	https://ggplot2.tidyverse.org/
pheatmap (version: 1.0.12)	N/A	https://cran.r-project.org/web/packages/pheatmap/index.html
glmnet (version: 4.1.7)	Friedman et al.[107]	https://glmnet.stanford.edu/articles/glmnet.html
Augur (version 3.1.0)	Skinnider et al.[108]	https://github.com/neurorestore/Augur
hdWGCNA (version 0.2.19)	Morabito et al.[109]	https://smorabit.github.io/hdWGCNA/
Clusterprofiler (version 3.1.0)	Yu et al.[110]	https://bioconductor.org/packages/release/bioc/html/clusterProfiler.html
Trim Galore (version 0.6.7)	N/A	https://github.com/FelixKrueger/TrimGalore
STAR (version 2.7.1a)	Dobin et al.[111]	https://github.com/alexdobin/STAR
StringTie (version 2.1.7)	Pertea et al.[112]	https://github.com/gpertea/stringtie
Mfuzz (version 2.58.0)	Futschik et al.[113]	https://bioconductor.org/packages/release/bioc/html/Mfuzz.html
GSVA (version 1.46.0)	Hanzelmann et al.[114]	https://bioconductor.org/packages/devel/bioc/vignettes/GSVA/inst/doc/GSVA.html
limma (version 3.54.1)	Ritchie et al.[115]	https://bioconductor.org/packages/release/bioc/html/limma.html
DEP (version 1.20.0)	Zhang et al.[116]	https://www.bioconductor.org/packages/release/bioc/html/DEP.html
SeSaMe (version 3.18)	Zhou et al.[117]	https://bioconductor.org/packages/release/bioc/html/sesame.html
FreeSurfer v6.0.0	Fischl et al.[118]	https://surfer.nmr.mgh.harvard.edu/
AFNI	Cox et al.[119]	https://doi.org/10.1006/cbmr.1996.0014

(*Continued on next page*)

Please cite this article in press as: Yang et al., Metformin decelerates aging clock in male monkeys, Cell (2024), https://doi.org/10.1016/j.cell.2024.08.021

Continued

REAGENT or RESOURCE	SOURCE	IDENTIFIER
FSL	FMRIB, Oxford	https://fsl.fmrib.ox.ac.uk/fsldownloads_registration
ANTS	Avants et al.[120]	https://www.nitrc.org/projects/ants
MATLAB (v.2021b)	The MathWorks Inc	https://www.mathworks.com/
BrainNet Viewer	Xia et al.[121]	https://www.nitrc.org/projects/bnv
SPSS Statistics	IBM	https://www.ibm.com/products/spss-statistics

EXPERIMENTAL MODEL AND STUDY PARTICIPANT DETAILS

Ethical statement

All experimental processes in this study comply with the Animal Care and Use Institutional Committee of the Institute of Zoology (IOZ-IACUC-2021-187), Animal Care and Use Institutional Committee of the Institute of Biophysics (IBP-NHP-004(21)), Research Ethics Committee of Beijing Institute of Genomics, Chinese Academy of Sciences (China National Center for Bioinformation) (2022A009), Chinese Academy of Sciences and Committee of Xieerxin Biology Resource (XEX20211203).

Experimental cynomolgus monkey

In this study, all male cynomolgus monkeys originated from Southeast Asia. Prior to long-term metformin treatment, monkeys had no clinical or experimental background, which could impact physiological aging or heighten sensitivity to diseases. The monkeys were kept in a clean breeding room with 25°C temperature and a 12-12 hours (h) light-dark cycle at Beijing Institute of Xieerxin Biology Resource, a Laboratory Animal Care accredited facility, fully compliant with all applicable local regulations pertaining to animal experiments. Monkeys were fed three meals and had free access to water. Along with breakfast, the O-Met group was treated every day with 20 mg/kg metformin administered through drinking water over the duration of the study (40 months). The Y-Ctrl group consists of individuals aged 3-5 years, the M-Ctrl group consists of individuals aged 10-12 years, and the O-Ctrl and O-Met groups consist of individuals aged 16-19 years at the endpoint. The typical lifespan for cynomolgus monkeys spans 25 to 30 years, with the record longevity reaching up to 39 years.[122–126]

METHOD DETAILS

Routine physical examination

Every three months, O-Ctrl and O-Met group monkeys received a routine physical examination, including assessment of body weight, body length, glucose tolerance, and routine blood and urine tests, analyzed by Bejing North Institute of Biotechnology Co.,Ltd. (China) every 3 months. At the endpoint, routine blood tests, blood hormone tests and blood biochemistry tests were also analyzed by Bejing North Institute of Biotechnology Co.,Ltd. (China).

Structural MRI

Structural MRI scanning was conducted at the Beijing MRI Center for Brain Research (BMCBR). The anesthesia and MRI procedures followed the guidelines outlined in the US National Institutes of Health Guide for the Care and Use of Laboratory Animals and were approved by the Institutional Animal Care and Use Committee of the Institute of Biophysics, Chinese Academy of Sciences (CAS). Prior to MRI scanning, the animals were premedicated with atropine (0.05 mg/kg, intramuscular) followed by ketamine (10 mg/kg, intramuscular). Anesthesia was maintained throughout the MRI session with continuous intravenous propofol at 10 mg/kg/h. The levels of EtCO2 and respiratory rate were monitored utilizing a magnetic-resonance compatible monitoring system to ensure optimal anesthesia. To prevent hypothermia, we carefully covered animals with a blanket during the scanning procedure. Imaging data were acquired utilizing a 3T Siemens Prisma MRI scanner with a custom-designed surface coil array (four elements). High-resolution T1-weighted and T2-weighted whole-brain anatomical images were obtained for each monkey. T1-weighted images were acquired using a magnetization-prepared rapid gradient echo (MPRAGE) sequence (voxel size = 0.5 mm isotropic, TE = 2.84 ms, TR = 2200 ms, flip angle: 8°), while T2-weighted images were acquired using a SPACE sequence (voxel size = 1.0 mm isotropic, TE = 392 ms, TR = 3200 ms, flip angle: 120°). The structural MRI analysis in this study involved 6 young monkeys in the Y-Ctrl group, 3 mature monkeys in the M-Ctrl group, 8 old monkeys in the O-Ctrl group, and 6 old monkeys in the O-Met group. Cortical thickness measurements were conducted independently for both the left and right hemispheres of each subject's brain.

Extraction of structural data

The structural data were processed utilizing Analysis of Functional NeuroImages software (AFNI), FMRIB Software Library (FSL), FreeSurfer, and Advanced Normalization Tools (ANTs).[118–120,127] First, the T1 image of each animal was nonlinearly registered to

the NIMH Macaque Template (NMT, version 2.0).[42] This registration process generated a brain mask by inversely applying the registration results to a skull-free version of the template. The obtained brain mask was then used as the initial skull stripping mask for both the T1 and T2 images, which had been co-registered to the T1 image using a rigid-body transformation. A bias correction procedure was applied to result in a high-contrast T1 image by combining the T1 and T2 images. Next, we processed the T1 images using a customized pipeline based primarily on FreeSurfer[118] to generate white-matter and gray-matter surfaces. To ensure accuracy, two experts manually examined and edited the skull stripping and white-matter masks slice-by-slice along axial and coronal planes. The revised versions were then used to generate the final white-matter and gray-matter surfaces. Subsequently, the brain surfaces were segmented into four lobes (frontal, parietal, temporal, and occipital) and 88 regions per hemisphere, following the Cortical Hierarchy Atlas of the Rhesus Macaque 1 (CHARM1) and CHARM5 atlas. The cortical thickness of each lobe and region was extracted using FreeSurfer.

Group analyses

No significant hemispheric asymmetries were observed in either the aging or metformin experiments. Therefore, for the group analyses, the results from the right and left hemispheres were collapsed.

To examine the changes in cortical lobes or regions during aging, we employed a general linear mixed model (GLMM) in the control groups (i.e., young control group and old-age control group), with Age as the fixed factor and Hemisphere as the random factor. The significance level for the aging effect was set at $P < 0.05$ [false discovery rate (FDR) corrected for multiple comparisons] at the lobe and region levels.

To evaluate the effects of metformin on aging, we conducted GLMMs on each lobe and region to compare the structural data between the old-age control group and the metformin group, with Hemisphere as the random factor. The significance level for the metformin effect was set at $P < 0.05$ (FDR corrected for multiple comparisons) at the lobe and region levels.

Notably, all cortical thickness data were corrected with the intracranial volume of the corresponding hemisphere.[128] Furthermore, when the data distribution did not meet the normality assumption as determined by the Shapiro-Wilk test, we employed the Mann-Whitney test as an alternative to the GLMM.

Cognitive testing

To carry out cognitive testing, we used a modified version of the Wisconsin General Test Apparatus (WGTA) to assess the basic memory, learning, and cognitive flexibility in aged monkeys.[40,137,138] To minimize any potential difficulties associated with monkeys when leaving their home cage, we modified the equipment and placed it directly in front of the monkey cage. The cognitive experiment was divided into four stages: Adaptation, Delay, Discrimination, and Reversal.

Adaptation

During the initial phase, the baffle in front of the experimenter was closed to prevent the animal from observing the experimenter's actions, while the baffle in front of the monkey remained open. In the first step, food was placed in front of the well, and the monkey needed to successfully obtain the food five consecutive times to progress to the next step. Subsequently, food was placed inside the well, and again, the monkey had to successfully retrieve the food five times in a row. The third step involved placing the food in the well and introducing a block behind it. If the monkey successfully obtained the food five times consecutively, it advanced to the next step. In the fourth step, the food was placed in the well, and the block covered half of the well. Success in obtaining the food five times in a row allowed the monkey to proceed. Finally, in the fifth step, the food was placed inside the well, and the block completely covered the well. It was considered a successful adaptation if the monkey successfully displaced the block to obtain the food. A session consisted of 25 consecutive trials, with more than 20 successful tests indicating that the monkey had completed the adaptation stage.

Delay

The baffle in front of the monkey was opened, while the presentation board remained out of reach. The experimenter placed food in one of two wells and covered it with a block. Another block with the same shape and color was placed on the well without food, on the opposite side of the presentation board. The baffle was then closed, and the timer was initiated. The baffle was opened when the predetermined time elapsed (i.e., 1s, 3s, 5s). To access the food, the monkey had to displace the block covering the well with food and retrieve the food within 60 seconds. If the monkey failed to respond within the designated time frame, the trial was terminated by lowering the baffle in front of the monkey. In each delay period, animals were tested for three sessions, each comprising 25 trials.

Discrimination

Two blocks with identical shapes but different colors (color A and color B) were employed, with color A designated as the correct choice and color B as the incorrect choice. The assignment of colors was balanced across the animals. Food was placed in one of the wells, covered with the block of color A, while the empty well on the opposite side was covered with the block of color B. The baffle was opened, requiring the monkey to displace the block of color A and successfully retrieve the food within 60 seconds to achieve success. Animals were tested for six sessions, each consisting of 25 trials.

Reversal

This stage mirrored the Discrimination step but reversed the correct and incorrect choices. That is, color B was designated as the correct choice, while color A became incorrect. To access the food, the monkey had to displace the block of color B within 60 seconds to retrieve the food successfully. Similar to the Discrimination stage, animals were tested for six sessions, each comprising 25 trials.

Please cite this article in press as: Yang et al., Metformin decelerates aging clock in male monkeys, Cell (2024), https://doi.org/10.1016/j.cell.2024.08.021

In the cognitive testing phase, 5 monkeys from the O-Ctrl group and 6 from the O-Met group participated. For each participant, accuracy was assessed across sessions in the Delay, Discrimination, and Reversal stages, with 9, 6, and 6 sessions, respectively. To discern performance variances between the O-Met and O-Ctrl groups, a series of ANOVAs were applied, when the data met the normality assumption, as verified by the Shapiro-Wilk test. If the assumption was not met, we employed the Mann-Whitney test instead.

Micro-CT analysis

As previously described, the monkey maxilla and mandible were subjected to scanning using a Micro-CT Scanner (PE Quantum FX, USA).[65] Subsequently, the acquired images were transformed into a three-dimensional format. The evaluation of the distance between the cementoenamel junction and alveolar bone crest (CEJ-ABC distance) was constructed employing a previously documented approach with minor adjustments. In brief, the CEJ-ABC distances of the premolars and molars within both the maxilla and mandible of each primate subject were measured and then averaged.

Tissue dissociation

Following a 40-month metformin treatment, the monkeys were anesthetized, and subsequently, a saline solution was perfused systemically through the heart. A total of 79 tissues from 11 systems were sampled (details in Table S1). Tissues were stored with 4% paraformaldehyde, embedded in OCT and cryopreserved in liquid nitrogen.

RNA-seq Library construction and sequencing

Total RNA from 79 tissues/organs in 11 systems was extracted with TRIzol reagent, after which the library was constructed as previously described.[7] Then, high-throughput sequencing was carried out for each sample on MGI DNBSEQ-T7 platform with PE150 (Novogene Bioinformatics Technology Co. Ltd.). The bulk RNA-seq sample sizes for each tissue are listed in Table S2.

Protein extraction and trypsin digestion

The blood plasma proteome from each monkey was analyzed with Data Independent Acquisition (DIA) based proteomics. Firstly, 100 μL of blood plasma from each monkey was mixed with 100 μg of nanomagnetic beads for high-abundance protein depletion.[129] After mixing with lysis buffer (8 M urea, 1% protease inhibitor cocktail), the protein concentration of the samples was determined using a BCA protein assay kit. 10 mM DTT was added to the protein extract, followed by incubation at 56°C for 1 hour. After cooling to room temperature, 55 mM IAA was added, and the mixture was incubated in the dark at room temperature for 45 minutes. Based on the protein concentration measurements, an appropriate amount of protein from each sample was enzymatically digested using the FASP (filter-aided sample preparation) method.[130] The next day, samples were centrifuged at 13000 × *g* for 10 minutes at room temperature, and the liquid in the collection tube was transferred to a new centrifuge tube and vacuum-dried. Finally, the samples were desalted using a C18 desalting column.

Mass spectrometry analysis of plasma proteins

The chromatographic mobile phase consisted of 0.1% FA as phase A and 80% ACN with 0.1% FA as phase B. The dried peptide segments were fully dissolved in phase A (0.1% FA) and centrifuged at 17000 × *g* for 15 minutes. The supernatant was transferred to a built-in tube and placed in an automatic sample injector. Using an EASY-nLC 1200 liquid chromatography system (Thermo Fisher Scientific, USA), the peptides were loaded onto a C18 trap column at a flow rate of 3 μL/min and then eluted to a C18 analytical column (150 μm inner diameter) at a flow rate of 600 nl/min. The chromatographic elution conditions were as follows: 0 min-45 min, linear increase of phase B (ACN with 0.1% FA) from 7% to 32%; 45 min-50 min, linear increase of phase B from 32% to 42%; 50 min-55 min, linear increase of phase B from 42% to 95%, maintained until 60 min. The Thermo Scientific Q Exactive HF mass spectrometer was used with a Nanospray Flex ion source, set at an ion spray voltage of 2.3 kV and an ion transfer tube temperature of 320°C. The plasma proteomics sample sizes for each tissue are listed in Table S2.

Mass spectrometry analysis of plasma metabolites

The plasma samples were extracted using a methanol solution at a 1:4 ratio, followed by shaking for 3 minutes and centrifugation at 4000 × *g* for 10 minutes at 20°C to precipitate the mixtures. Four aliquots of 100 μL supernatant were then transferred to sample plates and dried using blowing nitrogen. Subsequently, they were re-dissolved in reconstitution solutions for injection into UPLC-MS/MS systems. The UPLC-MS/MS analysis was performed using the ACQUITY 2D UPLC system from Waters paired with the Q Exactive (QE) hybrid Quadrupole-Orbitrap mass spectrometer. The QE operated in positive ESI mode, and the UPLC column was C18 reverse-phase (UPLC BEH C18, 2.1x100 mm, 1.7 μm; Waters). The mobile phases used for gradient elution were water (A) and methanol (B), which contained 0.05% PFPA and 0.1% FA. The plasma metabolomics sample sizes for each tissue are listed in Table S2.

DNA preparation

Based on the manufacturer's guidance of TIANamp Genomic DNA Kit, DNA extraction of monkey tissues was performed. After the tissue was broken in physiological saline, the supernatant was removed by centrifugation, and then 200 μL GA buffer was added.

Please cite this article in press as: Yang et al., Metformin decelerates aging clock in male monkeys, Cell (2024), https://doi.org/10.1016/j.cell.2024.08.021

20 μL of proteinase K was added to the tissue disruption mixture and incubated at 56 °C for 2 h. 200 μL GB was then added to the mixture and incubated at 70 °C for 10 min. The mixture was then mixed with 200 μL absolute ethanol, and the resulting solution passed through an adsorption column and washed with GD and PW buffer. The adsorption column was dried, and then the DNA was eluted using EB buffer. The concentration of DNA was measured and stored at -20 °C.

Microarray experiment of DNA methylation

DNA methylation data were generated using the custom Illumina chip, 'HorvathMammalMethylChip40'. This array focuses only on 36k CpGs that are highly conserved across mammals.[131,132] We utilized 34,838 CpGs that were conserved based on the Macaca fascicularis genome (version 5.0.100). Beta values were defined for each probe by SeSaMe.[117] The DNA methylation sample sizes for 7 tissues are listed in Table S2.

Nuclei sorting and snRNA-seq on the 10x genomics chromium platform

As previously described, the nuclei of liver (LL) and brain (FL) were isolated from 3 monkeys in each group randomly.[62,64] Fresh frozen tissues (liver (LL) and brain (FL)) were ground in liquid nitrogen. Then, the homogenization buffer was homogenized with the tissues using a freezing tissue grinding system (TissueLyser-24, Jingxin Industrial Development, China). The homogenization buffer included 10 mM Tris-HCl buffer, 250 mM sucrose, 25 mM $MgCl_2$, 25 mM KCl, 1 mM DTT, 1 × protease inhibitor, 0.4 U/mL Superasin, 0.4 U/mL RNaseIn, 1 mM PI, 0.1% Triton X-100 (v/v), and 10 ng/mL Hoechst 33342. Next, the homogenate is filtered through a 40 μm filter. The nuclei were centrifuged at 500 × *g* for 8 min and then suspended in PBS containing 0.3% BSA, 0.4 U/mL Superasin and 0.4 U/mL RNaseIn. Hoechst 33342 and PI-positive nuclei were sorted using FACS (BD Influx) and enumerated utilizing a dual fluorescence cell counter (Luna-FLTM, Logos Biosystems). Based on the 10x Genomics Single-Cell 3' system, the nuclei were subjected to single-nucleus capture. Around 7,000 nuclei per sample were obtained using the standardized 10x capture and library preparation procedure (10x Genomics) and subjected to sequencing using PE150 on the NovaSeq 6000 Sequencing System (Illumina, 20012866).

SA-β-gal staining

Frozen tissue sections were thawed to room temperature, air-dried, and subsequently washed with PBS. Samples were then treated with a fixed solution (2% formaldehyde and 0.2% glutaraldehyde in PBS) for 15 minutes (min) and then subjected to incubation with a SA-β-gal staining solution (including 5 mM potassium ferricyanide, 5 mM potassium ferrocyanide, 1 mg/mL X-gal, 150 mM NaCl, and 2 mM $MgCl_2$) at 37°C for a duration of 12 h. Finally, 50% glycerol was used for slide mounting. Similarly, cultured cells underwent fixation with a solution containing 2% formaldehyde and 0.2% glutaraldehyde for 15 min, followed by incubation with a SA-β-gal staining solution (including 5 mM potassium ferricyanide, 5 mM potassium ferrocyanide, 1 mg/mL X-gal, 150 mM NaCl, and 2 mM $MgCl_2$) at 37 °C for 12 h. Subsequent imaging was captured using a Nikon microscope, and quantification was carried out utilizing ImageJ.

Hematoxylin and eosin (HE) staining

Paraffin-embedded tissue specimens were sectioned into slices measuring 5 μm thick slices employing a rotary microtome. Subsequently, these sections underwent deparaffinization in xylene and rehydration through a sequential series of alcohol solutions (100%, 100%, 95%, 80%, 70%). They were then immersed in hematoxylin solution for 5 min, followed by washing three times to eliminate excess hematoxylin, and subjected to differentiation with 1% acid alcohol for 2 seconds (s), followed by thorough washing three times. Lastly, eosin was applied for counterstaining, and the sections were dehydrated through an ethanol and xylene gradient before being mounted using neutral gum. Subsequent imaging was captured using a Nikon microscope, and quantification was carried out utilizing ImageJ.

Masson's trichrome staining

Based on the manufacturer's guidance, Masson's trichrome staining was executed. Following tissue embedding in paraffin, samples were sectioned into slices measuring 5 μm in thickness. These sections underwent deparaffinization using xylene and were gradually rehydrated through successive alcohol solutions of 100%, 100%, 95%, 80% and 75%, followed by washing three times. Subsequently, the sections were immersed in potassium bichromate solution at 60 °C for 1 h. Following a 10-minute rinse in running tap water, the sections underwent sequential staining with iron hematoxylin solution for a duration of 5 min. Next, the sections were immersed in Ponceau-acid fuchsin working solution for a duration of 10 min. Following this, sections underwent differentiation in phosphomolybdic-phosphotungstic acid solution for a duration of 10 min, followed by staining in aniline blue solution for a duration of 5 min. After washing three times, differentiation was carried out in a 1% acetic acid solution for 2 minutes. Following dehydration in 50%, 75%, 85%, 95% and 100% alcohol, and clearance with xylene, the sections were covered using a cover glass and mounted using neutral gum. Image acquisition was performed using PerkinElmer Vectra Polaris.

Aggresome staining

After deparaffinization and antigen retrieval, paraffin sections are stained for aggresome based on the manufacturer's guidelines for the proteostat protein aggregation assay kit, and then destained with 1% acetic acid for 20 minutes. After staining the cell nucleus

Please cite this article in press as: Yang et al., Metformin decelerates aging clock in male monkeys, Cell (2024), https://doi.org/10.1016/j.cell.2024.08.021

with Hoechst 33342, the sections are mounted. The cells are stained similarly to paraffin sections, but without deparaffinization and antigen retrieval. Subsequently, images were captured utilizing a Zeiss LSM 980 confocal system.

ROS analysis

The fresh cells are incubated with the CM-H2DCFDA and Hoechst 33342 at room temperature for 30 min. After washing three times, the image was captured using an OLYMPUS CKX53 cell culture microscope.

Immunohistochemistry staining

Following paraffin embedding, the tissue was cut into 5 μm thick sections using a microtome, followed by deparaffinization with xylene and subsequent hydration through a gradient of alcohol concentrations including 100%, 100%, 95%, 85%, 75% alcohol, and concluding with running tap water. Antigen retrieval was conducted by exposing the sections to microwave irradiation in 10 mM sodium citrate buffer (pH = 6.0) for a duration of 20 min. Following cooling to room temperature, the sections underwent triple rinsing with PBS. Permeabilization was achieved by treating the sections with 0.4% Triton X-100 for 30 min, subsequent to blocking of endogenous peroxidase activity with 3% H_2O_2 for 10 min. Subsequently, the sections were blocked with 5% donkey serum (diluted in PBS) for 1 h at room temperature, followed by being incubated with primary antibodies at 4°C overnight. Then, the sections were subjected to a 20-minute incubation with an enhancement solution, followed by exposure to secondary antibodies at room temperature for 1 h. Then, colorimetric detection was carried out using a DAB Kit, followed by staining with hematoxylin. Next, the sections were treated with 1% hydrochloric acid (in 70% alcohol) for differentiation. Hematoxylin staining was reversed to blue by immersion in 1% ammonia water for 15 s. Ultimately, the sections were dehydrated using a gradient of alcohol concentrations, including 50%, 75%, 85%, 95%, 100% alcohol, and xylene, prior to being mounted with neutral gum. Image acquisition was performed using PerkinElmer Vectra Polaris.

Transmission electron microscopy (TEM) analysis of myelin thickness

The frontal lobe was carefully isolated and treated with 2.5% (v/v) glutaraldehyde (in 0.1 M phosphate buffer), after undergoing four washes with phosphate buffer. Subsequently, the tissues were subjected to post-fixation in 1% (w/v) osmium tetroxide in phosphate buffer for 2 h at 4 °C, followed by dehydration through a graduated series of ethanol concentrations (30%, 50%, 70%, 80%, 90%, 100%, 100%, 7 min each) until reaching pure acetone twice of 10 min. Following this, the samples were infiltrated with graded mixtures (3:1, 1:1, 1:3) of acetone and SPI-PON812 resin (10 g DDSA, 16.2 g SPI-PON812, and 8.9 g NMA), and subsequently transferred to pure resin. Ultimately, the tissues were embedded in pure resin containing 1.5% BDMA, polymerized for 12 h at 45°C followed by 48 h at 60°C. Ultra-thin sections measuring 70 nm in thickness were obtained using a microtome (Leica EM UC6) and subjected to double-staining using uranyl acetate and lead citrate. Subsequently, images were captured using a transmission electron microscope (FEI Tecnai Spirit120kV). Myelin thickness in the frontal lobe was quantified utilizing ImageJ software.

Golgi staining

Based on the manufacturer's guidance of FD Rapid GolgiStain Kit, Golgi staining of the monkey's frontal lobe was performed. The monkey frontal lobe was soaked in solutions A and B at room temperature for a duration of 2 weeks, then immersed in solution C for a duration of 72 hours at 4°C. Slices of FL were obtained with a Leica CM3050 S Cryostat at 150 μm. Subsequently, images of frontal lobe sections were captured using a ZEISS LSM 980 confocal microscope.

Oil red O staining

10 μm thick frozen tissue sections underwent a 15-minute air-drying process, followed by washing three times. Subsequently, the sections were subjected to fixation using 4% PFA for 10 min, and underwent an additional three times of PBS washes. Following 1 s exposure to 60% isopropanol, the sections were stained with 60% Oil Red O for 15 min, followed by another series of PBS washes. Hematoxylin staining was then performed for 5 min, subsequent to sequential immersion in 1% hydrochloric acid (in 70%alcohol), and 1% ammonia water, respectively. Finally, the sections were sealed utilizing 50% glycerol.

Immunofluorescence staining

For tissue immunofluorescence staining, following embedding in paraffin, tissue sections were sliced at 5 μm, which underwent identical procedures as those utilized for immunohistochemistry staining, encompassing deparaffinization and antigen retrieval. Subsequently, the sections were treated with 0.4% Triton X-100 (diluted in PBS) for 30 min. In the case of cell immunofluorescence staining, cells were treated with 4% PFA for 10 min and treated with 0.4% Triton X-100 (diluted in PBS) for 15 min. After PBS washes, tissue sections or cells were incubated with blocking buffer (5% donkey serum in PBS) for 1 hour at room temperature and incubated with primary antibodies at 4 °C overnight. On a subsequent day, the sections were exposed to secondary antibodies and nuclear dye for 1 hour at ambient temperature. Ultimately, images were acquired employing the Zeiss LSM 980 confocal system.

Human embryonic stem cell (hESC) culture

We cultured WT and Nrf2 E82G hESCs following established methodologies.[58] The hESCs were sourced from the WiCell Research Institute and cultured on mouse embryonic fibroblast feeder cells using a specialized medium formulated for human embryonic stem

cells. This medium consisted of 20% Knockout Serum Replacement (Invitrogen), 80% DMEM/F12 (Invitrogen), 10 ng/mL human basic fibroblast growth factor (bFGF, Joint Protein Central), 55 μM β-mercaptoethanol (Invitrogen), 1% non-essential amino acids (NEAA) (Invitrogen), 1% penicillin/streptomycin (PS, Invitrogen), 1% GlutaMAX (Invitrogen), and 0.01% plasmocin (Invitrogen). Importantly, all cells were subjected to thorough testing to confirm the absence of mycoplasma contamination.

Human neuron (hNeuron) differentiation

Directed differentiation of WT and Nrf2 E82G human neural stem cells (hNSCs) from WT and Nrf2 E82G hESCs was conducted following established protocols.[58] Initially, hESCs were cultured on mouse embryonic fibroblast feeder cells, and upon reaching a confluence of 20-40%, the ESCs were treated with NID-1 medium. This medium formulation comprised 50% neurobasal medium, 50% advanced DMEM/F12, 1× B27 supplement, 1× N2 supplement, 2 mM GlutaMAX, 10 ng/mL hLIF, 2 μM dorsomorphin, 3 μM SB431542, 4 μM CHIR99021, and 0.1 μM compound E. Following a 2-day incubation period, the NID-1 medium was changed by the NID-2 medium (which is similar to NID-1 but lacks dorsomorphin), and the cells were allowed to proliferate further for another 5 days. Subsequently, the cell cultures were dissociated into single cells using Accutase, transferred onto matrigel-coated plates, and cultured with Neural Progenitor Cell Maintenance Medium. This maintenance medium consisted of 50% advanced DMEM/F12, 50% Neurobasal medium, 2 mM GlutaMAX, 2 μM SB431542, 10 ng/mL hLIF, 3 μM CHIR99021, 1× N2 supplement and 1× B27 supplement.

WT and Nrf2 E82G hNSCs were seeded onto matrigel-coated plates at a seeding density of 3 × 10^4 cells per well for 24-well plates and 1 × 10^5 cells per well for 6-well plates and allowed to culture for 3 days. Cells were then exposed to a specialized neuronal differentiation medium composed of advanced DMEM/F12, 10 ng/mL GDNF, and 10 ng/mL BDNF, 200 μM ascorbic acid (Sigma), 400 μM dbcAMP, 1× B27 supplement and 1× N2 supplement. Laminin was introduced into the specialized neuronal differentiation medium 3 days post-neuronal induction to facilitate and stabilize the neuronal differentiation process. The cells were cultured in this neuronal differentiation medium for a minimum of 14 days before being employed for subsequent experiments. For prolonged culture periods, fresh medium was replaced every 3 days to sustain optimal cell conditions until the designated time of sample collection.

Knockdown of Nrf2 utilizing small interfering RNA (siRNA)

The inhibition of Nrf2 expression via siRNA in hNeurons was executed using established methodologies as outlined previously.[133] The siRNAs were synthesized by Ribobio (China). Transfections of RNA oligonucleotides were accomplished using lipofectamine® 3000 Reagent, adhering to the manufacturer's guidelines. Cells were collected for analysis 48-72 hours after transfection. Detailed sequence information can be found in Table S5.

Metformin treatment of hNeurons

At prolonged culture periods, WT and Nrf2 E82G hNeurons were cultured long-term for 18 days before exposure to metformin at a concentration of 5 μM (in neuronal differentiation medium). As for si-NC and si-Nrf2 hNeurons, metformin treatment was performed from day 12. Fresh medium was replaced every 3 days to sustain optimal cell conditions until the designated time of sample collection.

Western blot analysis

Based on the previous method, western blot analysis was performed.[134] Initially, cell lysis was performed using RIPA lysis buffer (containing protease inhibitors, phosphatase inhibitors and PMSF). The total protein concentration was then determined utilizing the BCA assay according to the manufacturer's guidelines. 5× SDS loading buffer was added to the lysis mixture and the sample was incubated at 105°C for 10 min. The protein lysates underwent separation via SDS-PAGE. Next, proteins were transferred to PVDF (polyvinylidene fluoride) membranes and subsequently blocked using 5% BSA in 1× TBST solution. Overnight incubation with primary antibodies at 4 °C ensued. The PVDF membranes were immersed in HRP-conjugated secondary antibodies at room temperature for 1 h. Finally, it was exposed by the ChemiDoc XRS system.

RNA extraction

For RNA extraction, cell pellets were first resuspended in TRIzol Reagent within centrifuge tubes, subsequent to the addition of 200 μL of chloroform. The resulting mixture underwent gentle agitation and was placed at ambient temperature for 15 minutes. Following this, centrifugation was performed at 12,000 × *g* at 4 °C for 15 min to separate the components. Subsequently, 400 μL of the upper liquid phase was cautiously transferred to a new centrifuge tube and combined with an equal volume of isopropanol at room temperature for 10 min. The mixture was then subjected to centrifugation once more at 12,000 × *g* at 4 °C for 10 min. Upon removal of the supernatant, 1 mL of pre-cooled 75% ethanol was added to the sediment for purification, followed by centrifugation at 8,000 × *g* at 4 °C for 5 min. After the supernatant was carefully removed, the residual ethanol was allowed to evaporate. Finally, the RNA was dissolved in 20 μL of DEPC water, after which the RNA concentration was quantified.

Real-time quantitative PCR

1 μg total RNA was incubated at 42 °C for 2 min with 5× gDNA wiper Mix. Then, the total RNA was mixed with 4× HiScript IV qRT SuperMix and incubated at 37 °C for 15 min before incubated at 85 °C for 5 s to synthetic cDNA. The real-time quantitative PCR

Please cite this article in press as: Yang et al., Metformin decelerates aging clock in male monkeys, Cell (2024), https://doi.org/10.1016/j.cell.2024.08.021

assays were performed utilizing the THUNDERBIRD SYBR qPCR mix on a Real-Time PCR instrument. Normalization of all data was conducted relative to the internal control, and analysis was carried out using the $2^{-\Delta\Delta Cq}$ approach. Primer pairs utilized in this investigation are listed in Table S5.

Bulk RNA-seq data processing

To trim the adaptor and remove low-quality reads, raw reads were processed by Trim Galore software (version 0.6.7). Cleaned reads of 79 monkey tissues/organs were aligned to the *Macaca fascicularis* reference genome (5.0, ensemble 91) using STAR (version 2.7.1a)[111] with strand-specific parameters. The Fragments Per Kilobase per Million (FPKM) mapped reads were calculated by StringTie (version 2.1.7).[112] To obtain age-dependent genes in four representative clusters, R package Mfuzz (version 2.58.0)[135] was employed to perform fuzzy c-means clustering based on $\log_2$-transformed FPKM, and highly overlapping clusters were merged. The details of the age-dependent genes are listed in Table S2.

Gene set variation analysis (GSVA)

Based on $\log_2$-transformed FPKM of age-dependent genes in each cluster, GSVA score was calculated by R package GSVA (version 1.46.0).[114] Gene sets were obtained from Molecular Signatures Database (MSigDB).

The rescue score for each tissue was calculated as follows:

$$Rescue\ score = -\frac{\overline{GSVA\ score_{O-Met}} - \overline{GSVA\ score_{O-Ctrl}}}{\overline{GSVA\ score_{O-Ctrl}} - \overline{GSVA\ score_{Y-Ctrl}}}$$

Differentially expressed pathways were identified using R package limma (version 3.54.1) with default parameters.[115] The pathways with $P < 0.05$ were considered significant. Rescue pathways were identified as a subset of pathways significantly up-regulated/down-regulated in cluster U/D that were changed in the opposite direction upon metformin treatment.

Data-independent acquisition (DIA) quantitative proteomics

Peptide identification was performed by searching against the UniProt *Macaca fascicularis* database by Spectronaut. *P*-value was calculated using the kernel density estimator, and Q-value cutoff at precursor and protein levels was set to 0.01. Protein abundance was quantified by the peak area of production, with at least three productions selected for average intensity quantification. The protein abundances were imputed by k-nearest neighbor algorithm, $\log_2$-transformed and normalized using *vst* function by R package DEP (version 1.20.0).[116] To identify age-dependent proteins in four representative clusters, R package Mfuzz (version 2.58.0) was employed to perform fuzzy c-means clustering on normalized protein abundance, and highly overlapping clusters were merged. Differentially expressed proteins (DEPs) were identified using R package limma (version 3.54.1)[115] with parameters (P-value < 0.05 and $|\log_2(\text{fold change})| > 0.5$). Rescued DEPs were identified as a subset of age-dependent DEPs in cluster U/D that were changed in the opposite direction upon metformin treatment. The details of the rescued DEPs are listed in Table S2.

Metabolomic data analysis

For metabolomic data analysis, ion peaks were extracted using proprietary in-house IT hardware and software after pre-processing of raw data and data quality control inspection. Metabolites were identified by searching an in-house library generated from running reference standards commercially purchased or obtained from other sources. Identification of metabolites in samples requires strict matching of three criteria between experimental data and library entry: narrow window retention index (RI), accurate mass with variation less than 10 ppm and MS/MS spectra with high forward and reverse searching scores. Metabolite quantification is achieved by calculating area-under-the-curve, yielding the raw peak area for each metabolite. The normalized peak areas were then $\log_2$-transformed to reduce data distribution skewness and be in an approximate normal distribution. Missing values in the peak area matrix were imputed by using the minimal detection value of a metabolite among all samples. To identify age-dependent metabolites in four representative clusters, R package Mfuzz (version 2.58.0)[135] was employed to perform fuzzy c-means clustering on normalized metabolite abundance, and highly overlapping clusters were merged. The details of the rescued DE metabolites are listed in Table S2.

DNA methylation aging clock analysis

The processed beta value matrix was used for aging clock analysis as previously described.[96] In brief, Pearson correlation values were calculated for all methylated sites with chronological age including 3 groups (Y-Ctrl, M-Ctrl, O-Ctrl) first. Only aging-related methylated sites (P-value < 0.05) were used for aging clock training. Utilizing the processed beta value matrix of these aging-related methylated sites as input data, and the chronological ages of each monkey (including 3 groups (Y-Ctrl, M-Ctrl, O-Ctrl)) as the training label, we employed a penalized regression model (ElasticNet, containing L1 regularization and L2 regularization) to construct DNA methylation aging clock, using the cv.glmnet function of the glmnet R package (version 4.1.7).[107] Alpha values were set from 0.01 to 0.99. Lambda values were determined using 10-fold cross-validation on the training set. To arrive at unbiased estimates of the accuracy of the DNA methylation aging clock, we performed a cross-validation scheme, Leave One Out Cross Validation (LOOCV).[136] By leaving out a single sample from the penalized linear regression, we predicted age for that sample

Please cite this article in press as: Yang et al., Metformin decelerates aging clock in male monkeys, Cell (2024), https://doi.org/10.1016/j.cell.2024.08.021

and iterated over all samples in all tissues. In this way, we considered model complexity and utilized the appropriate hyperparameters, selecting the model with the lowest mean absolute error (MAE) as the final model. R and MAE were used to measure the accuracy and compare it with the known aging clock model. Then, O-Met group was used as an input to predict DNAmAge. ΔAgeDiff was used to assess the geroprotective effects of metformin treatment. The details of DNAmAge and ΔAgeDiff in all tissues are listed in Table S3.

Multi-Model aging clock analysis

For bulk RNA-seq, aging-related genes were fitted by linear regression with chronological age by limma[115] (adjusted *P*-value < 0.05) with default parameters. Then, tissues with more than 10 aging-related genes were used for aging clock training. The expression matrix of these aging-related genes as input data, and the chronological ages of each monkey (including 3 groups (Y-Ctrl, M-Ctrl, O-Ctrl)) as the training label. The ElasticNet regression model was then trained with the training set (including 3 groups (Y-Ctrl, M-Ctrl, O-Ctrl)), using the cv.glmnet function of the glmnet R package (version 4.1.7)[107] to set the alpha values from 0.01 to 0.99. Lambda values were determined using 10-fold cross-validation on the training set. Then, we employed a methodology akin to DNAmAge to predict the transcriptAge of all samples. Additionally, we utilized the appropriate hyperparameters, selecting the model with the lowest MAE (Mean Absolute Error) as the final model. R and MAE were used to measure the accuracy and compare it with the known aging clock model. Then, the O-Met group was used as an input to predict transcriptAge, which was used to assess the geroprotective effects of metformin treatment. The details of ΔAge and ΔAgeDiff in all tissues are listed in Table S3.

For plasma proteomics and metabolomics, aging-related proteins and metabolites were fitted by linear regression with chronological age by limma[115] (*P*-value < 0.05) with default parameters between 3 groups (Y-Ctrl, M-Ctrl, O-Ctrl). Then, we employed a methodology akin to DNAmAge to construct the final model respectively and predict the proteinAge and metabAge of all samples. R and MAE were used to measure the accuracy and compare it with the known aging clock model. Then, the O-Met group was used as an input to predict proteinAge and metabAge, which was used to assess the geroprotective effects in metformin treatment. The details of ΔAge and ΔAgeDiff are listed in Table S3.

snRNA-seq data processing

The single-nuclei mRNA sequencing data were aligned to the Macaca fascicularis reference genome (5.0, ensemble 91) and counted by Cell Ranger (version 6.1.2) to generate a raw count matrix. Then, in the raw count matrix, the possible background noise was removed by CellBender (version 0.2.0)[99] with default parameters.

Clustering and identification of cell types for each tissue

The decontaminated count matrixes were converted into Seurat (version 4.1.1)[101] objects and processed in the order of the following steps:

1. Cells with fewer than 200 detected genes, more than 2.5% mitochondrial gene ratio for the frontal lobe and cells with fewer than 200 detected genes, more than 5% mitochondrial gene ratio for the liver were excluded.
2. SCTransform was used for normalization, then each Seurat objects were performed PCA analysis to provide priori knowledge for doublet detection by DoubletFinder (version 2.0.2).[100]
3. After filtering the doublets, all samples in each tissue were integrated across conducted using the standard Seurat procedure and the batch effect was corrected by using the CCA (rpca).
4. 30 PCs were used to execute the dimensionality reduction and clustering by using "FindNeighbors" and "FindClusters". UMAP were generated by "RunUMAP".
5. Marker genes for each cluster were performed using the Wilcoxon rank-sum test as statistical method in the "FindAllMarkers" function with the cutoff of $\log_2$(fold change) > 0.5, min.pct > 0.2 and adjusted *P*-values < 0.05. Cell types were assigned to each cluster using canonical marker genes. The details of the top 50 marker genes for each cell type are listed in Table S4.

Differential expression analysis from snRNA-seq data

For liver snRNA-seq data, age-dependent DEGs were calculated using the "FindallMarkers" in Seurat with the Wilcoxon rank-sum test in Y-Ctrl, M-Ctrl and O-Ctrl groups (|average_$\log_2$(fold change)| > 0.25, min.pct > 0.1 and adjusted *P* value < 0.05) in each cell type. In addition, differentially expressed genes between O-treated and O-Ctrl groups (O-Met/O-Ctrl) were calculated using the Seurat function "FindMarkers" with the Wilcoxon rank-sum test (|average_$\log_2$(fold change)| > 0.25, min.pct > 0.1 and adjusted *P* value < 0.05), named as Met DEGs. The details of the age-dependent DEGs and Met DEGs for each cell type are listed in Table S4.

For frontal lobe snRNA-seq data, age-dependent DEGs were calculated using the "FindallMarkers" in Seurat with the Wilcoxon rank-sum test in Y-Ctrl, M-Ctrl and O-Ctrl groups (|average $\log_2$(fold change)| > 0.15, min.pct > 0.1 and adjusted *P* value < 0.05) in each cell type. In addition, differentially expressed genes between O-treated and O-Ctrl groups (O-Met/O-Ctrl) were calculated using the Seurat function "FindMarkers" with the Wilcoxon rank-sum test (|average_ $\log_2$(fold change)| > 0.15, min.pct > 0.1 and adjusted *P* value < 0.05), named as Met DEGs. The details of the age-dependent DEGs and Met DEGs for each cell type are listed in Table S4.

Please cite this article in press as: Yang et al., Metformin decelerates aging clock in male monkeys, Cell (2024), https://doi.org/10.1016/j.cell.2024.08.021

snRNA-seq tissue-specific aging clock analysis

Owing to the sparsity of snRNA-seq data relative to bulk RNA-seq data, metacells were identified based on KNN by the function "MetacellsByGroups" from hdWGCNA package[109] with default parameters. Only cell types containing more than 3 metacells in each group were used for aging clock analysis. Then, the normalized metacell count matrix was split into 60% for training and 40% for testing. Each cell type normalized metacell count matrix was subsetted with their cell type-specific age-dependent DEGs. ElasticNet was trained in the training set by LOO to gain the final model, which presented the lowest MAE in the test set. R and MAE were used to measure the accuracy and compare it with the known aging clock model. Further, metacells from O-Met group were used to assess the geroprotective effects of metformin treatment. The integrated sn-transcriptAge was trained as follows, which included all metacells with age-dependent DEGs as input. The details of sn-transcriptAge and ΔAgeDiff in integrated and all cell types are listed in Table S4.

Aging-related trajectory analysis

Raw snRNA-seq counts were aggregated at the sample level in each cell type and subsequently extracted age-dependent DEGs were used to create an input matrix for Mfuzz[135] analysis. Age-dependent DEGs were grouped into four clusters according to their expression patterns, which is similar to the bulk RNA-seq analysis. The details of the aging-related trajectory DEGs for each cell type are listed in Table S4.

Rescue differential expression analysis

Rescue down-regulated DEGs were identified as the overlap of down-regulated DEGs (O-Met/O-Ctrl) and Aging-related trajectory cluster U. Rescue up-regulated DEGs were identified as the overlap of up-regulated DEGs (O-Met/O-Ctrl) and Aging-related trajectory cluster D. The details of the rescued DEGs for each cell type are listed in Table S4.

Cell type prioritization analysis

Augur[108] was used in 3 groups (Y-Ctrl, M-Ctrl, O-Ctrl) to prioritize aging-sensitive cell types. For metformin-sensitive cell types, Augur[108] was used in 2 groups (O-Ctrl, O-Met). Results were further visualized with the ggplot2[106] or ggpubr R package.

Functional enrichment analysis

Over Representation Analysis (ORA) was analyzed by Clusterprofiler (version 3.1.0)[110] and Metascape (http://metascape.org/gp/index.html).[102] Gene set enrichment analysis (GSEA) was analyzed by fgsea (version 1.26.0). Results were further visualized with the ggplot2[106] or ggpubr R package.

Gene set score analysis

Gene sets were collected from MsigDB (https://www.gsea-msigdb.org/gsea/index.jsp). In addition, modified gene sets were generated by overlapping with aging-related trajectory genes (Cluster D and Cluster U) to isolate aging-related pathway alteration. Next, perform "AddModuleScore" function in Seurat to calculate the gene set score. Genes in each gene set are listed in Table S4.

QUANTIFICATION AND STATISTICAL ANALYSIS

The data for cognitive testing and structural MRI were processed using Matlab and SPSS software. The data for micro-CT pathological staining, real-time quantitative PCR and western blotting were processed using PRISM software (GraphPad 9 Software). The data for bulk RNA-seq, snRNA-seq, proteomics, metabolomics and DNA methylation sequencing were using R packages, which have equal variances. A P-value < 0.05 was considered statistically significant. P-values are presented in the indicated figures as appropriate.

Supplemental figures

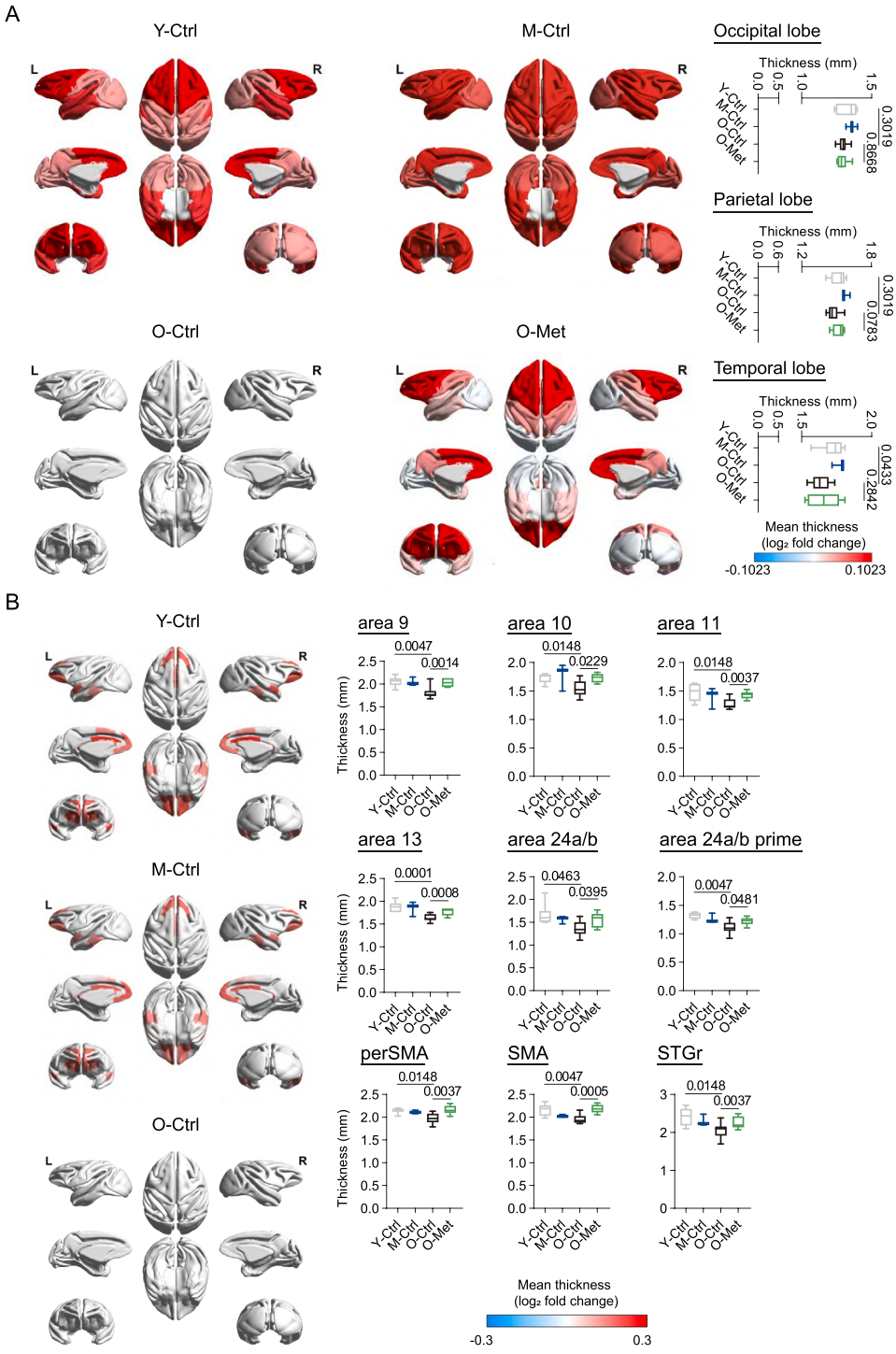

Figure S1. MRI examination of the impact of aging and metformin on cortical thickness in the brain, related to Figure 1

(A) MRI assessment of cortical thickness at the lobe level in Y-Ctrl, M-Ctrl, O-Ctrl, and O-Met monkeys is presented. log_2(fold change) in cortical thickness is displayed on the mid-gray surface, compared to the O-Ctrl group. Data for cortical thickness are presented as the mean value across both hemispheres for each

(legend continued on next page)

monkey. The boxes show the median (center line), the quartile range (25%–75%), and the whiskers (minimum and maximum), with GLMM analysis *p* values annotated. See STAR Methods.

(B) MRI assessment of cortical thickness at the region level in Y-Ctrl, M-Ctrl, O-Ctrl, and O-Met monkeys is presented. $\log_2$(fold change) in cortical thickness of regions showing the significant aging effect is displayed on the mid-gray surface, compared to the O-Ctrl group. Data for cortical thickness are presented as the mean value across both hemispheres for each monkey. The boxes show the median (center line), the quartile range (25%–75%), and the whiskers (minimum and maximum). Note that GLMM analysis *p* values for specific areas—9, 11, 13, 24a/b, 24a/b prime, perSMA, SMA, and STGr—are provided. Additionally, Mann-Whitney test *p* values for area 10 are indicated. See STAR Methods.

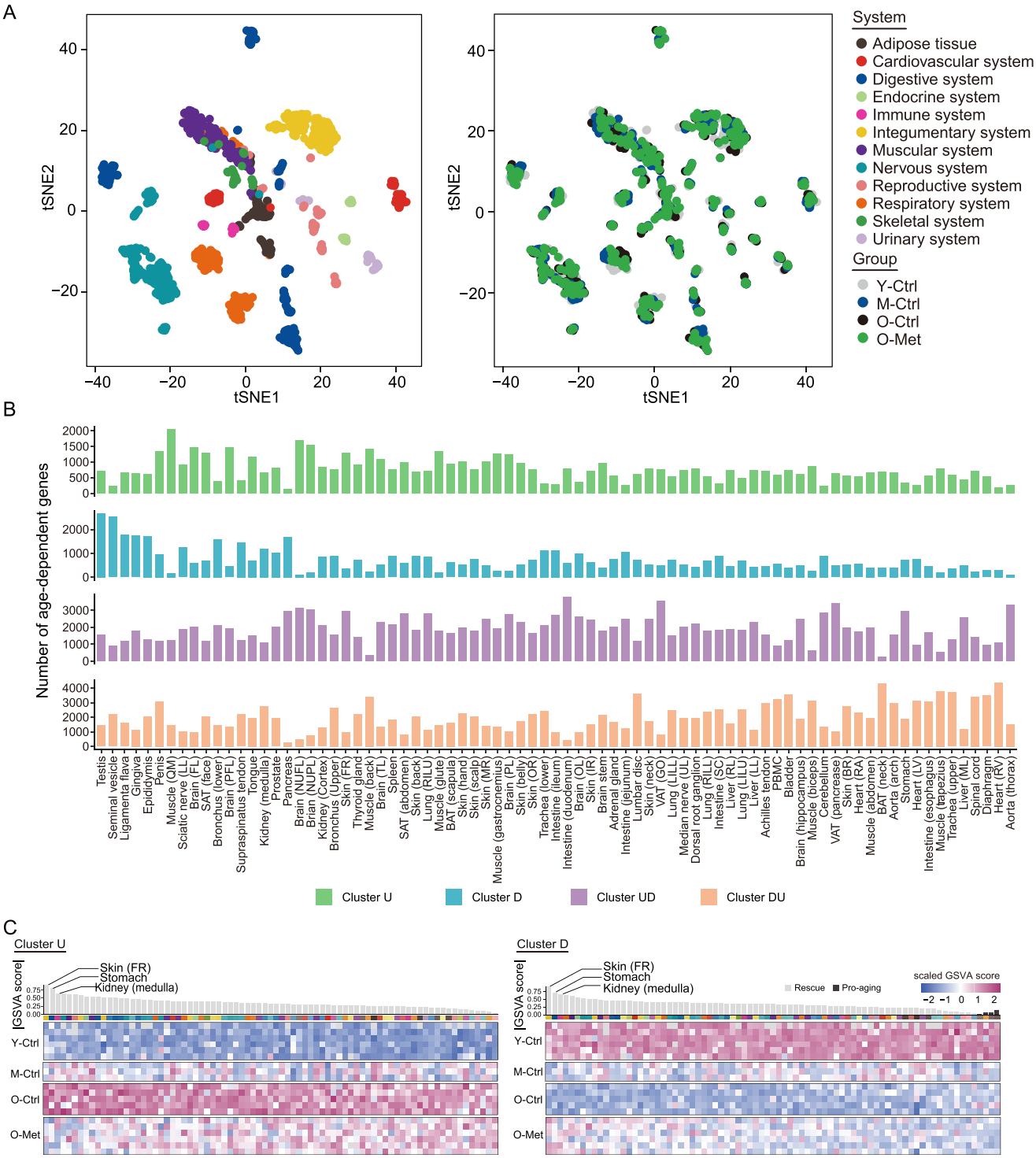

Figure S2. Transcriptomic profiling of multiple tissues during aging and in response to metformin intervention, related to Figure 2

(A) *t*-SNE plots showing different systems (left) or four groups (right) based on bulk RNA-seq data.

(B) Bar plot depicting the count of age-related genes across clusters within the 79 monkey tissues.

(C) Heatmap showing GSVA score of age-dependent genes in clusters U and D in different groups.

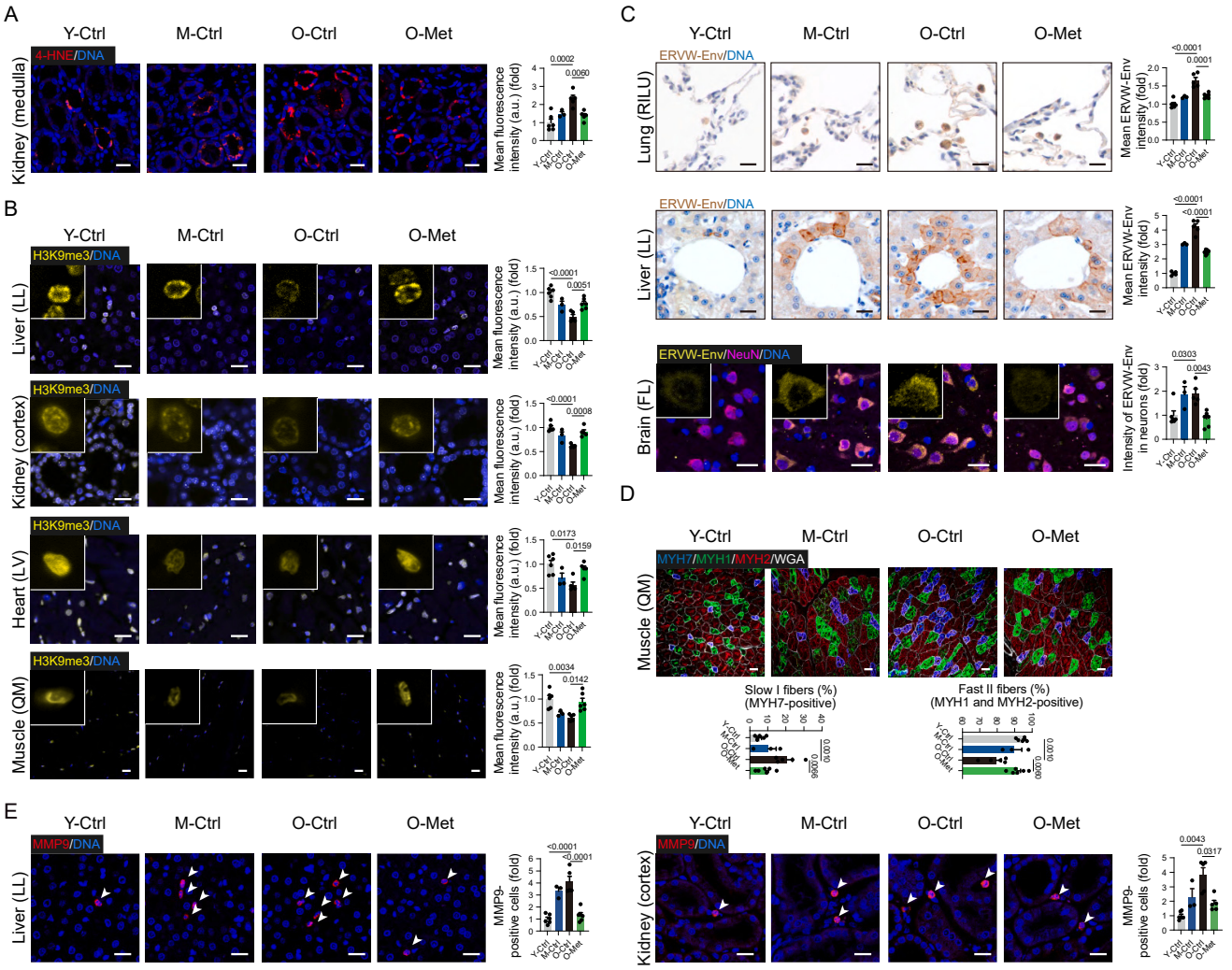

Figure S3. Aging phenotype evaluation across multiple monkey tissues, related to Figure 3

(A) Immunofluorescence examination of 4-HNE in kidney (medulla) in Y-Ctrl, M-Ctrl, O-Ctrl, and O-Met monkeys. Scale bars, 20 μm.

(B) Immunofluorescence evaluation of H3K9me3 in liver (LL), kidney (cortex), muscle (QM), heart (LV) of Y-Ctrl, M-Ctrl, O-Ctrl, and O-Met monkeys. Scale bars, 20 μm.

(C) Immunohistochemical and immunofluorescent assessment of ERVW-Env in lung (RILU), liver (LL), and brain (FL) in Y-Ctrl, M-Ctrl, O-Ctrl, and O-Met monkeys. The arrows indicate ERVW-Env-positive cells. Scale bars, 20 μm.

(D) Immunofluorescence analysis of MYH1, MYH2, and MYH7 in muscle (QM) of Y-Ctrl, M-Ctrl, O-Ctrl, and O-Met monkeys. Scale bars, 100 μm.

(E) Immunofluorescence examination of MMP9 in liver (LL) and kidney (cortex) in Y-Ctrl, M-Ctrl, O-Ctrl, and O-Met monkeys. Scale bars, 20 μm.

The quantified data in (A)–(E) are shown as means ± SEMs, Mann-Whitney test *p* values of heart (LV) in (B), brain (FL) in (C) and kidney (cortex) in (E) are indicated, one-way ANOVA with Tukey's multiple comparisons test *p* values of (A), liver (LL), kidney (cortex) and muscle (QM) in (B), lung (RILU) and liver (LL) in (C) and (D), kidney (cortex) in (E) are indicated. Y-Ctrl: $n = 6$, M-Ctrl: $n = 3$, O-Ctrl: $n = 5$, O-Met: $n = 5$–6 monkeys in (A)–(E).

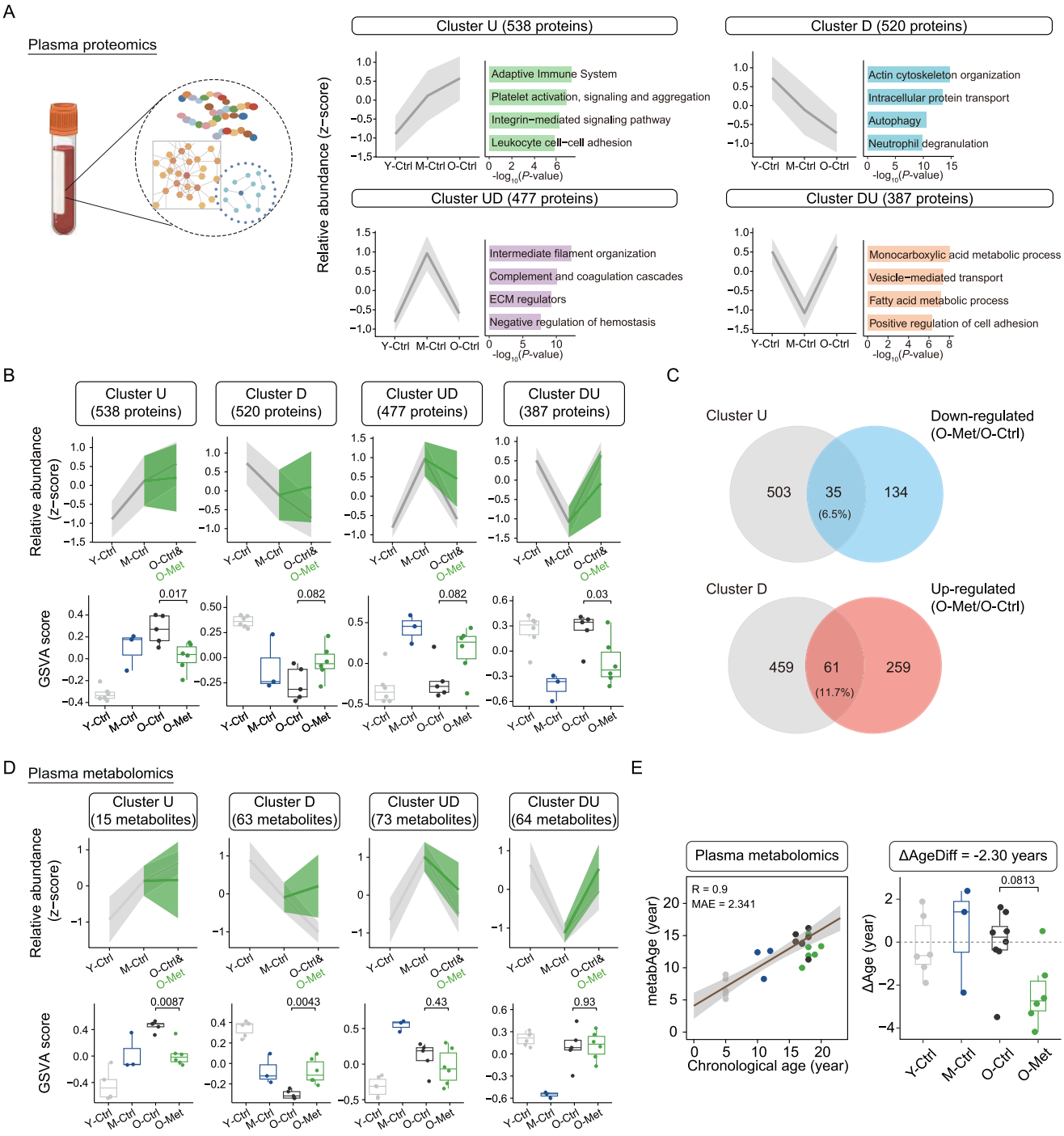

Figure S4. Plasma proteomics and metabolomics changes during aging and following metformin intervention in monkeys, related to Figure 4

(A) Clustering analysis of plasma proteomic data from monkeys during aging process. The number of age-dependent proteins in each cluster is shown. Solid lines and ribbons represent mean of standardized protein abundance across clusters ± SDs.

(B) Abundance changes in age-dependent plasma proteins from monkeys upon metformin treatment (top). Solid lines and ribbons represent mean of standardized protein abundance across clusters ± SDs. Box plot showing GSVA score of age-dependent proteins in different groups (bottom). Wilcoxon rank-sum test *p* values are indicated.

(C) Venn plot showing the number and proportion of rescue age-dependent proteins from clusters U and D.

(legend continued on next page)

(D) Abundance changes in age-dependent plasma metabolites from cynomolgus monkeys upon metformin treatment (top). Solid lines and ribbons represent mean of standardized metabolite abundance across clusters ± SDs. Box plot showing GSVA score of age-dependent metabolites in different groups (bottom). Wilcoxon rank-sum test *p* values are indicated.

(E) Dot plot showing predicted biological age (metabAge) based on plasma proteomics (left). Boxplot illustrating the rescue of monkeys' biological age (metabAge) by metformin treatment (right). The dashed line indicates no difference between the predicted biological age and the expected chronological age (ΔAge = 0), with the dot-to-line distance reflecting the individual's aging pace. Wilcox rank-sum test *p* values are indicated.

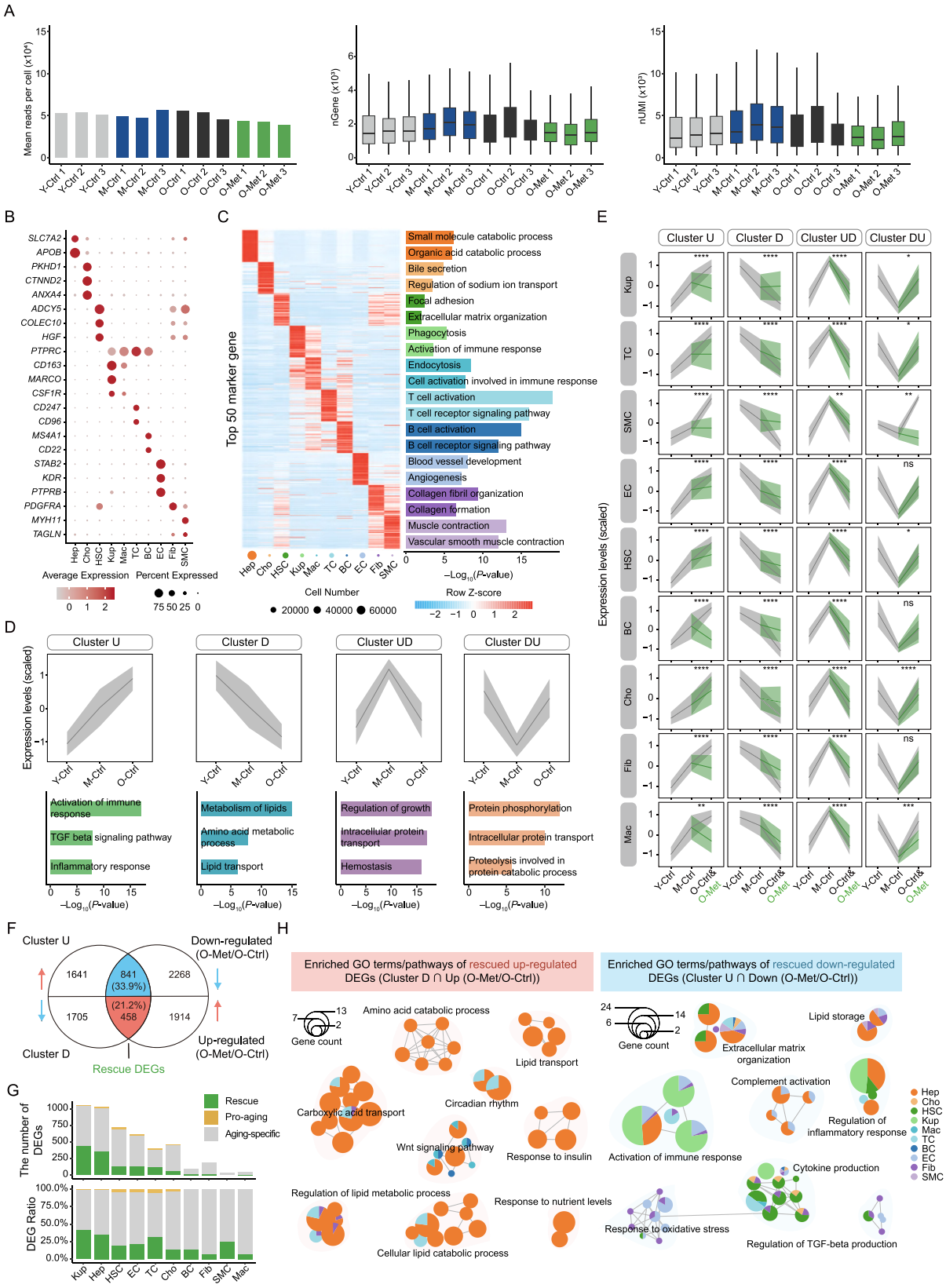

(legend on next page)

Figure S5. Quality control assessment of monkey liver snRNA-seq data, related to Figure 5

(A) Barplot showing the mean reads per cell in different samples (left). Boxplot showing the detected gene number in different samples (middle). Boxplot showing the detected UMI number in different samples (right).

(B) Dot plot showing the expression of marker genes used to annotate cell types.

(C) Heatmap showing the top 50 marker gene in different cell types. The enriched pathways, based on gene analysis, are depicted on the left.

(D) Clustering analysis of aging-dependent DEGs from liver during aging process (top). Barplot showing functional enrichment in 4 clusters (bottom). Solid lines and ribbons represent mean of count removed sequencing depth across clusters ± SDs.

(E) Metformin-induced expression shifts in age-sensitive genes across 9 major monkey liver cell types. Solid lines and ribbons represent mean of count removed sequencing depth across clusters ± SDs. Wilcoxon rank-sum test p values are indicated (not significant (ns), $p > 0.05$, * $p < 0.05$, ** $p < 0.01$, *** $p < 0.001$, **** $p < 0.0001$).

(F) Venn diagrams illustrate the counts of aging, Met, and rescued differentially expressed genes (DEGs). The intersections show the quantities of down-regulated (top) and up-regulated (bottom) rescued DEGs.

(G) snRNA-seq reveals the count and proportion of rescue and pro-aging DEGs across the 10 primary liver cell types.

(H) Networks depicting key Gene Ontology (GO) terms significantly enriched among rescued DEGs, as determined by functional enrichment analysis.

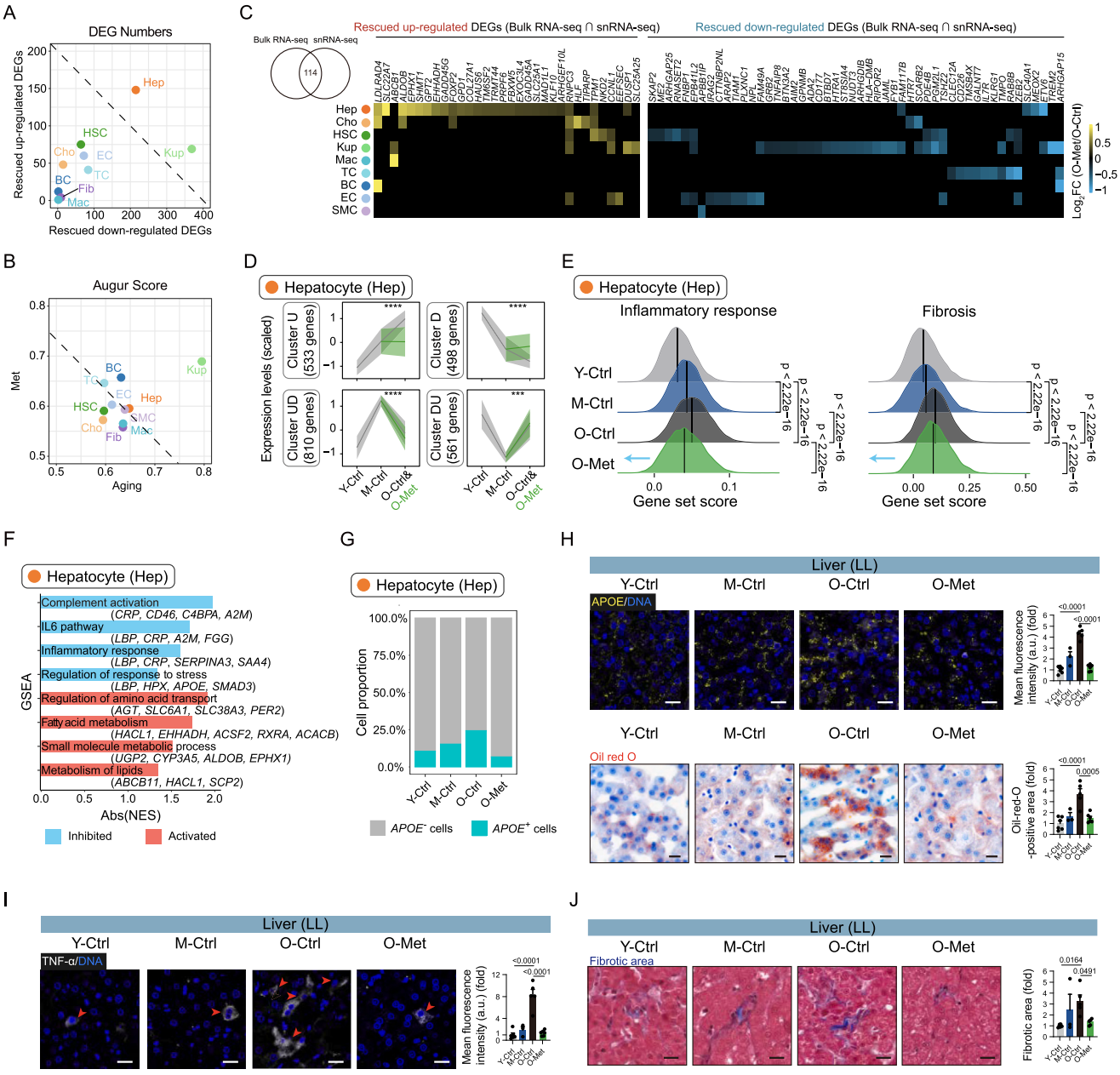

Figure S6. Metformin counteracts liver aging and enhances hepatic metabolic performance in monkeys, related to Figure 5

(A) Dot plot displaying up-regulated and down-regulated rescued DEGs across various liver cell types, as revealed by snRNA-seq.

(B) Dot plot illustrating the prioritization of liver cell types from snRNA-seq data using Augur.

(C) Heatmap depicting the expression patterns of overlapping rescued DEGs, derived from both snRNA-seq and bulk RNA-seq data, across various liver cell types. The color gradient from blue to red represents gene expression levels ranging from low to high in the O-Met/O-Ctrl comparison group.

(D) Metformin-induced expression shifts in age-sensitive genes within monkey hepatocytes. Solid lines and ribbons represent mean of count removed sequencing depth across clusters ± SDs. Wilcoxon rank-sum test *p* values are indicated. Wilcoxon rank-sum test *p* values are indicated (not significant (ns), $p > 0.05$, * $p < 0.05$, ** $p < 0.01$, *** $p < 0.001$, **** $p < 0.0001$).

(E) Ridge plots illustrating the representative gene set scores across the four groups, with the black line indicating median expression. Wilcoxon rank-sum test *p* values are indicated.

(F) Barplot illustrating representative GO terms significantly ($p < 0.05$) post-metformin treatment in hepatocytes, based on gene set enrichment analysis.

(G) Bar plot showing the proportion of *APOE*-positive cells in monkey hepatocytes from different groups.

(legend continued on next page)

(H) Immunofluorescence analysis of APOE (top) and oil red O staining evaluation (bottom) of liver (LL) in Y-Ctrl, M-Ctrl, O-Ctrl, and O-Met monkeys. Scale bars, 20 μm.
(I) Immunofluorescence analysis of TNF-α in liver (LL) of Y-Ctrl, M-Ctrl, O-Ctrl, and O-Met monkeys. The arrows indicate TNF-α-positive cells. Scale bars, 20 μm.
(J) Masson's trichrome staining evaluation of liver (LL) in Y-Ctrl, M-Ctrl, O-Ctrl, and O-Met monkeys. Scale bars, 20 μm.
The quantified data in (H)–(J) are shown as means ± SEMs, one-way ANOVA with Tukey's multiple comparisons test *p* values are indicated. Y-Ctrl: $n = 6$, M-Ctrl: $n = 3$, O-Ctrl: $n = 5$, O-Met: $n = 6$ monkeys in (H)–(J).

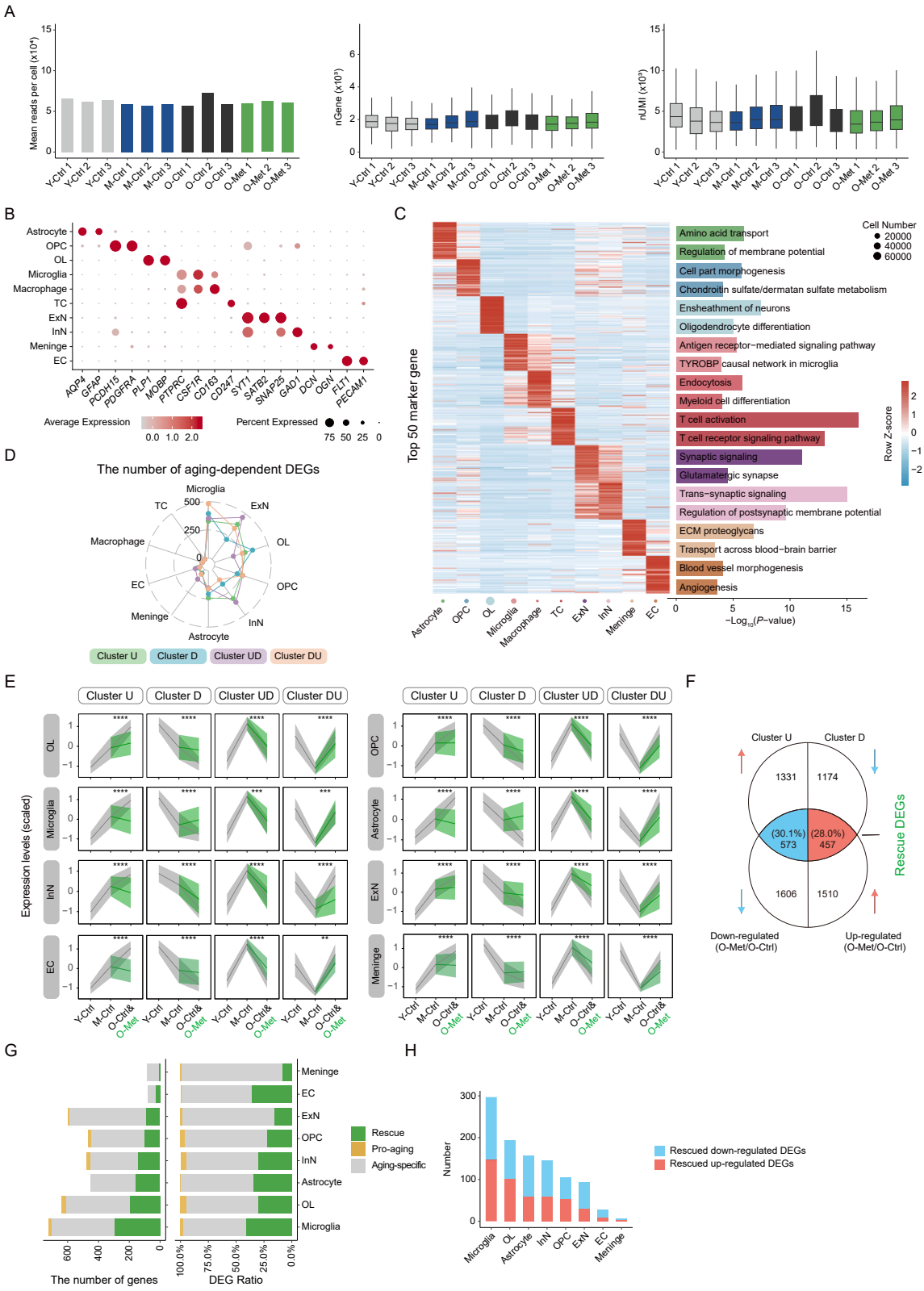

(legend on next page)

Figure S7. Quality control assessment of monkey frontal lobe snRNA-seq data, related to Figure 5

(A) Barplot showing the mean reads per cell in different samples (left). Boxplot showing the detected gene number in different samples (middle). Boxplot showing the detected UMI number in different samples (right).

(B) Dot plot depicting expression levels of marker genes utilized for cell type annotation.

(C) Heatmap illustrating the top 50 marker genes across various cell types. Enriched pathways based on these genes are displayed on the left.

(D) Radar plot showing the number of aging-dependent DEG in different clusters.

(E) Expression variations of age-associated genes in eight monkey frontal lobe cell types, following metformin treatment. Solid lines and ribbons represent mean of count removed sequencing depth across clusters ± SDs. Wilcoxon rank-sum test p values are indicated (not significant (ns), $p > 0.05$, * $p < 0.05$, ** $p < 0.01$, *** $p < 0.001$, **** $p < 0.0001$).

(F) Venn diagrams display the counts of aging, Met, and rescued DEGs, with the intersections highlighting the quantities of down-regulated (left) and up-regulated (right) rescued DEGs.

(G) snRNA-seq data indicates the count and proportion of rescue and pro-aging DEGs among the 8 predominant cell types in the frontal lobe.

(H) Barplot showing the rescued DEG number in different cell types.

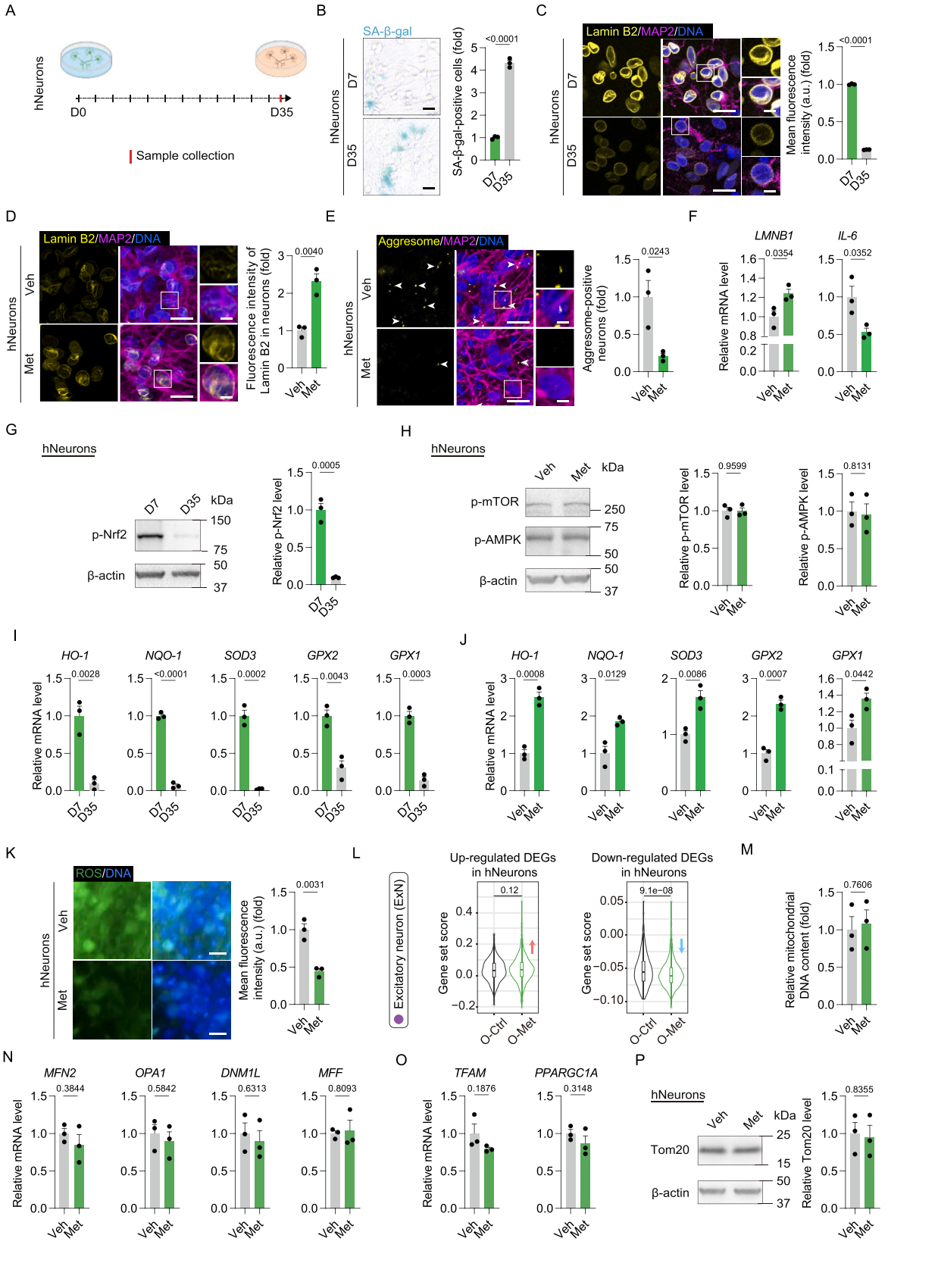

(legend on next page)

Figure S8. Assessment of senescent phenotypes in metformin-treated hNeurons under extended culture conditions, related to Figure 7

(A) Depiction of senescence in hNeurons induced by extended culture.
(B) SA-β-gal staining evaluation in hNeurons at day 7 and day 35 of culture.
(C) Immunofluorescence examination of Lamin B2 in MAP2-marked hNeurons on day 7 or day 35.
(D) Immunofluorescence analysis of Lamin B2 in MAP2-marked hNeurons on day 35 after treatment with Veh or Met.
(E) Aggresome staining assessment in MAP2-marked hNeurons on day 35 after treatment with Veh or Met. The arrows indicate aggresome-positive neurons.
(F) Transcript levels of *LMNB1* and *IL-6*, markers of hNeuron senescence, on day 35 after treatment with Veh or Met.
(G) Western blot analysis of p-Nrf2 levels in hNeurons at days 7 and 35 of culture.
(H) Western blot analysis of p-mTOR and p-AMPK levels in hNeurons on day 35 post-treatment with Veh or Met.
(I) Transcript levels of Nrf2-target genes *HO-1*, *NQO-1*, *SOD3*, *GPX2*, and *GPX1* in hNeurons during day 7 and day 35 culture.
(J) Transcript levels of Nrf2-target genes *HO-1*, *NQO-1*, *SOD3*, *GPX2*, and *GPX1* in hNeurons on day 35 after treatment with Veh or Met.
(K) ROS staining evaluation in hNeurons on day 35 following treatment with Veh or Met.
(L) Violin plot depicting gene set scores post-metformin treatment in monkey frontal lobe excitatory neurons, with the black line indicating median expression. Wilcoxon rank-sum test *p* values are indicated.
(M) Real-time quantitative PCR analysis of relative mitochondrial DNA content in hNeurons on day 35 after treatment with Veh or Met.
(N) Transcript levels of mitochondrial dynamics-related genes *MFN2, OPA1, DNM1L*, and *MFF* in hNeurons on day 35 after treatment with Veh or Met.
(O) Transcript levels of mitochondrial function-associated genes *TFAM* and *PPPARGC1A* in hNeurons on day 35 after treatment with Veh or Met.
(P) Western blot analysis of Tom20 protein levels in hNeurons on day 35 after treatment with Veh or Met.
The quantified data in (B)–(K) and (M)–(P) are shown as means ± SEMs, two-tailed Student's t test *p* values are indicated in (B)–(K) and (M)–(P). *n* = 3 biological samples per group in (B)–(K) and (M)–(P). Scale bars: 20 and 5 μm (zoomed-in images) in (B)–(E) and (K).

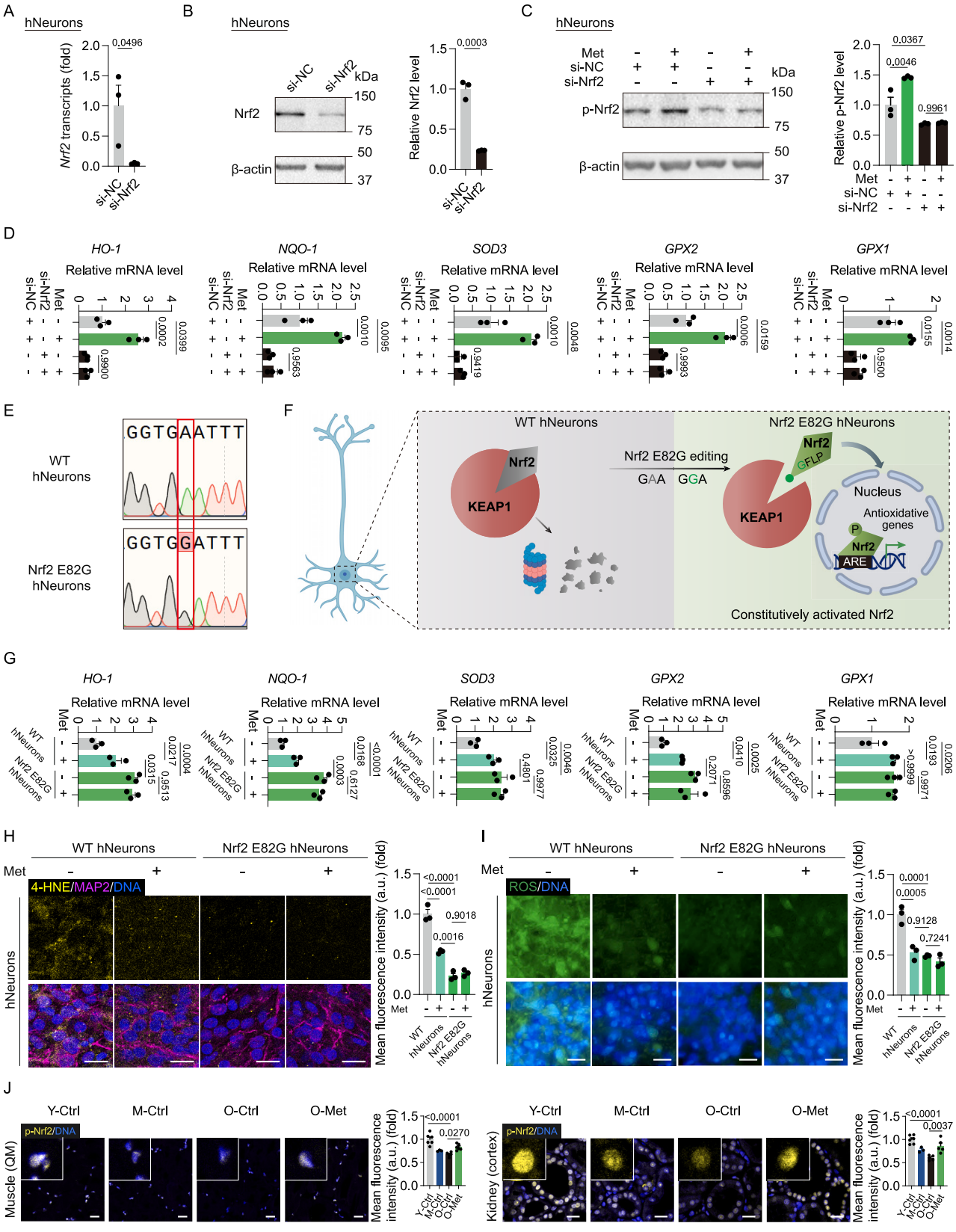

(legend on next page)

Figure S9. Senescent phenotype assessment in metformin-treated si-Nrf2 and Nrf2 E82G hNeurons under extended culture, related to Figure 7

(A) *Nrf2* mRNA levels in hNeurons 2 days after secondary siRNA transfection targeting si-NC or si-Nrf2.
(B) Nrf2 protein levels determined by western blot in hNeurons 3 days following the secondary siRNA transfection for si-NC or si-Nrf2.
(C) Western blotting of p-Nrf2 levels in si-NC or si-Nrf2 hNeurons on day 21 after treatment with Veh or Met.
(D) Transcript levels of Nrf2-target genes *HO-1, NQO-1, SOD3, GPX2*, and *GPX1* in si-NC or si-Nrf2 hNeurons on day 21 after treatment with Veh or Met.
(E) Sequencing outcomes of Nrf2 gene PCR products in WT and Nrf2 E82G hNeurons.
(F) Schematic showing the Nrf2 E82G mutation promotes nuclear entry and activation of antioxidant target genes.
(G) Transcript levels of Nrf2-target genes *HO-1, NQO-1, SOD3, GPX2*, and *GPX1* in WT or Nrf2 E82G hNeurons on day 35 after treatment with Veh or Met.
(H) Immunofluorescence examination of 4-HNE in MAP2-marked WT or Nrf2 E82G hNeurons on day 35 after treatment with Veh or Met.
(I) ROS staining assessment of WT or Nrf2 E82G hNeurons on day 35 after treatment with Veh or Met.
(J) Immunofluorescence analysis of p-Nrf2 in muscle (QM) and kidney (cortex) of Y-Ctrl, M-Ctrl, O-Ctrl, and O-Met monkeys.
The quantified data in (A)–(D) and (G)–(J) are shown as means ± SEMs, two-tailed Student's t test *p* values are indicated in (A) and (B), one-way ANOVA with Tukey's multiple comparisons test *p* values are indicated in (C) and (D) and (G)–(J). $n = 3$ biological samples per group in (A)–(D) and (G)–(I). Y-Ctrl: $n = 6$, M-Ctrl: $n = 3$, O-Ctrl: $n = 5$, O-Met: $n = 5$–6 monkeys in (J). Scale bars: 20 μm in (H)–(J).